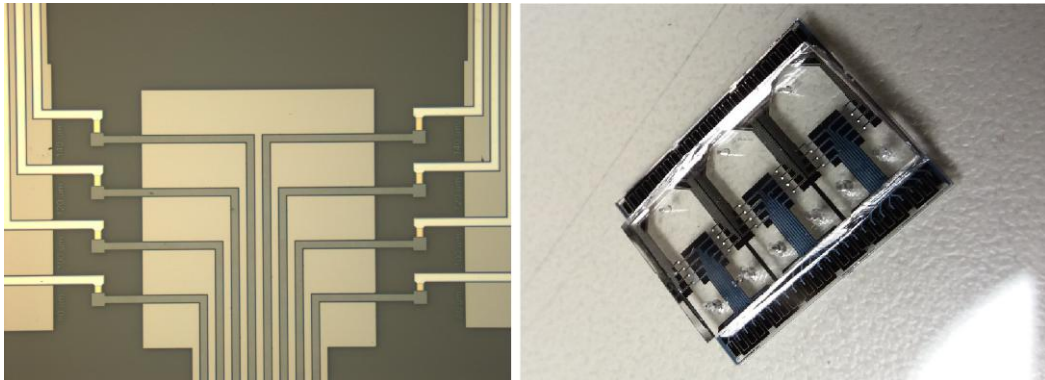




TÉCNICO
LISBOA



MEMS integration in microfluidics for biosensing applications:

Static cantilever sensor for DNA detection

Pedro Manuel Lourenço Brito

Thesis to obtain the Master of Science Degree in

Engineering Physics

Supervisor(s): Prof. João Pedro Estrela Rodrigues Conde
Prof. Susana Isabel Pinheiro Cardoso de Freitas

Examination Committee

Chairperson: Prof. Pedro Miguel Félix Brogueira
Supervisor: Prof. João Pedro Estrela Rodrigues Conde
Member of the Committee: Prof. Luís Humberto Viseu Melo

April 2017

Dedicated to my parents...

Acknowledgments

Agradeço muito todo o apoio e ajuda prestada durante o desenvolvimento desta tese aos meus orientadores e chefes do grupo de MEMS/BioMEMS do INESC-MN Prof. Dr. João Pedro Conde e Dr. Virginia Chu. Sempre se demonstraram interessados no desenvolvimento desta tese e nos resultados que esta ia retornando nas várias reuniões de grupo. Gostava também de mencionar a Prof. Susana Freitas por me ter introduzido à área das micro e nanotecnologias e por ter sempre demonstrado uma grande abertura para discutir qualquer assunto. Continuando na perspectiva académica, queria ainda agradecer à Prof. Maria Teresa Pinheiro por me ter feito ganhar tanto interesse pelas áreas da Física Aplicada e por me ter permitido explorar um pouco mais esse lado num pequeno projecto realizado no seu local de trabalho numa altura anterior.

Um agradecimento especial deve ser feito aos meus colegas do INESC-MN com quem tive o prazer de aprender e trabalhar. Menciono mais particularmente a Catarina Caneira pela excelente introdução que me deu sobre ensaios biológicos e todas as dicas e incentivos relativos a esta secção da minha tese. E menciono acima de todos o Rui Pinto que foi quem, de forma incansável, mais directamente me ajudou quando alguma dificuldade surgia e que sempre se mostrou interessado no meu trabalho, mais do que um colega, tornou-se um amigo. Não quero deixar de referir a Inês, o Ruben, o Eduardo, o Denis, o Ricardo, o Guilherme, a Jéssica, a Catarina e a Roberta que sempre foram também muito prestáveis e uma boa companhia de trabalho.

Agradeço aos meus amigos que desde há vários anos estão sempre ao meu lado para me apoiar e dar força, mas também para aconselhar e simultaneamente descontraír e festejar mesmo quando não há razão para tal. Aos amigos mais recentes o Duarte e o Gonçalo que nem por isso são menos importantes e que estavam sempre dispostos a dispensar um pouco do seu tempo, principalmente o Duarte que me acompanhou em várias maratonas de trabalho, mesmo quando não lhe apetecia assim tanto. Aos amigos que fiz através do curso a Maria, a Bárbara, o Luís e a Sofia por quem eu sempre tive e terei um carinho muito especial e que me conhecem como poucos. E aos amigos do secundário, especialmente às Anas que receberam muitas recusas da minha parte para certos convites para jantar e ir ao cinema durante esta época atribulada.

Por fim, agradeço aos meus pais todo o suporte dado não só agora, mas desde sempre. Sem o apoio deles, esta tese não teria sido escrita e eu não teria atingido o sítio a que cheguei.

Resumo

O foco deste trabalho é o desenvolvimento de um dispositivo que inclui SEMM e microfluídica para detecção biológica. A estrutura utilizada é uma consola multi-camada operando no modo estático e composta por um par de eléctrodos, uma camada estrutural de silício amorfo e uma camada de ouro para funcionalização com ADN. A deflexão da consola é monitorizada por um sistema de leitura capacitiva que mede a capacidade bem como a resistência entre os dois eléctrodos.

A adesão em consolas foi analisada e o protocolo padrão para desprendimento que usa hexano foi classificado com o trabalho de adesão reduzido de $77 \pm 8 \mu\text{J.m}^{-2}$.

Alguns ensaios de testes biológicos foram executados e mostraram que o grupo tiol ligado à cadeia única de ADN tem uma grande afinidade selectiva ao ouro depositado sobre a consola. Alguns parâmetros foram descobertos como sendo facilmente sintonizáveis de modo a modificar a densidade de sondas de acordo com o que é mais apropriado. A hibridação provou ser mais problemática, no entanto, um protocolo foi estabelecido retornando sinais razoáveis monitorizados por quimioluminescência.

Após combinar ambas as tecnologias em estudo, algumas medidas capacitivas preliminares em água foram executadas e a sensibilidade deste sistema revelou ser de 0.8 nm com um nível de ruído capacitivo de 0.04 fF. Infelizmente, não foi possível correr um ensaio biológico completo com estes dispositivos porque alguns problemas relativos à selagem e conexão com a PCB acabaram por danificar os dispositivos existentes.

Palavras-chave: SEMM, detecção biológica, ADN, modo estático, leitura capacitiva

Abstract

The focus of this work is the development of a device that comprises both MEMS and microfluidics for biosensing. The used structure is a multilayered cantilever operating in the static mode and composed by a pair of electrodes, a structural layer of amorphous silicon and a gold layer for functionalization with DNA. The deflection of the cantilever is monitored by a capacitive readout system that measures both capacitance and resistance between the top and bottom electrodes.

Stiction in cantilevers was analysed and the standard protocol for release using n-hexane was ranked with a low work of adhesion of $77 \pm 8 \mu\text{J.m}^{-2}$.

Some biological test assays have been performed and they showed that the thiol group linked to the single stranded DNA has a very selective affinity to the gold deposited on top of the cantilever. Some parameters were found to be easily tuned in order to change the probe density according to what is more appropriate. Hybridization proved to be more problematic, however one protocol was established returning reasonable signals tracked by chemiluminescence.

After combining both technologies under study, some preliminary capacitive measurements in water were performed and the sensitivity of such system revealed to be 0.8 nm with a capacitive noise level of 0.04 fF. Unfortunately, it was not possible to run a full biological assay with these devices because some problems regarding sealing and interconnection with the PCB ended up damaging the existent devices.

Keywords: MEMS, biosensing, DNA, static mode, capacitive readout

Contents

Acknowledgments	v
Resumo	vii
Abstract	ix
List of Tables	xiii
List of Figures	xv
Nomenclature	xxi
1 Introduction	1
1.1 Motivation	1
1.2 State of the art	2
1.3 Objectives	4
1.4 Thesis Outline	5
2 Background	7
2.1 Physical principles and operation modes of a cantilever	7
2.1.1 Static mode	8
2.1.2 Dynamic mode	11
2.1.3 Energy dissipation	15
2.1.4 Electrical model of the cantilever	17
2.1.5 Pull-in voltage model	18
2.1.6 Stiction effect	20
2.2 Microfluidics physics	21
2.3 Properties of DNA	23
3 Experimental methods and implementation	27
3.1 Functionalization with ssDNA	27
3.2 MEMS fabrication	32
3.2.1 Photolithography	38
3.2.2 Magnetron sputtering deposition	39
3.2.3 Plasma-enhanced chemical vapor deposition	41
3.2.4 Reactive Ion Etching	42
3.2.5 Wet etching	43

3.2.6	Lift-off	43
3.3	Microfluidics fabrication	45
3.3.1	Interface and control of microfluidics	48
3.3.2	Integration of microfluidics into MEMS	49
3.4	Characterization and measurement setup	50
4	Results	55
4.1	Fabrication outcome	55
4.1.1	Samples for biological tests	55
4.1.2	Samples for stiction tests	57
4.1.3	Samples for capacitive measurements	57
4.2	Biological tests	58
4.3	Stiction tests	70
4.4	Resonance measurements	71
4.5	Capacitive measurements	73
5	Conclusions	77
	Bibliography	81
A	Fabrication runsheets	87

List of Tables

2.1	List of the main properties of dsDNA and ssDNA. The structure considered for the dsDNA is the B-form, which is the most common one. The charge of the strand per unit length is given in terms of the charge of the electron, e^-	24
3.1	List of oligonucleotides used in this work, including information about modifications and purpose of each molecule.	31
3.2	Typical conditions and parameters applied for the depositions in Nordiko 7000. For the deposition of TiW it is used the recipe "TiW1500A Low Stress" while for Al it is used the recipe "Al5000A 2kW" twice.	40
3.3	Typical conditions and parameters applied for the depositions in Alcatel SCM 450. Before each deposition it is performed a cleaning step of the target to be used by turning on the power while keeping the shutter over the sample for 3 to 5 min.	40
3.4	Typical conditions and parameters applied for the PECVD. This recipe is optimized to achieve low residual film stress.	41
3.5	Typical conditions and parameters applied for the RIE of TiW and a-Si:H using LAM Plasma Etcher. Note that when etching solely 150 nm of TiW, the duration of the process is roughly 250 min, while for the bilayer it is necessary a process of 650 min.	42
3.6	Typical conditions and parameters applied for the deposition of Al in Nordiko 7000 in order to fabricate the hard mask.	45
3.7	Parameters for the spin coating of SU-8 on top of the silicon substrate.	46
3.8	Conditions and materials used during the process of SU-8 2015 lithography (20 μm thickness), immediately after spin coating.	47
3.9	Conditions and materials used during the process of SU-8 50 lithography (50 μm thickness), immediately after spin coating.	47
3.10	Parameters for the spin coating of PDMS on top of a glass substrate.	50
4.1	Average thickness of each material used for the biological assays after deposition and patterning. The measured values correspond to the average of multiple measurements in the profilometer and its experimental error is obtained by the calculation of the standard deviation.	56

4.2	Average thickness of each material used for the stiction tests. The measured values correspond to the average of multiple measurements in the profilometer. Since three different gaps were implemented, three different values are present for the sacrificial layer (Al).	57
4.3	Average thickness of each material used in the devices for the capacitive measurements. The measured values correspond to the average of multiple measurements in the profilometer and its experimental error is obtained by the calculation of the standard deviation.	58
4.4	Chemiluminescence intensity on PDMS/glass in arbitrary units for the different assays with blocking agents.	62
4.5	Resonance frequency and Q factor for each mode of vibration obtained by fitting a Lorentz curve. The voltages used for actuation of the cantilevers are also presented.	72
4.6	Average measurements in air and corresponding noise levels when the cantilevers are at equilibrium. The noise is calculated as the standard deviation.	74

List of Figures

1.1	Types of interfaces used for liquid handling when proceeding for MEMS functionalization.	3
1.2	Different types of integration of microfluidics in MEMS.	3
2.1	Schematics of a free cantilever without residual stress (<i>left</i>) and a deflected cantilever due to surface stress and/or a force acting on the tip (<i>right</i>).	7
2.2	Modes of operation of a cantilever. In the static mode, the adsorption of molecules creates a variation of the surface stress causing the deflection of the cantilever. In the dynamic mode, by adding mass to the beam, its resonance frequency is shifted towards lower values.	8
2.3	Schematics of a cantilever working in the static mode under tensile and compressive stresses. An upwards deflection is characteristic of tensile stresses while compressive stress originates a downwards deflection.	9
2.4	Schematics of a cantilever on the plane xOz showing the deflection in z at a certain point x of the beam. The beam is fixed at $x = 0$ and free to move at $x = L$ where the deflection is maximum, ψ_{max}	10
2.5	Mechanical model of a cantilever operating in the dynamic mode. It is similar to the damped harmonic oscillator driven by a certain force $F(t)$	12
2.6	Plot of the roots of the frequency equation 2.27 for a cantilever.	14
2.7	Plot of three different outcomes in a damped harmonic oscillator based on the value of the damping ratio.	15
2.8	Plot of a general resonance spectrum and the corresponding calculation of the Q factor. .	16
2.9	Schematics of the equivalent electrical models for a resonator.	17
2.10	<i>Left</i> : Typical array of cantilevers used to determine the detachment length. <i>Right</i> : Schematics of a cantilever that adhered to the substrate due to stiction.	20
2.11	Typical flow and shear stress profiles inside a microchannel with a circular cross section. The channel is assumed to have a radius R and the velocity of the flow depends on the radial cylindrical coordinate, $v_z(r)$. The shear stress, $\tau(r)$, also depends on the radial position, being more intense near the walls of the channel.	22

2.12	When a suspended structure is immersed in a fluid that is evaporating, a meniscus forms underneath it. Its shape depends on the affinity of the material to water, producing different contact angles. The restoring force of the structure needs to surpass the adhesive force which comprises the force created by the meniscus (arising from surface tension), F_m , and the normal component of the viscous force, $F_{v\perp}$	23
2.13	In a dsDNA molecule, the different nucleobases are linked by means of hydrogen bonds while the deoxyribose and the phosphate group form covalent bonds. In a ssDNA molecule, only one of the strands is present. During hybridization or even just with a ssDNA molecule, some mismatches may occur and atypical configurations arise: hairpin (ssDNA), bulge or loop.	25
3.1	Schematics of the two techniques employed for target detection. When the purpose is to detect the probe, a similar configuration is applied, but instead of a dsDNA one has only the ssDNA and the label is attached at the 3' termination.	28
3.2	Schematized diagram of fluorescence and some intermediate/competing processes upon excitation of a molecule using a light source. In the spectrum of absorbance and fluorescence it is possible to distinguish the Stokes shift.	29
3.3	Chemical reaction between peroxide and luminol in the presence of HRP for production of chemiluminescent signal. The signal is emitted when the excited product of reaction reaches the ground state.	30
3.4	<i>Left</i> : 2D top view of the microchannel array containing a total of 16 channels per substrate and multiple patterns inside each one; <i>Right</i> : 3D view of the microchannel array, showing the glass substrate where the various materials are patterned and the microchannels defined by soft lithography in the PDMS.	32
3.5	Sequence of patterns used in the structures of the first generation of biological tests. The sequence is repeated four times per channel.	33
3.6	Sequence of patterns used in the structures of the second generation of biological tests. This sequence is also repeated four times per channel. Patterns of TiW were added to the previous configuration.	33
3.7	Schematics of the structures for the stiction tests. Each cantilever was followed by a caption indicating its length which was allowed to range between 10 and 500 μm	34
3.8	Schematics of the top view of the structures used for the capacitive measurements. Each die is composed by three double channels like the one represented in the figure.	35
3.9	Sequence of steps for the fabrication of a cantilever, including the electrodes for actuation, the ground plane and the gold pattern on top. The schematics represent a lateral view of the structure.	36
3.10	(a),(b) Two different equipments that can be used to inspect the deposited and patterned layers of materials; (c) Dicing machine equipped with a diamond saw to separate the samples.	37

3.11 Equipment used for PR spin coating and development. (a) HDMS oven used for vapor priming; (b) automatic SVG track system for wafer processing; (c) PR spin coating and (d) PR development modules of the track system.	38
3.12 Direct Write Laser system for PR exposure. Inside the small chamber it is placed the laser and the corresponding focusing optics as well as the mechanical stage. There is also a CCD camera connected to a screen to assist in the alignment.	39
3.13 Magnetron sputtering is one of the techniques used for thin film deposition. In the figure, the process is exemplified for a general target material. The two machines used for deposition of TiW, Al, Cr and Au are also shown. The control of Nordiko 7000 is performed via computer with the appropriate software while Alcatel is manually set.	40
3.14 For the deposition of a-Si:H it is used the plasma-enhanced chemical vapor deposition depicted in the schematics. The equipment used at INESC-MN is composed by three different chambers, connected to various gas lines and pressure and temperature sensors. The excitation of the plasma is performed by RF power.	41
3.15 Given the physico-chemical nature of reactive ion etching, the etching profile becomes slightly rounded as depicted in the schematics. The equipment used for this process is automatized and optimized for multi-wafer processing.	42
3.16 Schematics of the different profiles that are obtained when using physical or chemical etching techniques. When processing a multilayered film, physical etching may damage other material layers due to poor selectivity of the process when comparing with chemical etching. At nanoscale, the thickness of the film may create some additional difficulties to the process.	43
3.17 <i>Left:</i> By visual inspection it seems that the wet etch of the hard mask of the microchannels is completed. <i>Right:</i> Images from the optical microscope showing the structures defined in the hard mask by wet etch. The images in green tones are taken after lithographic exposure, while the ones in black and white are taken after etching.	43
3.18 <i>Left:</i> In the beginning, only a uniform layer of metal over the sample is visible. <i>Middle:</i> After some moments, some of the PR starts dissolving and the metal that was deposit on top of it also starts peeling off. <i>Right:</i> Finally, all the PR is dissolved and the metal layer is patterned.	44
3.19 Images from the optical microscope, showing an incomplete lift-off (red marks). This result was obtained when it was not used ultrasonics bath during the process.	44
3.20 Schematics of the process for microfluidic channels fabrication.	45
3.21 (a) PDMS after mixing with the curing agent with a lot of air bubbles inside it and after degassification in the vacuum chamber; (b) Degassed PDMS is poured into a petri dish with the SU-8 mold inside it; (c) The PDMS can easily be peeled off from the mold which can be reused if not damaged.	47
3.22 Equipment used for microfluidics fabrication.	48

3.23	Schematics of the control setup for microfluidics control. The plastic tube where the metallic plug is inserted must be connected to the syringe needle placed in the pumping system.	48
3.24	Two different techniques for PDMS microfluidics sealing against a substrate.	49
3.25	Equipment used for the alignment of the microfluidics structure and the MEMS chip during the sealing procedure.	50
3.26	Example of a measurement of the signal on a gold surface. The average RGB intensity is measured for the area corresponding to each square.	51
3.27	Schematics of the customized optical setup used for resonance measurements of the MEMS structures in vacuum.	52
3.28	Lorentzian curve used for data fitting. Some general parameters are also represented.	53
3.29	Schematics of the 4-terminal pair configuration with cable shielding. Two different pairs of terminals are used for sensing the voltage and the current simultaneously.	54
3.30	Setup used for the capacitive measurements in the static mode of operation of the cantilevers.	54
4.1	Images taken under the optical microscope with different magnification lenses. It is clear the difference in contours between the grey material (a-Si:H) and the golden one (Cr+Au) due to the different patterning techniques used.	56
4.2	Structures after integration with microfluidics. <i>Left</i> : Reasonably well aligned channel and centered structures; <i>Right</i> : Although the channel is well aligned with the structures, they are not centered, possibly due to shrinkage of the PDMS.	56
4.3	Image of one die after release by wet etching. The black stripes along the beams of the longer cantilevers are evidence of stiction.	57
4.4	Set of images of the resultant structures for the capacitive measurements.	58
4.5	Results obtained by chemiluminescence by varying the flow rate of luminol and the instant of the measurement. <i>Left</i> : Plot of the signal on Au surfaces measured in three different instants at 10 and 20 $\mu\text{L}/\text{min}$; <i>Right</i> : Pictures taken from the microscope during the measurement at 20 $\mu\text{L}/\text{min}$.	59
4.6	Results obtained by chemiluminescence when using PBS and 1M TE NaCl as buffers. <i>Left</i> : Plot of the signal on Au surfaces measured for both solutions; <i>Right</i> : Pictures taken from the microscope during both measurements.	60
4.7	Results obtained by chemiluminescence by varying the flow rate of the probe inside the channel. <i>Left</i> : Plot of the signal on Au surfaces measured for three different probe flow rates; <i>Right</i> : Pictures taken from the microscope during the measurement.	60
4.8	Results obtained by chemiluminescence when a different incubation duration is implemented. <i>Left</i> : Plot of the signal on Au surfaces measured for various durations of incubation; <i>Right</i> : Pictures taken from the microscope during each measurement.	61

4.9	Results obtained by chemiluminescence when different blocking agents are used. <i>Left</i> : Plot of the signal on Au, TiW and PDMS/glass surfaces measured for various blocking materials; <i>Right</i> : Pictures taken from the microscope during each assay.	62
4.10	Results obtained by fluorescence from BSA marked with FITC after being washed multiple times with a constant flow rate of 5 $\mu\text{L}/\text{min}$. <i>Left</i> : Plot of the signal of BSA on Au and PDMS/glass surfaces measured after each minute of washing (the results for PDMS/glass correspond to the raw measurement); <i>Right</i> : Pictures taken from the microscope for each minute.	63
4.11	Results obtained by chemiluminescence when using thiolated and non-thiolated probes. <i>Left</i> : Plot of the signal on Au, TiW, a-Si:H and PDMS/glass surfaces measured for both types of probes (the results for PDMS/glass correspond to the raw measurement); <i>Right</i> : Pictures taken from the microscope for each assay.	64
4.12	Results obtained by chemiluminescence when implementing different procedures for probe flow and incubation. <i>Left</i> : Plot of the signal on Au surfaces measured with two different flow rates and different duration of flow and incubation; <i>Right</i> : Pictures taken from the microscope for each assay.	65
4.13	Results obtained by chemiluminescence for hybridization after incubation of probe for 3h. The color of the images was enhanced so that it was possible to confirm that no pattern was visible. <i>Left</i> : Pictures taken from the microscope for the assay with continuous flow of target at 0.75 $\mu\text{L}/\text{min}$; <i>Right</i> : Pictures taken from the microscope for the assay with target incubation for 3h after flowing for 5 min.	66
4.14	Results obtained by chemiluminescence for hybridization after incubation of probe for 24h and continuous flow of target. The measured signal on PDMS/glass surfaces is also indicated for each type of assay. <i>Left</i> : Plot for the three different events tested with the assays; <i>Right</i> : Pictures taken from the microscope for each assay and the measured signal on PDMS/glass.	67
4.15	Results obtained by fluorescence in order to track the density of BSA molecules along the entire protocol for hybridization. The measured signal on PDMS/glass surfaces corresponds to the raw signal obtained by the software. <i>Left</i> : Plot of the signal intensity measured for each step of the protocol; <i>Right</i> : Pictures taken from the microscope for some particular steps of the entire protocol.	68
4.16	Results obtained by fluorescence. <i>Left</i> : Plot of the signal on Au and a-Si:H surfaces measured in four different instants; <i>Right</i> : Pictures taken from the microscope during the measurement.	69
4.17	Results obtained by fluorescence for longer molecules. <i>Left</i> : Plot of the signal on Au and a-Si:H surfaces measured in four different instants; <i>Right</i> : Pictures taken from the microscope during the measurement.	70
4.18	Plots of the fraction of adhered cantilevers as function of the length of the beam. <i>Left</i> : Standard release; <i>Right</i> : Release without using n-hexane.	70

4.19	Fit of the function of the work of adhesion when using the standard protocol and the release without n-hexane. The measurements of detachment length are also listed in the table.	71
4.20	Resonance spectrum of each cantilever. The intensity of the various harmonics cannot be directly compared because higher voltages were used for actuation for higher harmonics. <i>Inset:</i> Plot of a resonance peak with a Lorentz curve fit and the extracted parameters. . .	72
4.21	Plot of capacitance and resistance for each instant of time. The results were obtained in air by measuring a cantilever with 100 μm length. The black arrows are pointing the instants when the light of the microscope was turned on.	75
4.22	Plots of capacitance and resistance for each instant of time. The results were obtained in water by measuring two cantilevers with 120 μm length in two different channels. The black arrows are pointing the instants when the flow was turned on and off.	76

Nomenclature

Greek symbols

ϵ	Permittivity.
γ	Surface free energy.
κ	Radius of curvature.
λ	Linear density.
μ	Viscosity.
ν	Poisson's ratio.
ω	Radial frequency.
ψ	Vertical deflection of the cantilever.
ρ	Density.
σ	Surface stress.
τ	Shear stress.
ξ	Surface tension.
ζ	Damping ratio.

Roman symbols

d_0	Separation distance.
e^-	Charge of the electron.
F_e	Electrostatic force.
F_m	Meniscus force.
F_r	Restoring force.
F_v	Viscous force.
$h\nu_{em}$	Energy of the emitted photon.

$h\nu_{ex}$	Energy of the incident photon.
l_d	Detachment length.
Q_v	Volumetric flow rate.
R_0	Radius.
R_e	Reynolds number.
R_f	Flow resistance.
S_0	Ground state.
S_1	First excited state.
S'_1	Excited singlet state.
S_{Au}	Calculated signal on gold.
T_m	Melting temperature.
V_{pp}	Voltage peak-to-peak.
W_a	Work of adhesion.
x, y, z	Cartesian components.
$\dot{x}, \dot{y}, \dot{z}$	Velocity cartesian components.
A	Area of the surface of the cantilever.
AI	Average RGB intensity.
b	Damping coefficient.
C	Capacitance.
D	Characteristic length, diameter.
E	Young's modulus.
f	Frequency.
g	Gap distance.
h	Thickness of the cantilever.
I	Moment of inertia.
i	Current.
k	Spring constant.
L	Inductance.

l	Length of the cantilever.
M	Bending moment.
m	Mass.
P	Pressure.
Q	Quality factor.
q	Load.
R	Resistance.
S	Shear force.
t	Time.
U	Energy.
V	Voltage.
v	Velocity.
W	Work.
w	Width of the cantilever.

Subscripts

0	Vacuum.
\perp	Perpendicular.
C	Centroid.
d	Damped.
em	Electromechanical.
ft	Feedthrough.
i	In.
n	Mode number.
o	Out.
P	Parallel.
PI	Pull-in.
r	Relative.
res	Resonance.

S Series.

s Static.

vdW van der Waals.

Abbreviations

2D 2-Dimensional.

A Adenine.

a-Si:H Hydrogenated amorphous silicon.

AC Alternate current.

Al Aluminum.

Ar Argon.

Au Gold.

BSA Bovine Serum Albumin.

C Cytosine.

CCD Charged-Coupled Device.

CMOS Complementary Metal-Oxide-Semiconductor.

Cr Chromium.

DC Direct current.

DI Deionized.

DNA Deoxyribonucleic Acid.

DoF Degree of Freedom.

dsDNA double stranded DNA.

DUT Device Under Test.

DWL Direct Write Laser.

EDTA Ethylenediamine Tetraacetic Acid.

F Fluor.

FITC Fluorescein Isothiocyanate.

FWHM Full Width at Half Maximum.

G Guanine.

HDMS Hexamethyldisilazane.

HRP Horseradish Peroxidase.

INESC-MN Instituto de Engenharia de Sistemas e Computadores - Microsistemas e Nanotecnologias.

IPA Isopropyl Alcohol.

LoC Lab-on-Chip.

LoD Limit of Detection.

MEMS Micro Electro Mechanical Systems.

N Nitrogen.

NaCl Sodium Chloride.

O Oxygen.

P Phosphorus.

PA Sodium Polyacrilate.

PBS Phosphate Buffered Saline.

PCB Printed Circuit Board.

PDMS Polydimethylsiloxane.

PECVD Plasma-Enhanced Chemical Vapor Deposition.

PGMEA Propylene Glycol Monomethyl Ether Acetate.

PR Photoresist.

RF Radio Frequency.

RGB Red/Green/Blue.

RIE Reactive Ion Etching.

ROC Receiver Operating Characteristic.

S Sulfur.

SAM Self-Assembled Monolayer.

SPR Surface Plasmon Resonance.

ssDNA single stranded DNA.

Strept Streptavidin.

T Thymine.

TiW Titanium and Tungsten.
Tris Tris(hidroximetil)aminometano.
UV Ultraviolet.
Xe Xenon.

Chapter 1

Introduction

1.1 Motivation

The present situation in health care demands for new devices, capable of a faster detection of lower concentrations of a certain biomarker. Hence, a sooner diagnosis can be established and an appropriate treatment can be performed. For this purpose, a biosensor is a powerful tool to detect any biomarker or other type of biological material that may help in this process. Actually, not only health care would benefit from the development of improved biosensors, but also fields like process control in industry, environmental monitoring, genetics, biology and drug screening among others.

A generic biosensor is a device containing a biomolecular set that is capable of recognizing a given biological element in solution and transducing this recognition into a measurable signal. The first biosensor was described in 1962 by Clark and Lyons and it was intended for glucose monitoring. It used a platinum electrode covered with glucose oxidase acting as probe which produces peroxide in the presence of glucose and oxygen. A second electrode guarantees the transduction since its electrical properties are sensitive to the presence of peroxide. From this point forward, a lot of advances in chemistry, biology, electronics and nanotechnology allowed a fantastic progress towards new biosensors with improved sensitivity and faster responses.

An important aspect from the point of view of the industry is the production cost. The emergence of microfabrication was decisive for this sector to embrace mass production of micromachined sensors. Although the fabrication processes and materials used in microtechnology are expensive, the final cost of a single device can be very low due to the possibility of batch processing and miniaturization. A trendy set of devices within nano and microtechnology are the micro electromechanical systems (MEMS) comprising micromechanical sensors or actuators and microelectronic circuits. Such systems are known for their many and varied applications: temperature and air flow monitoring, detection of chemical and biological substances, energy harvesting, production of electrical components, optical displays and many others. When designed for biosensing, these structures are functionalized with a proper probe molecule which transduces the signal resulting from molecular recognition into a well defined mechanical behaviour, such as bending or resonance frequency shift. With an appropriate apparatus, it is possible

to translate the variations in the mechanical status of these structures into an electrical signal. An additional advantage is the possibility of integration with existing components such as CMOS technology given that the fabrication process and specifications are compatible.

The combination of MEMS with a system that is capable of handling the necessary fluids for biosensing allows the creation of a device with low consumption of biological material to be analysed and potentially a shorter detection time and also higher sensitivity also. Microfluidics is the sector of microtechnology that deals with this problem of fluid handling at a scale smaller than 1 mm. By using a net of microchannels, pumps, valves and other types of structures, one is able to guide, mix, separate or incubate a certain fluid in a microchip. It is even possible to create thin self-assembled monolayers (SAM's) of probes on the MEMS, eliminating the need of labelling the target molecules with fluorophores, radioactive isotopes or other molecules. This label-free detection is the strongest advantage of using MEMS in this device instead of other sensing structures. The major concern that is currently creating some constraints to this integration when applied to biosensing is the damping effect that a fluidic medium can induce in a mechanical structure under vibration. Furthermore, the incorporation of electrical circuits in a wet environment is a difficult task that can cause malfunctioning in the electrical components.

In the end, a system that is able to join both MEMS and microfluidics would benefit from the advantages of each technology and even allow multiplexing, turning it into a high-throughput sensor for label-free detection with a high sensitivity and response rate.

1.2 State of the art

The major advantage that places MEMS on top of the list of biosensors, along with surface plasmon resonance (SPR) systems, is their ability for label-free detection [1, 2, 3, 4]. In fact, also their exquisite mass resolution and fast response are very attractive for biosensing, thus MEMS would be advantageous for integration in diagnosis equipment [4, 5]. The sensitivity of a cantilever is currently quoted in the hundreds of fM [1, 4] which is already a low limit of detection (LoD).

Different approaches for thin film silicon MEMS fabrication can be employed. As a matter of fact, both bulk and surface micromachining can be used. Nevertheless, at INESC-MN it is preferred the second method because it allows the control of thickness and surface stress of the films which are important factors for MEMS fabrication. In surface micromachining, each layer of material is sequentially deposited and patterned using optimized parameters, while bulk is based on patterning of a pre-fabricated substrate. The common strategy used at INESC-MN is the deposition by radiofrequency plasma-enhanced chemical vapor deposition (RF-PECVD) of amorphous silicon [6, 7]. This deposition procedure is already optimized for MEMS applications due to previous studies on the parameters and conditions of deposition [8, 9]. Using this process, different structures such as cantilevers, bridges and plate resonators have been already studied in the past [10, 11, 12]. The tuneability accomplished through these previous studies allows the control of the residual surface stress on the film which is an undesired effect since it can cause stiction. In fact, multiple phenomena may induce the collapsing of the structure and some studies are provided along with techniques to assess the magnitude of the effect [13, 14, 15, 16].

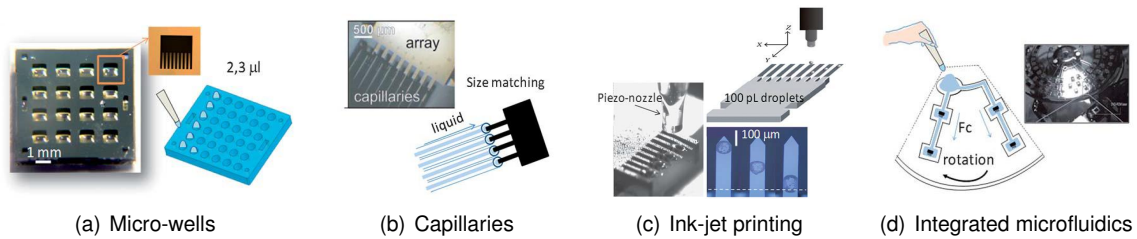


Figure 1.1: Types of interfaces used for fluid handling when proceeding for MEMS functionalization [3].

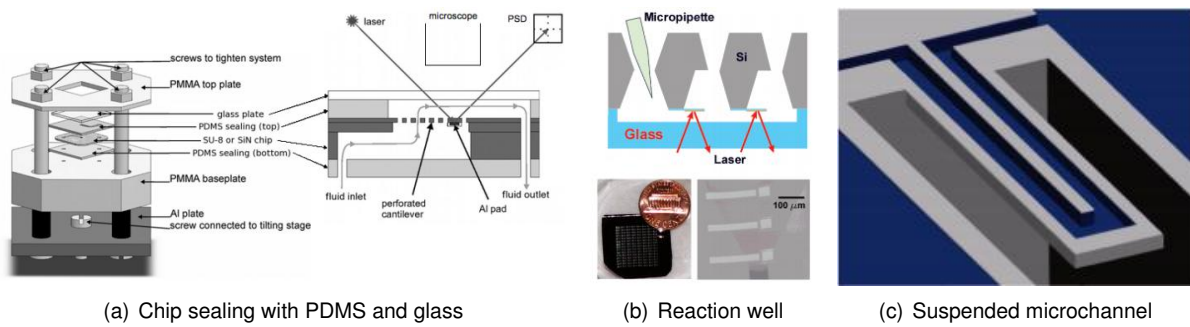


Figure 1.2: Different types of integration of microfluidics in MEMS [25, 26, 27].

Regarding the detection and measurement of the mechanical bending of a MEMS, different setups can be applied. It is possible to use either a capacitive [17] or optical [18] readout system currently installed at INESC-MN or a more ingenious one which includes detection of magnetic films through the incorporation of spin-valves [19]. Other groups also report piezoresistive [20] and Doppler vibrometry [21] detection among other types.

The so called lab-on-chip (LoC) integration which is defined by the incorporation of fluid handling, sensing and detection in the same chip, benefiting from the integration of microfluidics in the system [22]. For microfluidics it is preferable to use a transparent and elastic material like PDMS and the control of flow rates can easily be established by many types of pumps, such as syringe, peristaltic, electrokinetic or even MEMS pumps [23, 24].

In terms of integration of both technologies above mentioned, not much work has been developed until now. Usually, the main techniques used to handle fluids in the vicinities of MEMS are the ones summarized in Figure 1.1. Some attempts of incorporation of microfluidic channels with MEMS are reported (Figure 1.2), mainly using the dynamic mode of operation (resonance), however exhibiting weak outcomes since damping effects on the vibration of the resonators dominate. In [25], it is implemented a design of an array of cantilevers made of SiN and SU-8 (photoresist) inside a microfluidic channel using PDMS and glass. In a different way, in [26] the cantilevers are micromachined from a silicon layer so that it also creates a reaction well covered by glass, where the biological recognition occurs. A promising configuration that is currently being applied for the dynamic mode is the fabrication of the microchannels inside the suspended part of the MEMS [27]. This design allows an easier handling of the fluids and prevents the damping caused by a liquid medium since the medium around the resonator is vacuum.

Functionalization of MEMS is the aspect that shows more variability in terms of molecules and strategies used. There are lots of possibilities for targets such as: enzymes, proteins/peptides, lipid bilayers,

liposomes, cells, spores, bacterias, viruses, among others [28]. In this work, it was chosen DNA given its strong importance at a biological level and its many applications [5, 29]. The most common strategy for DNA immobilization is to use a gold layer on the MEMS surface which has a strong affinity to thiol groups. By using a probe DNA molecule modified with a thiol group, it is possible to attach it to gold [1, 30]. Some groups also report a significant improvement of the signal when using a passivation molecule for the bottom surface of the suspended structure of the MEMS [25, 31].

A recurrent statement of the authors reviewing this subject is that there are few accurate models predicting the connection between surface properties, surface stress and surface energy changes in the MEMS due to molecular interactions since the phenomena involved are very complex [2, 3, 4, 32]. It is also referred the huge variability of sensor characterization methods and it is pointed the inexistence of a universal method to facilitate the comparison between sensor performances, apart from the LoD. A solution is proposed: receiver operating characteristic (ROC) curves [2, 3]. This method relates the selectivity and sensitivity of the sensor by evaluating the quantity of true positives and false positives.

1.3 Objectives

Given the potentialities of MEMS and microfluidics, the aim of this thesis is to design and fabricate a device that combines both technologies efficiently. The versatility that MEMS fabrication allow in terms of geometry, materials and dimensions need to be properly analysed so that the purpose of biosensing is conveniently addressed. A thin film of amorphous silicon is used as structural material of the device that is fabricated on top of a glass substrate. The chosen MEMS structure is a cantilever working in the static operation mode. Such structure is easily bendable and its performance is not affected by fluidic damping effects if working in the static mode. The challenge here is to design a robust and reliable structure, maximizing its sensitivity when a surface stress is applied, while aiming for a multiplexed device with multiple sensors and references. Microfluidic structures should also be properly designed without compromising the integrity and reliability of the MEMS.

As a second objective, there is the necessity of defining a reactive layer on the surface of the cantilever which must be able to recognize a certain molecule in a liquid medium. The target molecule is a specific single stranded DNA (ssDNA) that needs to be selectively captured by an appropriate probe. Such probe is immobilized on the cantilever, creating a SAM. In this stage, extensive biological tests are crucial to understand how this system can be tuned according to the established purpose. A complete study involving the probe and target molecules subjected to different conditions of salts, concentrations, incubation and flow rates is essential in order to obtain the ideal conditions for probe immobilization and target capturing.

Finally, using the existent systems for MEMS readout, one should be able to characterize the final structures in terms of performance, sensitivity, reliability and robustness. This way, it is possible to establish a comprehensive comparison between the existent sensors and the ones produced in this project. Apart from the measurements in vacuum, the behaviour of the system in a liquid medium is also intended to be studied because this is the significant medium where the biological recognition occurs.

If all these objectives are successfully accomplished, the concept of combining MEMS and microfluidics is validated and new horizons and potentialities may arise.

1.4 Thesis Outline

The description of the work involved in this thesis is divided by chapters, starting with the present one which is dedicated to a brief explanation on the motivation for this project and a summarized overview of the previous studies on some relevant fields of science and technology. The main objectives and challenges are also presented for a further comprehension.

In chapter 2, it is possible to find all the formalism necessary to understand the subsequent contents in this thesis. The relevant theoretical background is presented, starting with the characterization of MEMS, the physical principles involved in its operation and the various effects that can affect its performance. An insight into microfluidics principles and DNA properties is also included in this section.

All the methods that were employed for sensor fabrication and characterization are listed and described in chapter 3, as well as the materials and protocols for biological assays. Details on film deposition, etching techniques and photolithography are presented along with the materials and conditions used for the fabrication of MEMS and microfluidics devices. The processes used for integration of both technologies are also explained. The last subsection covers the type of setups that were used for the measurements of the devices and for the biological tests.

Chapter 4 includes all the results obtained during the development of this thesis. A preliminary subchapter shows the resultant devices that were fabricated for the different stages of the work. The subsequent one lists the main results from the biological test assays, comparing different conditions for probe immobilization and DNA hybridization and establishing the optimal protocol to be used in the biosensors. Afterwards, the initial results from the characterization of the structures in air and vacuum are presented, followed by the ones obtained in a liquid medium and using the protocol previously established.

Finally, in chapter 5, the conclusions and suggestions for future work are discussed as a way of pursuing an improved system.

Chapter 2

Background

In this chapter, the main physical principles involved in MEMS operation are explained. The mathematical formalism of the mechanical behaviour of cantilevers operating in both modes is presented along with the definition of some important parameters. A comparison between the mechanical and electrical models is done and it is explained the principle of electrostatic actuation of a cantilever. Considerations about parasitic capacitances and a model to determine the maximum voltage that can be applied are also included. Afterwards, a small section covers the main aspects in microfluidics in terms of typical flow behaviours and characteristics. Finally, some general characteristics of DNA are presented since this is the biological molecule used in this work.

2.1 Physical principles and operation modes of a cantilever

A cantilever is a type of MEMS characterized by a suspended beam that is anchored at one end while the opposite one is free to move as depicted in Figure 2.1. Since it is able to deflect and oscillate, it is commonly categorized as a microresonator system. As any oscillatory system, cantilevers can be described using a spring-mass model. In fact, when a force is applied on the cantilever's surface, it will bend and its vertical deflection is proportional to the magnitude of the force as stated by Hooke's law:

$$F_r = k\psi_{max} \tag{2.1}$$

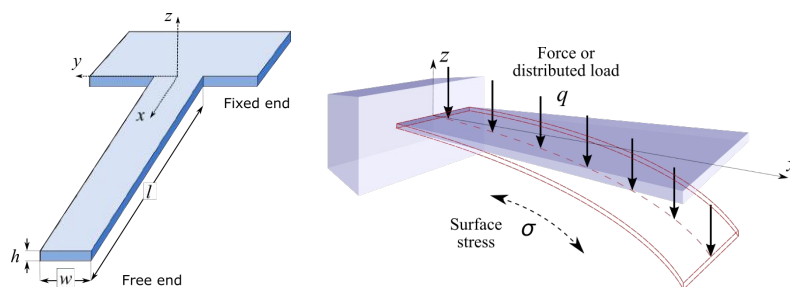


Figure 2.1: Schematics of a free cantilever without residual stress (*left*) and a deflected cantilever due to surface stress and/or a force acting on the tip (*right*).

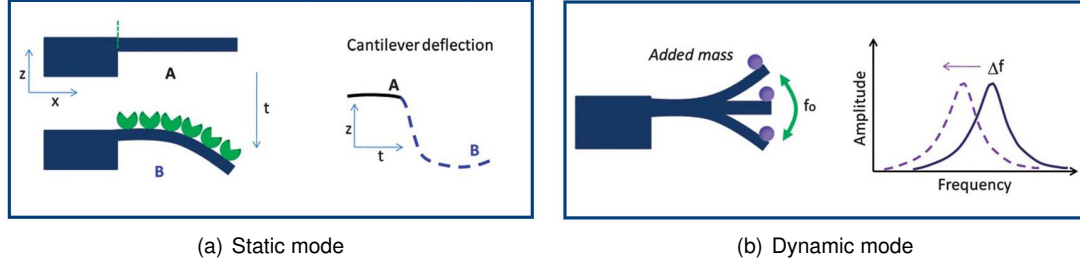


Figure 2.2: Different two modes of operation of a cantilever. In the static mode, the adsorption of molecules creates a variation of the surface stress causing the deflection of the cantilever. In the dynamic mode, by adding mass to the beam, its resonance frequency is shifted towards lower values. Images adapted from [3].

where ψ_{max} represents the vertical deflection on the tip of the beam, k is the spring constant of the cantilever and F_r is the restoring force. If one is interested in measuring the deflection of the cantilever's tip, the spring constant defines its sensitivity since it is a measure of stiffness. For the same applied force, a stiffer beam will not bend as much as a more flexible one, which means it has a lower sensitivity. Furthermore, the spring constant of a rectangular cantilever is known to be dependent on the used materials and the established geometry:

$$k = \frac{3EI}{l^3} \quad (2.2)$$

with E being the Young's modulus of the material and I the moment of inertia given as:

$$I = \frac{wh^3}{12} \quad (2.3)$$

where w , h and l are the width, thickness and length of the cantilever, respectively. By analyzing the variables in both equations, it is possible to state that larger aspect ratios in respect to the length will contribute for a larger sensitivity.

Depending on the existence of an external force driving the cantilever motion, it can either be working in the *static* or *dynamic* operation modes (Figure 2.2). In the first one, the cantilever is solely subjected to a differential surface stress responsible for the deflection of the cantilever. In the other case, an external force, usually arising from an electrostatic field, induces a forced oscillation so that the resonance frequency can be evaluated.

2.1.1 Static mode

The most commonly used operation mode in biosensing, also called surface stress mode, is the the static one. In this case, a variation in the surroundings or directly on top of the cantilever's surface creates a surface stress that causes the beam either to stretch or compress in that region. In biosensing applications, this effect is caused by the adsorption of molecules onto the surface of the cantillever. Such bending reduces the surface free energy of its lattice structure. Shuttleworth equation [33] for isotropic materials expresses this relation between surface stress, σ , and surface free energy, γ :

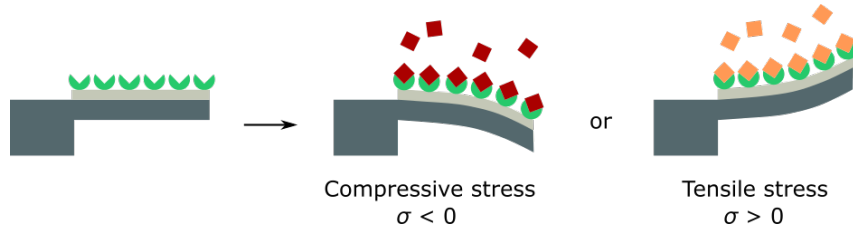


Figure 2.3: Schematics of a cantilever working in the static mode under tensile and compressive stresses. An upwards deflection is characteristic of tensile stresses while compressive stress originates a downwards deflection.

$$\sigma = \gamma + \frac{\partial \gamma}{\partial \epsilon} \quad (2.4)$$

where the surface strain is defined as the ratio between the variation in surface area and the total area, $\partial \epsilon = \partial A/A$. Nevertheless, for a more practical approach, it is used the Stoney's formula [34] which relates a differential surface stress with the vertical deflection of the tip of the cantilever, ψ_{max} :

$$\Delta \sigma = \frac{Eh^2}{3(1-\nu)l^2} \psi_{max} \quad (2.5)$$

with ν representing the Poisson's ratio and $\Delta \sigma$ expressing the difference in surface stress between the top and bottom surfaces of the cantilever. In fact, if both surfaces are under the same stress, the deformations will cancel and no deflection will happen. However, for an asymmetrical surface stress, the cantilevered structure will bend either up or downwards, depending on the sign of the differential stress (Figure 2.3). For example, if the cantilever bends upwards, it is because the stress is *tensile*, otherwise it bends downwards and the stress is said to be *compressive*. These designations arrive from the relation for the reversible work $dW = \sigma \times dA$ which for spontaneous processes is defined as negative, $dW < 0$. If the stress is positive, then dA needs to be negative which means that the surface will tend to compress while for negative stresses, dA is positive so the surface will expand [32].

At microscale, systems are generally characterized by a low Reynolds number which represents the ratio between inertial and viscous forces as presented in Section 2.2. This means that the effects of inertial forces, such as the gravitational one, are considered negligible. For this reason, it is not possible to measure mass with cantilevers, at least not using the static mode. This mode is preferable for measuring the magnitude of interactions between molecules. For example, if one intends to measure the relative concentration of a specific highly charged molecule in a medium, it is possible to capture that molecule with an appropriate probe and due to the electrostatic interactions between the targets, a different stress will arise on the surface of the cantilever. If the concentration of targets is higher, the number of captured molecules is also higher and the stress generated increases as well as the displacement of the beam.

The deflection of the cantilever can be described using the equation of Euler-Bernoulli for a general beam under the effect of an applied load [35, 36]:

$$\frac{d^2}{dx^2} \left(EI \frac{d^2 \psi}{dx^2} \right) = q \quad (2.6)$$

where $\psi(x)$ is the function of the curve that represents the deflection in z at a certain point x and q is the load applied on the beam (Figure 2.4). In a symmetrical and uniform rectangular cantilever the product EI (flexural rigidity) is constant, so one obtains:

$$EI \frac{d^4 \psi}{dx^4} = q \quad (2.7)$$

It is possible to define different quantities in terms of the derivatives of the deflection curve [37]. The first derivative, $\frac{d\psi}{dx}$, is simply the slope of the beam while the second one describes its radius of curvature, κ :

$$\kappa \equiv \frac{1}{R_0} = \frac{\frac{d^2 x}{dz^2}}{\left[1 + \frac{dx}{dz}\right]^{\frac{3}{2}}} \approx \frac{d^2 \psi}{dx^2} \quad (2.8)$$

The approximation is valid for beams with a large radius, R_0 , which is a characteristic of cantilevers. An important quantity called bending moment, M , can be defined as function of this curvature:

$$M = -EI \frac{d^2 \psi}{dx^2} \quad (2.9)$$

The quantity corresponding to the applied force on the cantilever, also called shear force, S , is simply given by the derivative of the bending moment:

$$S \equiv \frac{dM}{dx} = -EI \frac{d^3 \psi}{dx^3} \quad (2.10)$$

With this relations well established and specially using the differential equation 2.7, it is possible to find the slope and maximum deflection of the cantilever after applying the appropriate boundary conditions to the system. First of all, lets consider a rectangular cantilever with an uniformly distributed load, q , on its surface. The corresponding shear force and bending moment at a distance x from the tip of the beam are given as $S = \int -q dx = -qx$ and $M = \int S dx = -\frac{qx^2}{2}$, respectively. By substituting this result in Equation 2.9, one obtains:

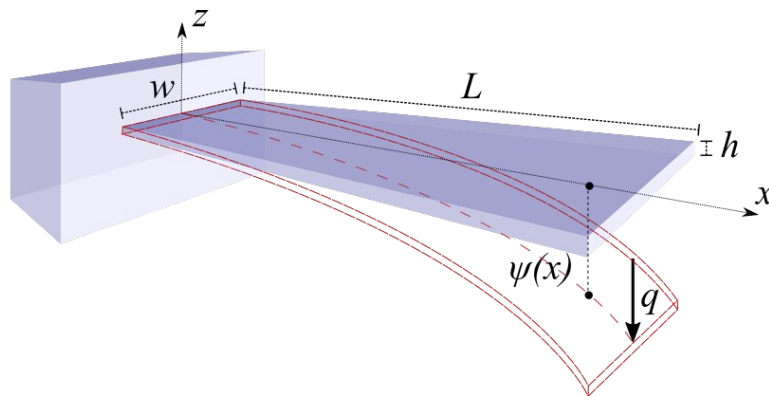


Figure 2.4: Schematics of a cantilever on the plane xOz showing the deflection in z at a certain point x of the beam. The beam is fixed at $x = 0$ and free to move at $x = L$ where the deflection is maximum, ψ_{max} .

$$EI \frac{d^2\psi}{dx^2} = -\frac{qx^2}{2} \quad (2.11)$$

By successively integrating the equation in respect to dx , it reduces to:

$$\begin{cases} EI \frac{d\psi}{dx} = -\frac{qx^3}{6} + A \\ EI\psi = -\frac{qx^4}{24} + Ax + B \end{cases} \quad (2.12)$$

where A and B are constants of integration. To determine these constants, the following boundary conditions are applied when the cantilever is operating in the static mode:

$$\begin{cases} \psi(x = l) = 0 \\ \frac{d\psi}{dx}(x = l) = 0 \end{cases} \quad (2.13)$$

These conditions establish that the cantilever is fixed at $x = l$ so that it cannot bend in this point. The substitution of these conditions in the integrated equations returns the expressions for the constants:

$$\begin{cases} A = \frac{ql^3}{6} \\ B = -\frac{ql^4}{8} \end{cases} \quad (2.14)$$

The final equations for the deflection and slope of the cantilever can be evaluated for the free end ($x = 0$) which is the position that shows the highest values:

$$\begin{cases} \psi_{max} = -\frac{ql^4}{8EI} \\ \frac{d\psi}{dx}(max) = \frac{ql^3}{6EI} \end{cases} \quad (2.15)$$

By knowing the deflection at the tip of the cantilever, it is possible to substitute its result in Stoney's formula and to find the value of applied surface stress. This way, one is able to relate the surface stress with the deflection of the cantilever since the stress on a surface for a linear isotropic material can be described in terms of the bending moment, validating the conjugation of both equations.

2.1.2 Dynamic mode

Instead of tracking the deflection when a constant load is applied, it is also possible to actuate the cantilevers in such a way that it induces an oscillation. For this reason, cantilevers are also included in the class of microresonators. In a simplified system, without external and damping forces, the oscillation has a natural frequency, ω_{nat} , which is given in terms of the elastic constant, k , and mass, m , of the structure:

$$\omega_{nat} = \sqrt{\frac{k}{m}} \quad (2.16)$$

Nonetheless, since viscous forces have such a strong effect at this scale, it is necessary to include the damping and external forces (for actuation). In such conditions, the motion is described by the

differential equation of a typical damped harmonic oscillator [38, 39] as suggested in Figure 2.5:

$$m\ddot{\psi}(t) + b\dot{\psi}(t) + k\psi(t) = F(t) \quad (2.17)$$

where b is the damping coefficient and ψ represents the vertical displacement of the mass in respect to time, t . It is also possible to define a damping ratio, ζ , which characterizes the magnitude of damping occurring in the system:

$$\zeta = \frac{b}{2m\omega_{nat}} = \frac{b}{2\sqrt{mk}} \quad (2.18)$$

If one introduces the definitions of natural frequency and damping ratio into Equation 2.17, it can be reformulated as:

$$\ddot{\psi}(t) + 2\zeta\omega_{nat}\dot{\psi}(t) + \omega_{nat}^2\psi(t) = F(t) \quad (2.19)$$

Because the cantilever is assumed to be a symmetrical and homogeneous structure and since the amplitude of oscillation is very small, it is valid to consider a single degree of freedom (DoF) along the vertical axis zz . In a real system, a three dimensional analysis would be necessary to describe the distribution of mass in the beam and specific material properties as well as a full analysis of all vibration modes (flexural, torsional, extensional, etc). However, for this purpose and this specific structure, a 2D model with a single DoF is enough to obtain the general parameters of the motion.

Using now the full equation of Euler-Bernoulli with dependence in time and assuming a thin rectangular beam ($l/h \geq 10$) with a uniform distribution of mass, one may rewrite it as [40, 41]:

$$EI \frac{\partial^4 \psi(x, t)}{\partial x^4} + \lambda_m \frac{\partial^2 \psi(x, t)}{\partial t^2} \quad (2.20)$$

with $\psi(x, t)$ varying with time, t , and the position along the beam, x , while the linear mass density of the beam is given as the product of the density of the material and its cross sectional area, $\lambda_m = \rho A$. To find the vibration frequencies correspondent to this motion, one must solve the previous equation by firstly assuming a general solution of the type:

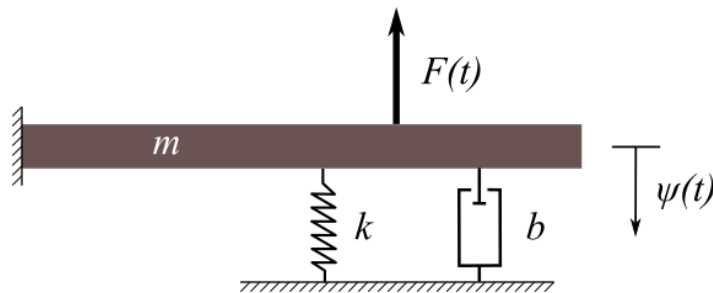


Figure 2.5: Mechanical model of a cantilever operating in the dynamic mode. It is similar to the damped harmonic oscillator driven by a certain force $F(t)$.

$$\psi(x, t) = \sum_n \Psi_n \left(\frac{x}{l} \right) [A_n \cos \omega_n t + B_n \sin \omega_n t] \quad (2.21)$$

where $\Psi_n \left(\frac{x}{l} \right)$ corresponds to the shape function of the oscillation, ω_n is the radial frequency and A_n and B_n are constants all of them relative to the n^{th} vibration mode. The integration of the generic solution over the infinite vibration modes and subsequent substitution in Equation 2.20 returns:

$$\Psi_n'''' \left(\frac{x}{l} \right) - k_n^4 \Psi_n \left(\frac{x}{l} \right) = 0 \quad (2.22)$$

For convenience, it was defined $k_n^4 = \frac{\omega_n^2 \rho A l^4}{EI}$. Afterwards, a trial solution of the type $\Psi_n = e^{\lambda x/l}$ is applied in the previous equation:

$$\lambda^4 - k_n^4 = 0 \quad (2.23)$$

With this equation, the solutions calculated for the auxiliary variable are $\lambda = \{k_n, -k_n, ik_n, -ik_n\}$. This way, the solution of the shape function can be rewritten as:

$$\begin{aligned} \Psi_n \left(\frac{x}{l} \right) &= A e^{k_n \frac{x}{l}} + B e^{-k_n \frac{x}{l}} + C e^{ik_n \frac{x}{l}} + D e^{-ik_n \frac{x}{l}} = \\ &= A \sin \left(k_n \frac{x}{l} \right) + B \cos \left(k_n \frac{x}{l} \right) + C \sinh \left(k_n \frac{x}{l} \right) + D \cosh \left(k_n \frac{x}{l} \right) \end{aligned} \quad (2.24)$$

For a general cantilever anchored at $x = 0$ and free at $x = l$, the corresponding boundary conditions are given as:

$$\begin{cases} \psi(x=0) = 0 \\ \psi'(x=0) = 0 \\ \psi''(x=l) = 0 \\ \psi'''(x=l) = 0 \end{cases} \quad (2.25)$$

Consequently, if each derivative of the shape function is calculated with the expression obtained in 2.24, the result will be a system of four equations that can be summarized in its matrix form as:

$$\begin{pmatrix} 1 & 0 & 1 & 0 \\ 0 & 1 & 0 & 1 \\ -\cos(k_n) & -\sin(k_n) & \cosh(k_n) & \sinh(k_n) \\ \sin(k_n) & -\cos(k_n) & \sinh(k_n) & \cosh(k_n) \end{pmatrix} \begin{pmatrix} A \\ B \\ C \\ D \end{pmatrix} = 0 \quad (2.26)$$

The calculation of nontrivial solutions requires the determinant of the matrix to be zero. Following this reasoning, one ends up with the transcendental frequency equation:

$$\cosh(k_n) \cos(k_n) + 1 = 0 \quad (2.27)$$

that can be solved numerically for the lower order modes. These roots correspond to the eigenvalues k_n plotted in Figure 2.6 and since the cosine is a periodic function while the hyperbolic cosine grows exponentially with an increasing k_n , one has a quantity of solutions equal to the number of periods of the cosine function. For high order modes ($n \geq 3$) it is assumed that $\cos(k_n) \approx 0$. After computing Equation 2.27 it is possible to define the eigenvalues k_n for the different n modes:

$$k_n = \begin{cases} 1.8751 & , n = 1 \\ 4.6941 & , n = 2 \\ 7.8548 & , n = 3 \\ \frac{(2n-1)\pi}{2} & , n \geq 4 \end{cases} \quad (2.28)$$

Having these values calculated, it becomes possible to determine the radial vibration frequency for each mode, ω_n , just by substituting the numerical results in:

$$\omega_n = \frac{k_n^2}{l^2} \sqrt{\frac{EI}{\rho A}} \quad (2.29)$$

To reach the expression of the resonance frequency of the system, for a specific mode n , one must divide the radial frequency by 2π . If the moment of inertia (Equation 2.3) is substituted along with the area $A = h \cdot w$, the resonance frequency, f_{res} , becomes:

$$f_{res} = \frac{k_n^2}{2\pi l^2} \sqrt{\frac{EI}{\rho A}} = \frac{k_n^2}{2\pi \sqrt{12}} \cdot \frac{h}{l^2} \sqrt{\frac{E}{\rho}} \quad (2.30)$$

As expected, the resonance frequency shows dependence with the properties of the material, namely its Young's modulus and density, and also with the dimensions of the cantilever, being the length the most influential one.

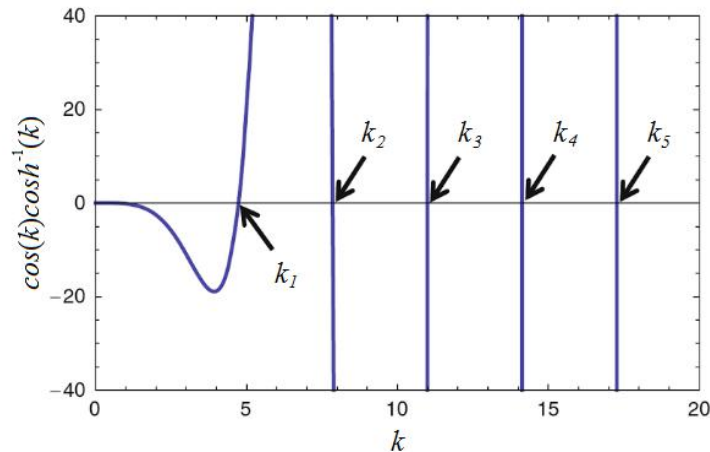


Figure 2.6: Plot of the roots of the frequency equation 2.27 for a cantilever. Image adapted from [41].

2.1.3 Energy dissipation

As stated before, the damping effect is an important issue to consider in microresonators. Actually, there are multiple processes occurring simultaneously that contribute for energy dissipation and consequently damping of motion. Depending on the magnitude of the total damping, the oscillation can exhibit different outcomes [39]. For systems with a low damping ratio ($\zeta < 1$), also called *underdamped*, although the oscillatory motion will remain with decreasing amplitude, its frequency is changed:

$$\omega_d = \omega_n \sqrt{1 - \zeta^2} \quad (2.31)$$

where ω_d is the damped radial frequency. On the contrary, when there is no oscillation and the motion corresponds to an exponential decay, the system is said to be *overdamped*, which means that the damping ratio is high ($\zeta > 1$). The intermediate case ($\zeta = 1$) establishes the border between the previous ones and it is typical of *critically damped* oscillators. The different behaviours are summarized in the plot of Figure 2.7

Another parameter that is intrinsically linked with the damping ratio is the quality factor, Q :

$$Q = \frac{1}{2\zeta} = \frac{\sqrt{km}}{b} \quad (2.32)$$

This is also a dimensionless parameter that relates the energy that is available for the resonator with the energy that is lost during oscillation by dissipation mechanisms:

$$Q = 2\pi \frac{\text{Average energy stored}}{\text{Energy lost during operation}} \quad (2.33)$$

In the end, it is valid to say that the Q factor is also a measure of damping. In MEMS, it is desired a higher Q factor since it means that less energy is being dissipated allowing a lower power operation and a higher sensitivity and precision [43]. In a frequency spectrum, this parameter is determined by the “sharpeness” of the resonance peak. An experimental method called “-3dB bandwidth method” or “half-power method”, depending on the references, is commonly used to estimate the Q factor as function of the full width at half maximum (FWHM) of the resonance peak in the spectrum [42]:

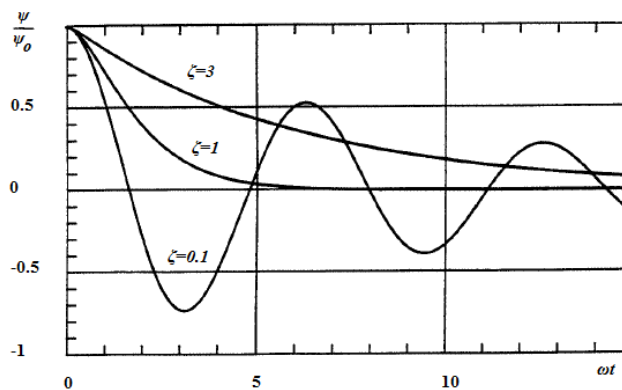


Figure 2.7: Plot of three different outcomes in a damped harmonic oscillator based on the value of the damping ratio. Image adapted from [42].

$$Q \approx \frac{f_{res}}{\Delta f} = \frac{f_{res}}{\Delta f_{-3dB}} \quad (2.34)$$

In the previous equation, Δf_{-3dB} is the frequency bandwidth limited by the points correspondent to $1/\sqrt{2}$ of the maximum amplitude response ($-3dB$ bandwidth) which by definition is where the resonance frequency, f_{res} , is located in the spectrum. The graphical approach is exemplified in Figure 2.8.

In MEMS, the dissipation mechanisms can be divided in two different groups: the intrinsic and extrinsic ones [44]. *Intrinsic* mechanisms are the ones that arise from the design of the structure and from the properties of the materials used to fabricate the microresonators. Support damping is one example which is characterized by energy losses through the anchors of the resonator into the substrate. This results from the stress applied in the anchors by the deflection of the resonator. Here, the design of the anchors and their location with respect to the different parts of the resonator will define the quantity of energy that is lost. Thermoelastic damping is another type of intrinsic damping which varies with the material used for the resonator. In this case, due to deflection/deformation, it is created an irreversible heat flow across the thickness of the resonator that dissipates some energy.

In the other hand, there are the *extrinsic* mechanisms which are a consequence of the interactions between the resonator and the surroundings. The damping due to the presence of a medium other than vacuum is an extrinsic mechanism that combines three different damping sources: Stokes damping, squeeze-film damping and acoustic damping. The first one, also called viscous damping, exists due to the Stokes drag force acting against the direction of motion. The resistance exhibited when compressing and pushing the fluid that is located in the gap between the substrate and the resonator refers to the squeeze-film damping. Finally, the acoustic damping comprises the effect of losing energy by excitation of the fluid.

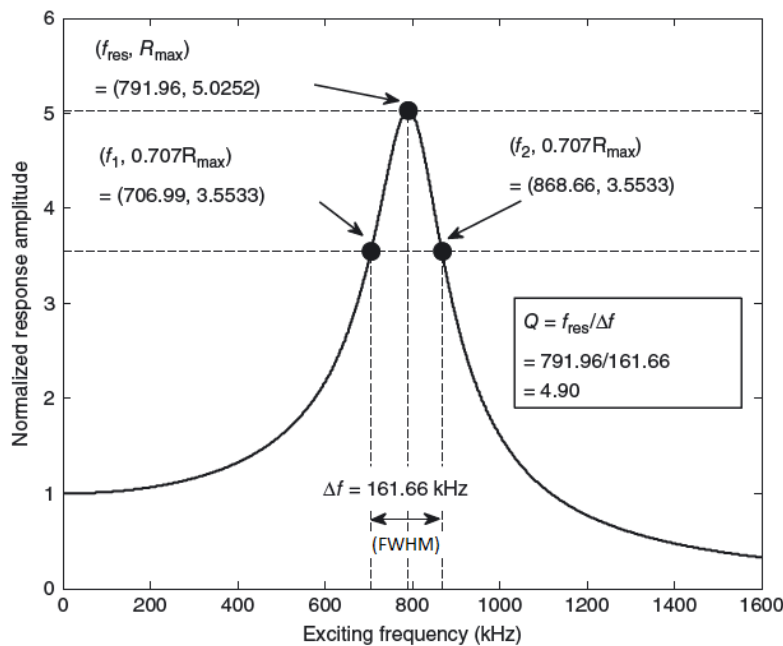


Figure 2.8: Plot of a general resonance spectrum and the corresponding calculation of the Q factor. Image adapted from [39].

All the mechanisms listed above act independently and they can occur simultaneously. Typically, the total Q factor is given by the summation of all the mechanisms. However, when one of them is much stronger, it is possible to treat that one as the only contribution, as approximation. In biosensing, usually the effect of viscous damping due to the presence of a liquid medium dominates largely, for that reason it is possible to consider the simpler model in Figure 2.5. Given the small dimensions of MEMS and its high surface to volume ratio, it becomes difficult to surpass these effects in air and water, increasing the potential of static mode measurements for biosensing instead of the dynamic mode ones.

2.1.4 Electrical model of the cantilever

A simple damped harmonic oscillator can also be described by an electrical equivalent which is useful to consider when integrating with electronic readout systems [45]. For such purpose, the cantilever must include one electrode on its beam and another one on the substrate, creating a parallel plate capacitor. The equivalent electrical model comprises a resistor, a capacitor and an inductor connected in series as shown in Figure 2.9(a).

A second order differential equation can be written using the RLC model in which the main variable with dependence on time is the current passing through the components, $i(t)$:

$$i''(t) + \frac{R}{L}i'(t) + \frac{1}{LC}i(t) = 0 \quad (2.35)$$

where R , C and L correspond to the resistance, capacitance and inductance, respectively. Using this renewed equation, it is possible to redefine the quantities in Equations 2.16, 2.18 and 2.32:

$$\omega_{nat} = \frac{1}{\sqrt{LC}}; \quad \zeta = \frac{R}{2} \sqrt{\frac{C}{L}}; \quad Q = \frac{1}{R} \sqrt{\frac{L}{C}} \quad (2.36)$$

In fact, if one is interested in studying a more realistic resonator, it is necessary to include the contribution of parasitic capacitances. Figure 2.9(b) shows the improved model including the capacitances arriving from the intrinsic MEMS capacitance, wiring, packaging and characterization setup. This is the Butterworth-van-Dyke model and it takes into consideration the contribution of the static and parasitic capacitances by adding a feed-through capacitor, C_{ft} , in parallel to the RLC set [45, 46]. The new components are given as:

$$C_s = \frac{\epsilon_r \epsilon_0 l w}{g}; \quad C_m = \frac{\mu_{em}^2}{k}; \quad L_m = \frac{m}{\mu_{em}^2}; \quad R_m = \frac{\sqrt{km}}{\mu_{em}^2 Q} \quad (2.37)$$

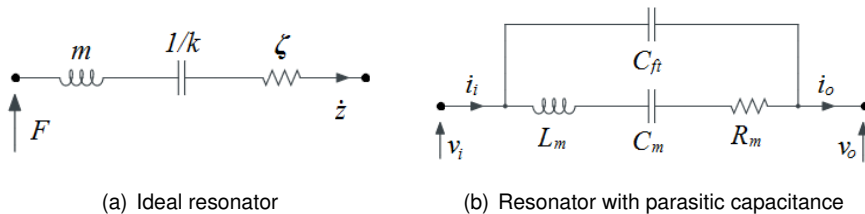


Figure 2.9: Schematics of the equivalent electrical models for a resonator.

where C_s is the static capacitance of the structure, g is the gap distance between the structure and the substrate, ϵ_r is the relative permittivity of the medium, ϵ_0 is the permittivity in vacuum and μ_{em} is the electromechanical coupling factor which can be simplified for small deflections ($g \gg z(t)$):

$$\mu_{em} = V_{DC} \frac{\partial C(z)}{\partial z} = V_{DC} \frac{\epsilon_r \epsilon_0 l w}{[g - z(t)]^2} \approx V_{DC} \frac{\epsilon_r \epsilon_0 l w}{g^2} \quad (2.38)$$

where it was used the following definition for the capacitance, assuming that the beam is maintained parallel to the bottom electrode (small deflections):

$$C(z) = \frac{\epsilon_r \epsilon_0 l w}{g - z(t)} \quad (2.39)$$

Because there is an additional line in the model containing the feed-through capacitor, another resonance frequency can be obtained. This way, both parallel, f_p , and series resonance frequencies, f_s , are defined as functions of the various components:

$$f_s = \frac{1}{2\pi} \sqrt{\frac{1}{L_m C_m}}; \quad f_p = \frac{1}{2\pi} \sqrt{\frac{1}{L_m \frac{C_m C_{ft}}{C_m + C_{ft}}}} \quad (2.40)$$

In fact, the series resonance frequency is a mechanical and electrical phenomenon, while the parallel resonance frequency only exists in the electrical domain.

2.1.5 Pull-in voltage model

In order to maintain the oscillatory motion of a damped resonator, it is necessary an external driving force capable of transferring enough energy to the system. The forced oscillation is known to exhibit different amplitudes depending on the driving frequency. If this frequency matches the natural frequency of the resonator, then it is reached a maximum in amplitude which corresponds to the resonance.

Cantilevers are commonly actuated by electrostatic forces acting on the beam. When the structure is composed by two electrodes, one at the beam's surface and the other one on the substrate, and a differential voltage is applied, it is generated an electrostatic field in between. Along with this field, an attractive force is created, pulling the beam of the cantilever towards the bottom electrode which is fixed on the substrate. If the differential voltage applied on the terminals only has a direct current (DC) component, the beam reaches an equilibrium state and only a deflection can be monitored. However, if an additional alternate current (AC) is applied, the intensity of the attractive force changes periodically with a certain frequency. This way, the capacitance arising between both electrodes also changes periodically. Using the electrodynamics formalism, it is possible to calculate the energy stored in this capacitor, U :

$$U = \frac{1}{2} C(z) V^2(t) = \frac{1}{2} \frac{\epsilon_r \epsilon_0 \omega l}{g - z(t)} (V_{DC} + V_{AC} \cos(\omega t))^2 \quad (2.41)$$

where it was used the approximation of capacitance for small deflections and a time-dependent potential comprising both DC and AC components at the frequency ω . The corresponding electrostatic force, F_e ,

is obtained by differentiating the energy with respect to the vertical position of the beam, z :

$$F_e = -\frac{1}{2} \frac{dC(z)}{dz} V^2(t) = -\frac{1}{2} \frac{\epsilon_r \epsilon_0 w l}{(g - z(t))^2} (V_{DC} + V_{AC} \cos(\omega t))^2 \quad (2.42)$$

After calculating the binomial relative to the potential, the attractive force is defined as:

$$F_e = -\frac{1}{2} \frac{dC(z)}{dz} V^2(t) = -\frac{1}{2} \frac{\epsilon_r \epsilon_0 w l}{(g - z(t))^2} \left(V_{DC}^2 + 2V_{DC}V_{AC} \cos(\omega t) + \frac{V_{AC}^2}{2} + \frac{V_{AC}^2 \cos(2\omega t)}{2} \right) \quad (2.43)$$

From Equation 2.43, it is concluded that the force acting on the resonator has three different components: the static deflection, the oscillation at the excitation frequency, ω , and the oscillation at double the excitation frequency, 2ω . Any increase in V_{DC} causes not only an increase in the static deflection but also an amplification of the oscillation at the excitation frequency. On the contrary, an increase in V_{AC} results in a larger deflection and amplification of the component at double the excitation frequency. If one is interested in eliminating the last component, it is important to decrease the AC voltage as much as possible. In the limit of very large DC component when compared with AC ($V_{DC} \gg V_{AC}$) and for small deflections ($g \gg z(t)$), the force acting on the resonator is simplified to:

$$F_e \approx -\frac{1}{2} \frac{\epsilon_r \epsilon_0 w l}{g^2} (V_{DC}^2 + 2V_{DC}V_{AC} \cos(\omega t)) \quad (2.44)$$

When dealing with electrostatic actuation, an important effect that must be accounted is the *pull-in*. This term refers to the collapsing of the resonator due to an excessive electrostatic force which may lead to permanent damaging of the structure. This effect is the result from the force balance between the electrostatic force and the elastic restoring force, which are the two forces applied in the resonator. The interactions that are being neglected, for simplicity, are mentioned in the following subsection 2.1.6. When the sum of the forces acting on the structure is zero ($\sum F = F_e + F_r = 0$), by substituting the corresponding definitions for each force (Equations 2.1 and 2.42), it is possible to determine the deflection, $z(t)$:

$$-\frac{\epsilon_r \epsilon_0 w l V^2}{2(g - z)^2} + kz = 0 \quad (2.45)$$

When the restoring force is larger than the electrostatic one, the resonator is able to return to its initial position. Otherwise, it suffers pull-in due to an excessive elastic constant and/or voltage. Different models are currently used, accounting for different small variations in details. The one used in this work is deduced in [47] and it is governed by the equation:

$$V_{PI} = 2\sqrt{\frac{2EIg^3}{3\epsilon_r \epsilon_0 w l^4}} \quad (2.46)$$

Other pull-in models can be established, accounting for other effects. With this estimation it is possible to predict the limit for the unstable regime. This way, it is guaranteed the control and integrity of the structure during its operation.

2.1.6 Stiction effect

One of the fundamental problems of MEMS is the occurrence of stiction. This is the phenomenon related with the effect of adhesion forces on suspended structures when they touch neighboring surfaces and they can be divided in two categories: release stiction and in-use stiction. The first one occurs during the last step of MEMS fabrication using surface micromachining in which a sacrificial layer is dissolved (wet etch) using a liquid chemical compound. The other one occurs when operating the MEMS and it is specially critical when using electrostatic actuation. The effect is characterized by the collapsing of the suspended structure when adhesion is sufficiently strong, leading in most of the cases to a permanent adhesion to the substrate. Commonly, stiction is originated due to capillary, electrostatic, hydrogen bonding and van der Waals forces which gain a strong intensity at microscale. In fact, when comparing with the gravitational force which decreases with the cubed characteristic length, adhesion forces have such a larger magnitude because they decrease linearly with this parameter. Capillary forces arise usually due to the hydrophilic nature of the surfaces, while electrostatic interactions are originated by charge accumulation on insulating surfaces. As a matter of fact, a comprehensive physical analysis of the problem of capillary forces acting on microstructures was exhaustively examined by Mastrangelo and Hsu in 1993 [48, 49]. Hydrogen bonding and van der Waals forces are also considerable but they do not exhibit such high magnitudes as the previous enumerated interactions.

This effect creates huge barriers against the development of this technology since it decreases the limit of production yield, the sensitivities and lifetime of the devices. A popular method used for quantifying stiction is the work of adhesion study [13, 14, 15]. To perform it, an array of structures is fabricated with different dimensions and after release, it is observed the limit of dimensions that can be employed (Figure 2.10). For example, a set of cantilevers with varying lengths is produced and released, having all the same width and thickness. Then, it is measured the detachment length which is defined as the length of the cantilever not attached to the substrate. With this value, it is calculated the work of adhesion, W_a , given as:

$$W_a = \frac{3}{8} \frac{Eh^2t^3}{l_d^4} \quad (2.47)$$

where l_d is the measured detachment length. With this result for the work of adhesion of the process, it is possible to estimate if a certain structure will suffer stiction, by calculating the adhesion for its dimensions. If the calculated one is higher than the one obtained experimentally, it means that there is a strong probability for the structure to collapse. Typical values for work of adhesion using structures

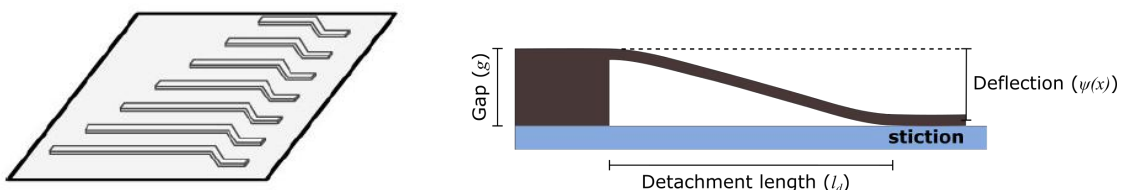


Figure 2.10: *Left*: Typical array of cantilevers used to determine the detachment length [15]. *Right*: Schematics of a cantilever that adhered to the substrate due to stiction [13].

composed by amorphous silicon are $10-100 \text{ mJ}\cdot\text{m}^{-2}$, much higher than van der Waals attraction, W_{vdW} , given in approximation as:

$$W_{vdW} = \frac{A}{12\pi d_0^2} \quad (2.48)$$

where A is the Hamaker constant ($\approx 1.6 \text{ eV}$ for silicon) and d_0 is the separation distance when both surfaces are in contact. By using a separation d_0 of 5 \AA , the attraction due to van der Waals forces equals $17 \text{ mJ}\cdot\text{m}^{-2}$ which is a relatively small value.

Some strategies already being employed to decrease this parameter are surface treatment to improve hydrophobicity and immersion in liquids with low surface tension in order to decrease capillary forces [14, 50]. Electrostatic forces can be decreased by using conductive materials instead of insulators and van der Waals forces are intrinsic to the properties of the used materials (dipole moment and polarizability) so they can only be reduced by roughening treatments on the surfaces [15].

2.2 Microfluidics physics

A full insight into microfluidic systems and their general behaviour is given in *Introduction to microfluidics*, by Patrick Tabeling [51] and a full review on general models and mathematics is covered in *Microfluidics: modeling, mechanics, and mathematics*, by Bastian Rapp [52]. In a microfluidic structure, the surface-area-to-volume ratio is much larger than in a macroscale system. For this reason, the fluids in a microscale system are dominated by interactions with the surface, namely viscous interactions. These are responsible for the different type of flow commonly observed in this regime - laminar flow. In opposition to the turbulent flow, the laminar one is characterized by an organized flow of particles from the fluid that maintain their velocity and relative positions to neighboring particles. The ratio between the inertial and viscous forces is defined as the Reynolds number, Re , which is an indicator of the type of flow observed in a certain system. For a fluid with density ρ and dynamic viscosity μ , flowing at velocity v inside a channel with characteristic length D , the Reynolds number can be defined as:

$$Re = \frac{\rho v D}{\mu} \quad (2.49)$$

The transition between both types of flows is known to be around $Re = 2300$, thus the majority of microfluidic systems present a laminar flow ($Re < 2300$). For a general microchannel with $100 \text{ }\mu\text{m}$ diameter where water is flowing at 1 cm/s , the Reynolds number is 1000.

When a different pressure is applied at one end of the microchannel, the flow is either pushed or pulled and the flow acquires a characteristic parabolic profile. This is the so called Poiseuille flow, depicted in Figure 2.11. Poiseuille stated that when a fluid is flowing inside a long circular channel, the friction between the fluid and the walls of the channel force it to slow down. In fact, what happens is similar to the case of two layers of fluids in contact moving at different velocities. A shear force is created, causing the faster layer of liquid to slow down while the slower one is accelerated. The same happens in the channel, the fluid near the walls is slowed down by friction (drag forces) and a shear force causes

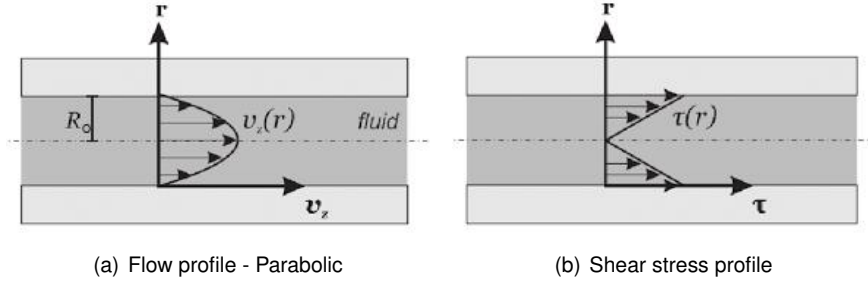


Figure 2.11: Typical flow and shear stress profiles inside a microchannel with a circular cross section. The channel is assumed to have a radius R and the velocity of the flow depends on the radial cylindrical coordinate, $v_z(r)$. The shear stress, $\tau(r)$, also depends on the radial position, being more intense near the walls of the channel. Images adapted from [52].

a deceleration of the fluid portions in the vicinity, locating the points with maximum velocity in the center of the channel. The relation between the applied pressure difference, ΔP , the flow resistance, R_f , and the volumetric flow rate, Q_v , can be derived from the Navier-Stokes equation:

$$\Delta P = R_f Q_v = \frac{8\mu l Q_v}{\pi R_0^4} \quad (2.50)$$

where l and R_0 are the length and radius of the channel, respectively. In this expression, the pressure has a strong dependence on the radius of the channel, meaning that for microfluidics, by decreasing the radius, the pressure increases a lot. Although laminar flow prevents mixing of two different parallel flows, the reduced dimensions of the channels allow a faster diffusion. According to the Stokes-Einstein formalism for diffusion in fluids, the diffusion rate, τ_d , is proportional to the second power of the diffusion length which for the microscale is very small, validating the previous statement. For a general mass diffusivity of $1 \times 10^{-9} \text{ m}^2 \cdot \text{s}^{-1}$, a channel with 1 mm diameter takes 1000 s for mixing, while a $100 \mu\text{m}$ channel takes only 10 s. Furthermore, the parabolic profile enhances dispersion effects inside a carrier fluid. When a different fluid or particles are contained in a carrier fluid exhibiting laminar flow, radial potential gradients of diffusion are formed due to the shear forces, promoting mixing.

Another important concept that should be addressed is the surface tension, ξ . This parameter is generally described as function of the pressure difference between the inside and outside of a fluid's circular surface, ΔP , and its radius, R_0 , or characteristic length, D :

$$\xi = \frac{R_0}{2} \Delta P = \frac{D}{4} \Delta P \quad (2.51)$$

Again due to the increased strength of viscous forces, all the surface interactions become more important to account for. In fact, the above mentioned quantity results from the tendency of a certain fluid to contract its interface surface in order to reduce its free energy. When considering a certain liquid, the surface tension is the balance between the cohesive forces and the adhesive ones. The cohesive forces between the internal molecules of the liquid cause a contraction of its surface, while adhesive forces between the molecules from the liquid and the ones from the external fluid cause an expansion of the same surface. When releasing a certain MEMS, it is beneficial to use a liquid (or gas) with a

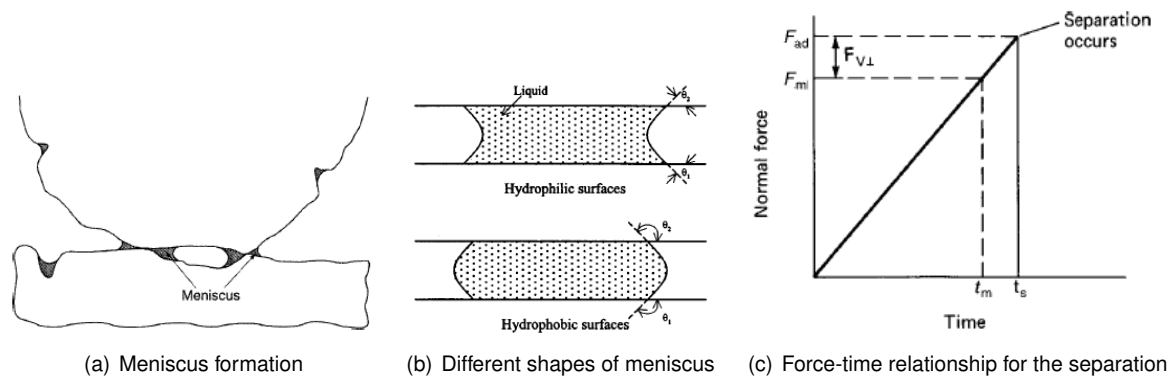


Figure 2.12: When a suspended structure is immersed in a fluid that is evaporating, a meniscus forms underneath it. Its shape depends on the affinity of the material to water, producing different contact angles. The restoring force of the structure needs to surpass the adhesive force which comprises the force created by the meniscus (arising from surface tension), F_m , and the normal component of the viscous force, $F_{v\perp}$. Images adapted from [16].

reduced surface tension since the forces pulling the structure towards the substrate become less strong [16]. As an example, let's consider a meniscus (interface air-liquid) of water under a cantilever beam as in Figure 2.12, knowing that the surface tension of water is $0.0712 \text{ N}\cdot\text{m}^{-1}$ and assuming that the characteristic length of the channel is $100 \mu\text{m}$. The resultant pressure difference is 2.8 kPa which is reasonably high for a suspended microstructure, leading to its collapse towards the substrate as the water evaporates

2.3 Properties of DNA

As widely known, the deoxyribonucleic acid (DNA) is a macromolecule present in the living organisms which carries the genetic information and that can be used as a biomarker for the early detection of certain diseases [53]. It is composed by two coiled strands forming a double helix structure. Each strand is composed by many monomers called nucleotides which consist of a phosphate group, a sugar (deoxyribose) and one of the four nucleobases - cytosine (C), guanine (G), adenine (A) or thymine (T). The nucleobases follow a specific order when pairing by means of hydrogen bonding: A binds with T and C with G. This way it is ensured a large specificity for DNA base-pairing, also called hybridization. Nonetheless, not only totally complementary strands are able to hybridize. If the complementarity is partial, there is some probability that they bind, creating atypical configurations like loops or bulges. The two ends of a strand are not identical, since one of them corresponds to a 3' hydroxyl group, while the other is the 5' phosphate group termination. When pairing strands, they are oriented in opposite directions, so that for the same end of the dsDNA, the terminations are not the same.

Hybridization is a sensitive process that may exhibit different stability when subjected to changes in temperature, monomers ratio, strand length, salt concentration and pH. In fact, if the double stranded DNA (dsDNA) is dehybridized into two complementary sequences of single stranded DNA (ssDNA) by changes in temperature, it is possible to define a melting temperature, T_m . It corresponds to the point at

which the stability of the bonding is compromised and dehybridization starts occurring. Given the strong negative charge of this molecule, a buffer containing a mono- or divalent cation is preferred to increase stability of dsDNA because it is able to shield nearby negatively charged molecules. However, for higher concentration of salt in a divalent cation buffer ($> 1M$), the stability can become compromised since they show some affinity to the nucleobases along the DNA. The presence of solvents in the solution is also adverse for hybridization as well as hydrolysis which can lead to strand cleavage due to damage in phosphate and ribose bonds. For longer strands, hybridization is more difficult to occur, not only because it is necessary to form more bonds, but also because they may bind in incorrect locations which may form loops and mismatches in between. Some general characteristics of dsDNA and ssDNA are listed in Table 2.1 along with their representation in Figure 2.13.

The previous chemical properties of DNA allied with its relatively high stiffness (persistence length) and biological relevance, makes this an extremely suitable molecule for self-assembling monolayers in micro- and nanodevices. With appropriate modifications like thiol group incorporation [30], it is possible to attach these molecules in a specific thin film and perform reactions and measurements with them.

Properties	dsDNA	ssDNA
Rise/base-pair (nm)	0.33	0.6
Helicoidal Diameter (nm)	2.2-2.6	-
Charge/length (e^-/nm)	6	1.66
Persistence length (nm)	50	1.5-3.0

Table 2.1: List of the main properties of dsDNA and ssDNA [53, 54]. The structure considered for the dsDNA is the B-form, which is the most common one. The charge of the strand per unit length is given in terms of the charge of the electron, e^- .

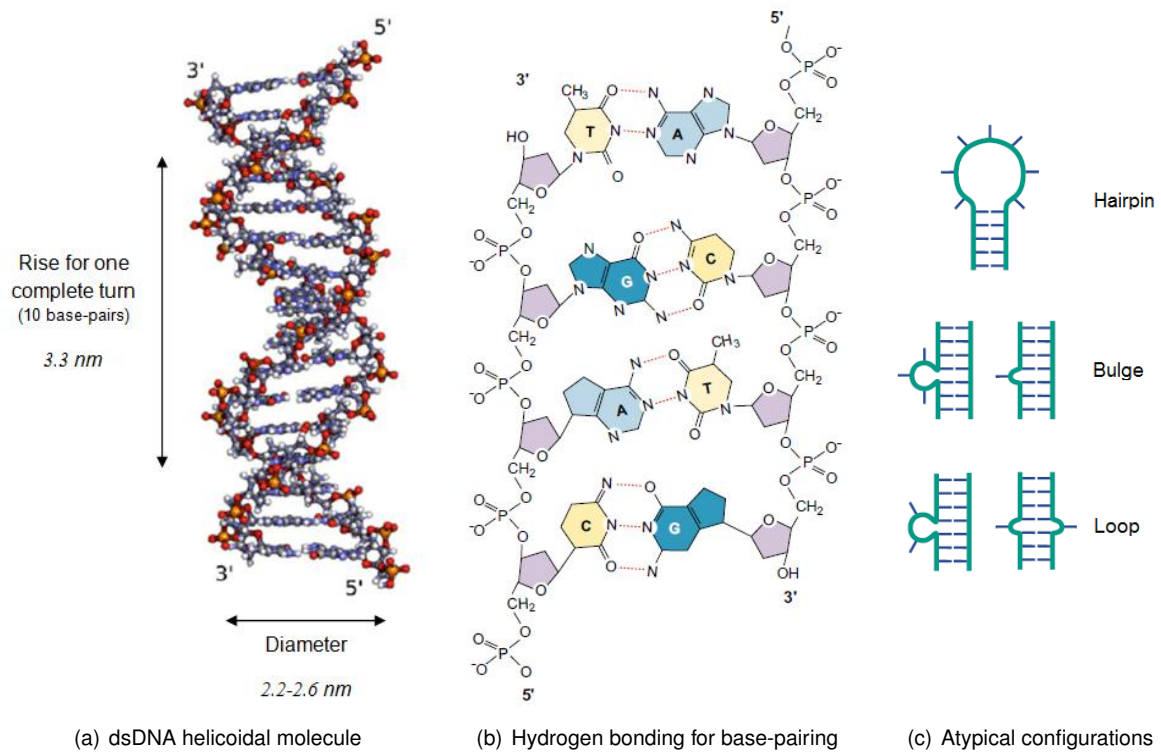


Figure 2.13: In a dsDNA molecule, the different nucleobases are linked by means of hydrogen bonds while the deoxyribose and the phosphate group form covalent bonds. In a ssDNA molecule, only one of the strands is present. During hybridization or even just with a ssDNA molecule, some mismatches may occur and atypical configurations arise: hairpin (ssDNA), bulge or loop. Images adapted from [53, 54].

Chapter 3

Experimental methods and implementation

In this chapter it is covered all the methodology involved in the execution of this project. It starts with a brief description of the biological material and solutions used for functionalization and hybridization as well as the conditions applied. After presenting the structures that are going to be produced, the fabrication process is described and each technique for material deposition, etching and lift-off is detailed in terms of operation principles and conditions. Fabrication of MEMS and microfluidics are covered in separate sections, followed by its integration procedure. For a more detailed and systematic approach on the steps involved in the fabrication of the devices, please refer to the Appendix A where all the runsheets used in the process can be consulted. In the end, the main characterization methods are also described and some considerations about the measurements are referred.

3.1 Functionalization with ssDNA

The process of creating a layer of biomolecules on top of the cantilever which are able to interact with a specific target molecule is called functionalization. Since the device is operating in the static mode, it is important to ensure a strong interaction between the captured molecules. Apart from that, DNA is also capable of producing tuneable SAM's in terms of density, turning it into a promising candidate as probe for surface functionalization. The strategy is to immobilize a ssDNA probe into the cantilever top surface by attaching a thiol group to the molecule. Thiol groups are known to have a strong affinity to gold (Au), so by covering the top surface of the cantilever with this material, it is possible to form a SAM of ssDNA. Then, the complementary strand is introduced in the medium and binds to the immobilized probe, creating a surface stress due to electrostatic interactions with neighboring molecules.

The first biological assays are intended to be performed with both fluorescence and chemiluminescence. For that reason, different labels are used to perform the detection of the oligonucleotides. In Figure 3.1, it is presented a schematic of the different configurations that were implemented for target detection. For fluorescence microscopy it is just necessary to have a fluorophore attached to the

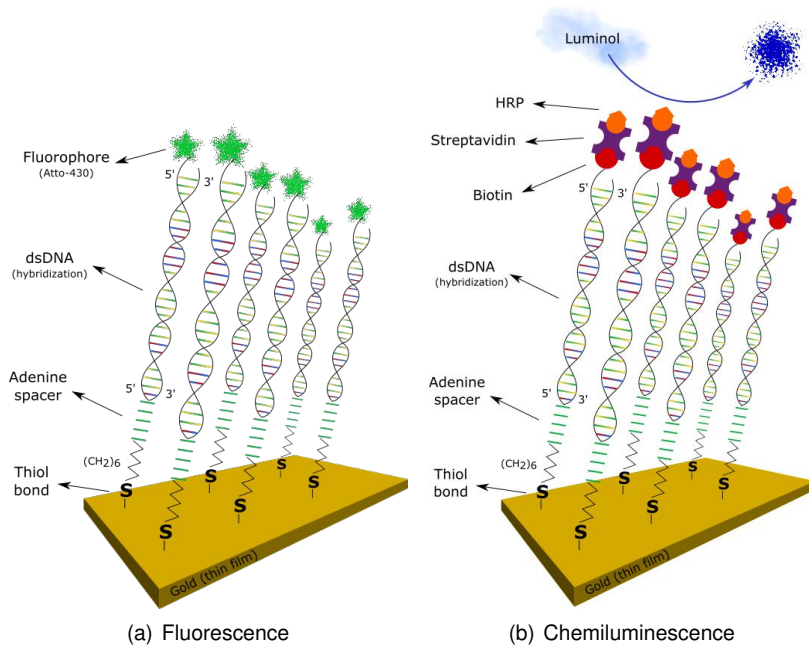


Figure 3.1: Schematics of the two techniques employed for target detection. When the purpose is to detect the probe, a similar configuration is applied, but instead of a dsDNA one has only the ssDNA and the label is attached at the 3' termination.

thiolated ssDNA. Chemiluminescence detection requires in this case a more complex procedure: the thiolated ssDNA is attached to a molecule of Biotin which shows a very strong affinity to Streptavidin (Strept); for the detection itself it is used Horseradish Peroxidase (HRP) which can be conjugated with Strept. If one is interested in tracking the DNA probes, then they must be labelled with the appropriate molecule. Otherwise, they must have their 3' termination free and only the targets are labelled in their 5' termination. If the labelling is performed in the opposite end of the DNA strand, hybridization does not occur.

Fluorescence microscopy

This microscopical technique is defined by the emission of light by a certain substance after being excited with an appropriate light source. As it is known, molecules are composed by different orbitals which are occupied by their electrons. Usually, the electrons tend to occupy the lowest energy level which is called the ground state (S_0). However when excited, the electrons can reach a higher discrete energy level, creating an excited state (S'_n). Each energy level, even the ground state, is composed by various vibrational levels with different energies. When a light source, such as an incandescent lamp or a laser, releases photons with energy $h\nu_{ex}$, they can be absorbed by a group of molecules whose electrons are allowed to reach an excited state if the energy is enough. Fluorescence may occur when the excitation energy is sufficiently high to place the electrons in the first excited level, called excited singlet state (S'_1). If the energy of the light source is so high that the molecule reaches a higher energy level, fluorescence can still occur but only after the molecule loses a certain amount of energy by means of internal conversion, reducing its energy level to the first excited state. Afterwards, the molecule tends

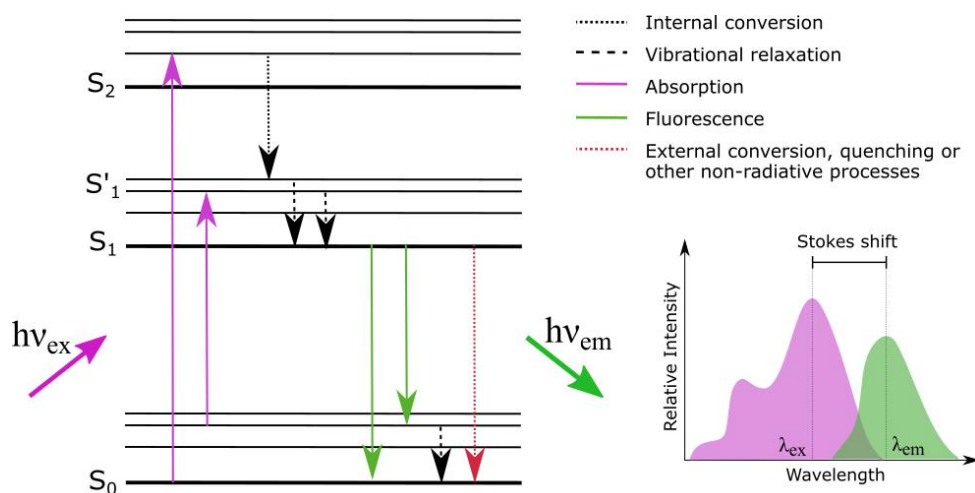


Figure 3.2: Schematized diagram of fluorescence and some intermediate/competing processes upon excitation of a molecule using a light source. In the spectrum of absorbance and fluorescence it is possible to distinguish the Stokes shift.

to return to the initial state by multiple mechanisms. First, it should lose some energy in order to change to the lowest vibrational level of the first excited state (S_1), then another amount of energy is lost so that it is able to return to the ground state. This phenomenon called relaxation can occur by multiple ways. If it undergoes a non-radiative relaxation, the energy that is lost is dissipated as heat to the surroundings. Otherwise, the radiative process called fluorescence takes place and a photon with energy $h\nu_{em}$ is emitted. The wavelength of the emitted photon is in this case longer than the absorbed one since some energy is usually lost in the excited state. The difference in energy $h\nu_{ex} - h\nu_{em}$ is represented in the spectrum of Figure 3.2 and it corresponds to the Stokes shift which is important to quantify in fluorescence microscopy. Some more complex phenomena are able to occur during relaxation, even other radiative and non-radiative processes involving molecules in the vicinities. Because of this parallel mechanisms, the quantum yield of fluorescence is rarely maximum [55].

Two important effects that may occur when working with fluorescence are photobleaching and quenching. The first one is characterized by a photochemical change in the covalent bonds of the fluorophore which no longer is able to fluoresce. This phenomenon can be caused either by an exaggerated intensity (or energy) of the light source or by a long exposure to it. Quenching corresponds to a set of reactions that may occur which are responsible for the decrease of fluorescence intensity. Molecular oxygen and chloride ions are known to induce quenching in some substances and different pressure and temperature conditions can also induce this effect. Usually, these are undesirable effects since they both reduce/eliminate the intensity of the signal.

In microscopy, by knowing the characteristic Stokes shift of a certain molecule and by applying adequate light filters, it is possible to image the excited and emitted photons separately. It is also important to know the excitation energy spectrum in order to select an appropriate light source for the microscope. Commonly, when trying to image biological samples with fluorescence techniques, it is necessary to label the biomolecules with fluorophores chosen accordingly to the affinity to the labelled molecule and to the light filters equipped in the microscope.

For the detection of DNA it was used the same fluorophore as in previous works [56], Atto-430. This fluorophore is characterized by a large Stokes shift with an excitation peak at 433 nm and an emission peak at 545 nm. The microscope (Olympus CHX41) used for imaging is equipped with a 50 W mercury lamp followed by a blue light excitation filter creating an excitation spectrum ranging between 450 – 490 nm. Connected to the microscope, there is a charged-coupled device (CCD) camera (XC30) linked to a computer to acquire the images.

All the molecules labelled with the fluorophore were kept in eppendorfs which were covered with aluminum foil and the experiments were performed with minimum light conditions in the room to prevent photobleaching.

Chemiluminescence microscopy

Similarly to fluorescence, chemiluminescence relies on the emission of visible light upon relaxation from an excited electronic state. The difference here is that the excitation is due to a chemical reaction and not due to light absorption. One of the most popular substrates used in chemiluminescent are the luminol-based ones. For such compounds, an oxidative reaction of luminol (Figure 3.3) occurs when in presence of HRP and peroxide buffer, for example. This reaction creates a product in an excited state that is responsible for the light emission. This microscopical technique is known to be more sensitive than fluorescence. However, its signal tends to decrease as the substrate is consumed [57].

Chemiluminescence was detected by a microscope (Leica DMLM) equipped with a CCD camera (DFC300FX) connected to the computer. In this case, instead of labelling the molecules with fluorophores, Biotin molecules were added to the DNA strands as explained previously.

Molecules and solutions

Having in mind the previous discussed strategies, different oligonucleotides were chosen having the same sequence of 23 nucleobases. These oligonucleotides were synthesized by StabVida Genomics Lab and they are detailed in Table 3.1. They were stored at -20°C in aliquots of $100\ \mu\text{M}$. The chosen DNA sequence is known to be useful for the detection of specific biomarkers of cardiovascular diseases [56].

Milli-Q water ($18\ \text{M}\Omega\cdot\text{cm}$, Millipore) is used in the preparation of TE 1 M NaCl solution (10 mM Tris-HCl, 1 mM EDTA, 1 M NaCl) which is going to be renamed as TE NaCl for the sake of simplicity.

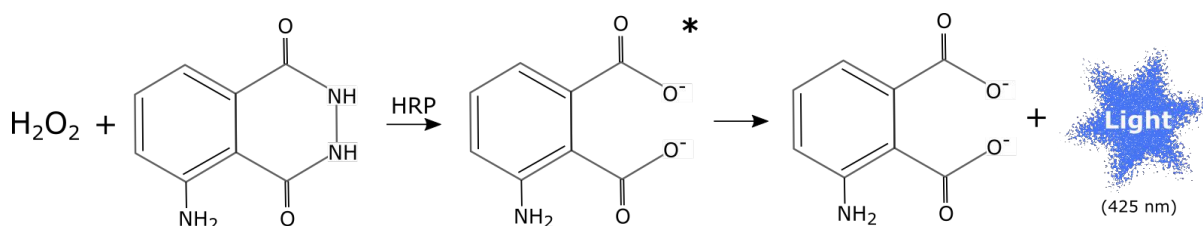


Figure 3.3: Chemical reaction between peroxide and luminol in the presence of HRP for production of chemiluminescent signal. The signal is emitted when the excited product of reaction reaches the ground state.

Phosphate buffered saline (PBS) (Sigma-Aldrich P4417) stock solution of 10 mM with pH 7.4 is prepared by dissolution of one portion (137 mM NaCl, 2.7 mM KCl, 10 mM Na₂HPO₄ and 2 mM KH₂PO₄) in 200 mL of deionized (DI) water at room temperature. Both PBS and TE NaCl are filtered through a 0.2 μm syringe filter from Whatman GmbH and they are subsequently used for preparation of various solutions.

Two types of blocking agents were evaluated during this work: Bovine Serum Albumin (BSA) and Sodium Polyacrylate (PAA). A blocking agent is a molecule responsible for occupying any space of the substrate where the molecule of interest should not be present - passivation. In this case, the blocking agent is supposed to attach everywhere inside the channel except in the gold surfaces where the DNA strands should bind. BSA (A2153, Sigma-Aldrich) is prepared from a stock solution of 1 μg.mL which is diluted to a 4% (w/v) working solution with filtered PBS. PAA (8000 [416029] average molecular weight, Sigma-Aldrich) is diluted from a 45% (w/w) stock solution to a 4% (w/w) working solution, also with filtered PBS.

For chemiluminescent assays, a Strept-HRP conjugate (S-911, Invitrogen) is diluted from a stock solution to a concentration of 1 mg.mL in PBS and kept at -20°C. The luminol-based substrate used for the experiments was Luminol SuperSignal®West Femto Chemiluminescent Substrate kit (34094, Thermo Scientific).

Name	Sequence	5' Mod	3' Mod	Purpose
thiolated ssDNA probe	5'-CAGGTCAAAGGGTCCTTAGGGA-3'	Thiol	-	Probe for capturing the target strand
thiolated ssDNA probe	5'-CAGGTCAAAGGGTCCTTAGGGA-3'	Thiol	Atto 430	Optimization of the immobilization step (fluorescence)
thiolated ssDNA probe	5'-CAGGTCAAAGGGTCCTTAGGGA-3'	Thiol	Biotin	Optimization of the immobilization step (chemiluminescence)
non-thiolated ssDNA probe	5'-CAGGTCAAAGGGTCCTTAGGGA-3'	-	Biotin	Control for thiol bonding
ssDNA compl. target	5'-TCCCTAAGGACCCTTTTGACCTG-3'	Atto 430	-	Target molecule to be captured (fluorescence)
ssDNA compl. target	5'-TCCCTAAGGACCCTTTTGACCTG-3'	Biotin	-	Target molecule to be captured (chemiluminescence)
ssDNA non-compl.target	5'-CGTGTCGTTACATCTGTCCGT-3'	Atto 430	-	Negative control for hybridization (fluorescence)
ssDNA non-compl.target	5'-CGTGTCGTTACATCTGTCCGT-3'	Biotin	-	Negative control for hybridization (chemiluminescence)

Table 3.1: List of oligonucleotides used in this work, including information about modifications and purpose of each molecule.

3.2 MEMS fabrication

Three types of microfabricated structures were designed for the purpose of this thesis. The first one was intended to evaluate and create an efficient protocol for probe immobilization and target hybridization. Another design was created to test and quantify the effects of stiction in the cantilevers. Finally, the last structures included both cantilevers and microchannels with a capacitive readout system.

Structures for biological tests

For these biological tests it is important to have an array of independent microchannels containing patterns composed of all the materials used in the devices for the capacitive measurements (Figure 3.4). This way it is possible to determine and tune the selectivity of thiol groups and DNA itself to different materials. It is indispensable to use already microfluidics for these tests because in a microfluidic regime the interactions between molecules and the environment gain different magnitudes and effects given that shear and viscous forces are considerably higher. Having this in mind, a set of rectangular shapes with dimensions similar to the cantilevers were defined inside the microchannel. Before defining the type of measurements that were going to be applied in the final device, a **first generation** of structures was designed using only patterns of n^+ -type hydrogenated amorphous silicon (a-Si:H) and chromium+ gold bilayer (Cr+Au) on top of the glass substrate. As depicted in Figure 3.5, this set is composed by one a-Si:H rectangle followed by a smaller one of Cr+Au both directly deposited on the glass substrate. After these ones, there are three more a-Si:H rectangles with a Cr+Au layer on top of it with different lengths. The reason to have these other patterns is linked with the fact that the roughness and uniformity of the deposited layer is also affected by the roughness of the material underneath. This variation in roughness can possibly cause some variations in probe immobilization yield and since Cr+Au is deposited on the cantilever's surface, on top of a-Si:H, it seemed worth it to analyze such effect. The differences in length of the Cr+Au layer also help to understand more precisely the relative selectivity between the materials. This sequence of patterns is repeated four times in each channel in order to evaluate the variability along the channel's length.

Afterwards, it was defined that it was going to be implemented a capacitive readout system to the cantilevers, so an additional material needed to be used for the electrical interconnections. In this

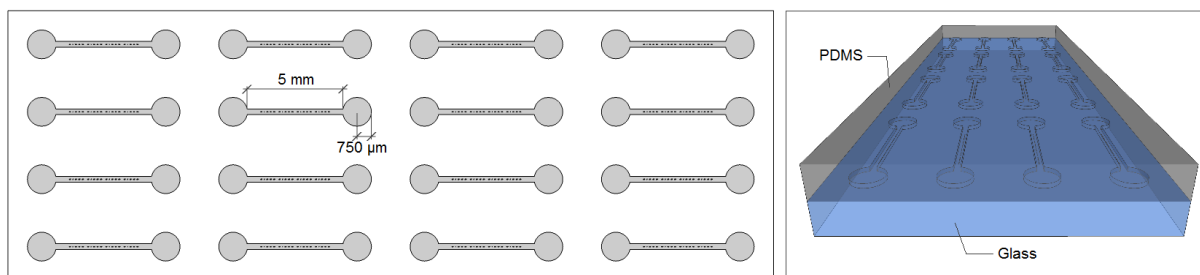


Figure 3.4: *Left*: 2D top view of the microchannel array containing a total of 16 channels per substrate and multiple patterns inside each one; *Right*: 3D view of the microchannel array, showing the glass substrate where the various materials are patterned and the microchannels defined by soft lithography in the PDMS.

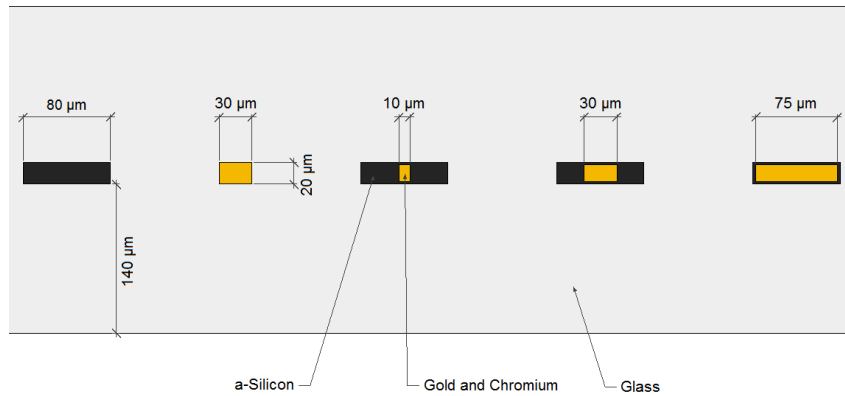


Figure 3.5: Sequence of patterns used in the structures of the first generation of biological tests. The sequence is repeated four times per channel.

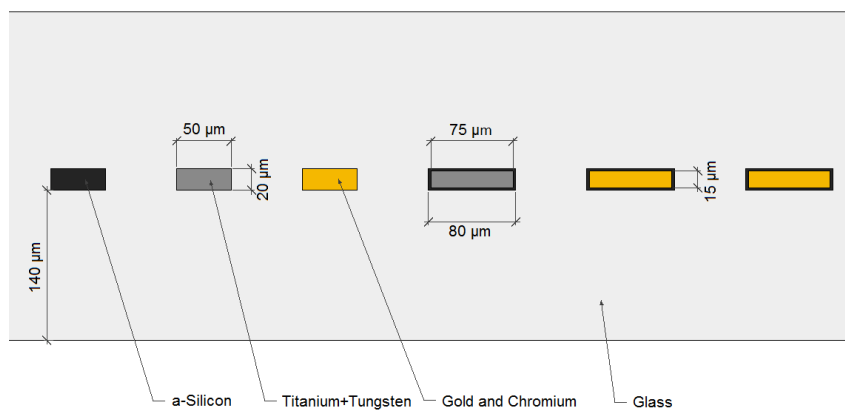


Figure 3.6: Sequence of patterns used in the structures of the second generation of biological tests. This sequence is also repeated four times per channel. Patterns of TiW were added to the previous configuration.

second generation of structures, two patterns of a single-layer of titanium and tungsten (TiW) were added. One of them was directly deposited on glass while the other was positioned on top of a-Si:H. It is extremely important to add this material to the biological tests because the top electrode of the cantilever (which is positioned on the bottom surface of the cantilever) is composed of TiW. If this material shows, for some reason, also a great affinity for thiol groups, then the surface stress originated on gold will match that caused on TiW and they will cancel. In Figure 3.6 it is depicted the sequence of patterns implemented in this generation of structures.

Structures for stiction tests

Since stiction is intrinsically dependent on the dimensions of the cantilevers and the properties of the material, it was created a large set of a-Si:H cantilevers with the same width ($20\ \mu\text{m}$) and thickness ($1\ \mu\text{m}$), but with different lengths and gaps between the glass substrate and the bottom surface of the structure. Each substrate was divided in two dies and each die contained two sets of cantilevers with lengths ranging $[10, 500]\ \mu\text{m}$ in steps of $10\ \mu\text{m}$ (Figure 3.7). Three different substrates were processed simultaneously, each one with a different gap (400, 600 and 800 nm) because it is not so immediate and

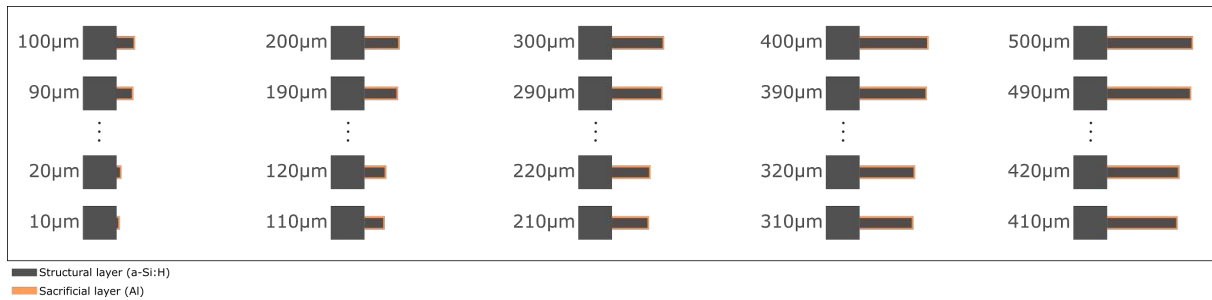


Figure 3.7: Schematics of the structures for the stiction tests. Each cantilever was followed by a caption indicating its length which was allowed to range between 10 and 500 μm .

clever to create gaps with different dimensions in the same sample. This way, it is possible to compare stiction using two different release protocols, confirm the dependence on the geometry and quantify the effect. In this case, it was not integrated with microfluidics.

When stiction occurs, the beam of the cantilever collapses and gets attached to the substrate. This is visible in the microscope by adjusting the focal plane in order to verify if the beam is at a constant height or with the tip located in a deeper focal plane.

Structures for capacitive measurements

For the final integration of MEMS in microfluidics, it was designed a die containing three paired-channels with two inlets and one common outlet. Inside each channel there are four cantilevers with different lengths but the same width and thickness. The layer of Cr+Au was chosen to cover the entire surface of the cantilever, leaving only a tiny empty margin. From each cantilever there are two lines connected to a pair of pads. One comes from the bottom electrode while the other comes from the top electrode of the cantilever. This way, it is prevented any capacitive coupling arising from a common ground line for all the cantilevers. Nevertheless, it was also included a ground plane in order to inhibit any crosstalk between electrical lines. For each sample, a set of short- and open-circuit structures was patterned in order to allow for corrections before the measurements. The open-circuit corresponds to a cantilever without the beam while the short-circuit is designed as a cantilever without sacrificial layer, so that both electrodes can be permanently in contact. These additional features are very important for high precision capacitive measurements, since the parasitic capacitances can exhibit magnitudes similar to the signal of interest. Some details of the structure are shown in Figure 3.8.

The idea here is to overcome any problems related with the typical noise of static mode operation. Since this is an equilibrium state, any slight perturbation or variation in the surroundings can cause a dramatic change in the signal. By having a functionalized set of cantilevers capable of capturing a certain target and another set of the same structures, in a separate channel, with a similar functionalization but where a non-complementary target is present, it is possible to subtract the unspecific signal of the second channel to the signal of the first one and removing almost the entire unspecific signal. Similar strategies using *differential measurements* are referred in [1, 2, 5].

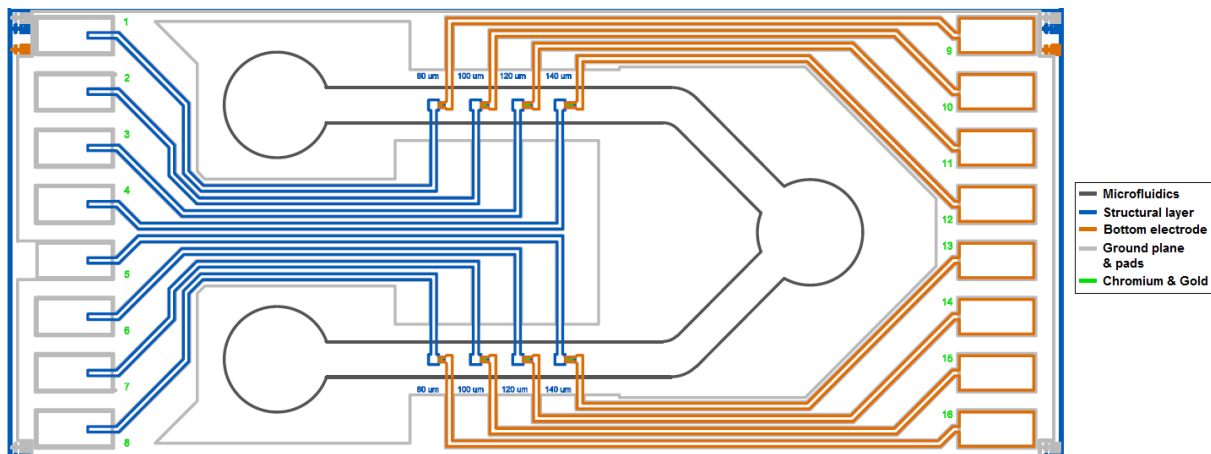


Figure 3.8: Schematics of the top view of the structures used for the capacitive measurements. Each die is composed by three double channels like the one represented in this figure.

Typical MEMS fabrication procedure

As any other device using microfabrication techniques, MEMS are produced in a cleanroom. This is a dedicated room for nano and micromachining with temperature, humidity and light control. It is also equipped with air filtering systems to remove dust and larger microorganisms from the environment. This is an important measure to apply because these particles and organisms have dimensions similar to the produced structures. Also, since there is control over some conditions, the reproducibility of the processes will be increased. INESC-MN is equipped with a large class-100 room and a smaller one where lithography takes place which is a class-10 area. Around these rooms, there is a class-10,000 area, generally called grey area. The classification is related with the quantity of particles of each size that are found inside the room: the lower the class number, the finer is the filtering process.

The MEMS used for this work comprise different layers with different purposes. There is a structural layer which corresponds to the part of the device that is responsible for the mechanical motion. Coupled to this layer, there is the top electrode, right above the bottom electrode which stands on the substrate. These are the electrodes responsible for actuation of the structure and transduction of the mechanical behaviour. In between both electrodes, there is the sacrificial layer which is removed in the end of the fabrication procedure, so that the structure is able to move freely. Finally, another layer of metal is used as ground plane and one made of Au is used for functionalization.

There is a particular sequence for the fabrication steps that must be followed to obtain a device with the proper characteristics (Figure 3.9). The first step involves cleaning the substrate with Alconox for 30 min at 65°C, followed by a similar treatment using instead DI water. Then, it should be rinsed with isopropyl alcohol (IPA) and DI water and dried using a compressed air gun. The substrate is a corning glass (Corning Eagle 1737) with a thickness of 0.7 mm and an area of 5 cm × 2.5 cm. Its high surface quality, low thermal expansion coefficient and low electrical conductivity turn this material into a good choice as substrate. Furthermore, its transparency may be useful for integration with microfluidics.

The following procedure is the DC-magnetron sputtering deposition of a 150 nm thick layer of TiW. This is the metal used as the bottom electrode. Since the patterning is executed via etching, deposition

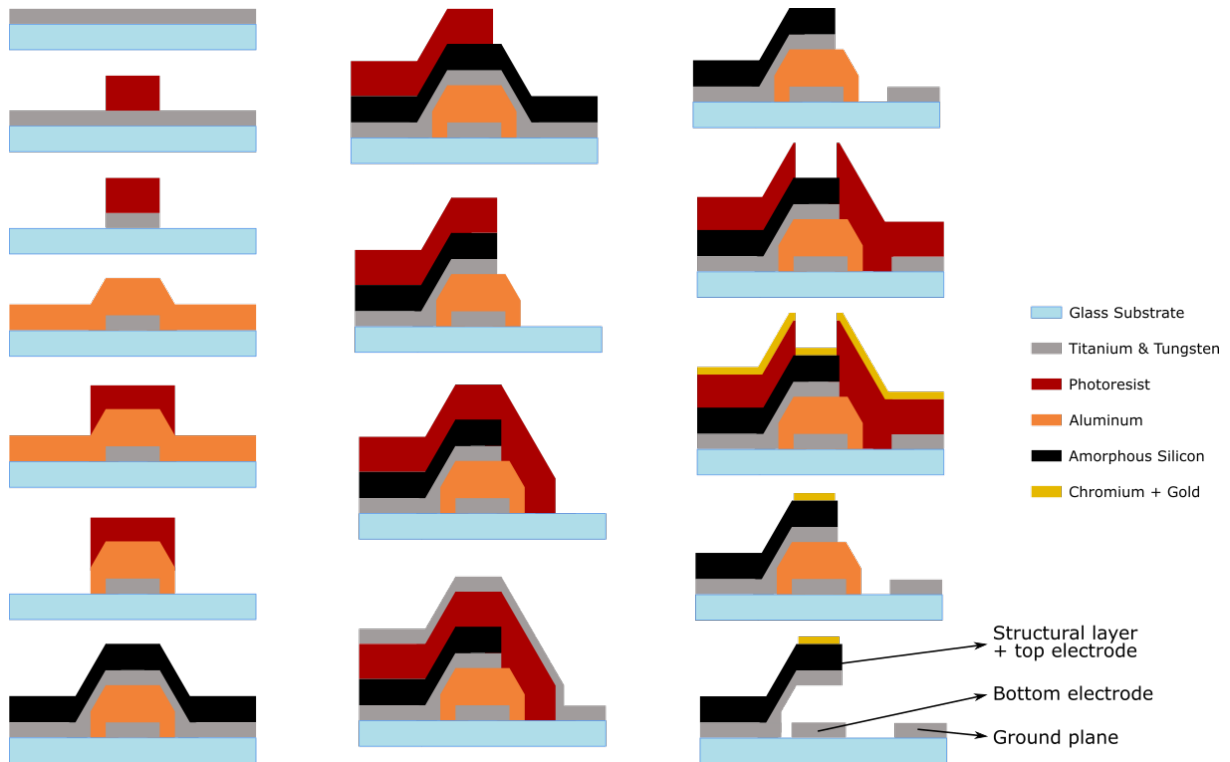


Figure 3.9: Sequence of steps for the fabrication of a cantilever, including the electrodes for actuation, the ground plane and the gold pattern on top. The schematics represent a lateral view of the structure.

must be followed by photolithography in order to define the undesired areas (the areas that have to be etched). All the lithographic steps are performed using a direct write laser (DWL) system and a positive photoresist layer $1.5 \mu\text{m}$ thick. After developing the photoresist (PR), the sample is ready for the reactive ion etching (RIE) that removes all the areas that are not covered by PR. In the end, the PR is dissolved in microstrip (Microstrip 3001, Fujifilm) at room temperature. The sample is rinsed sequentially with DI water, acetone, DI water and IPA and dried under compressed air.

Subsequently, the sacrificial layer of aluminum (Al) is deposited by RF-magnetron sputtering. This material is capable of sustaining the high temperatures present during the structural layer deposition and it can be selectively etched at the end. The thickness of this layer defines the gap between the structure and the substrate that, in this case, was fixed as $1 \mu\text{m}$. The deposition is followed by photolithography just like before, but instead of a dry etch, it is used a wet etch technique to pattern the unprotected regions. For 15 min, the sample is immersed in a commercial Al etchant (Gravure Aluminum Etchant Micropur MOS, Technic) at room temperature and rinsed with DI water afterwards. In the end, a similar procedure with microstrip is performed.

The next step corresponds to the deposition of 150 nm TiW for the top electrode and $1 \mu\text{m}$ of a-Si:H which serves as structural layer. The deposition of the top electrode is similar to the bottom one, while the a-Si:H is deposited using plasma-enhanced chemical vapor deposition (PECVD). Since the patterning of both layers is the same, lithography is only performed after these depositions. After development, they suffer RIE simultaneously, although for a longer duration because the total thickness to be etched is larger. The usual procedure using microstrip and the solvents is also done.

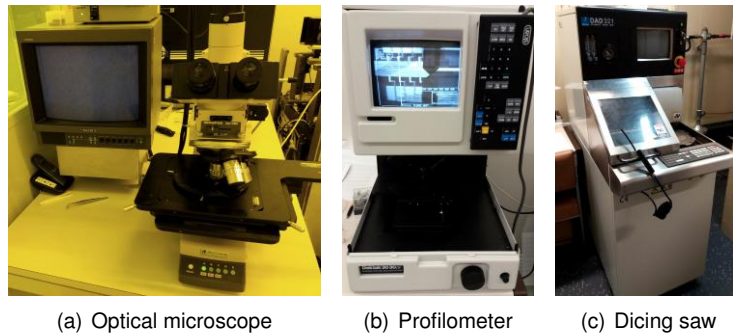


Figure 3.10: (a),(b) Two different equipments that can be used to inspect the deposited and patterned layers of materials; (c) Dicing machine equipped with a diamond saw to separate the samples.

Afterwards, another lithography takes place to define the pads for wirebonding and the ground plane around the electrical vias. In this case, since the technique used for metal patterning is lift-off, the lithographic step needs to be done previously to deposition. The material used is again TiW originating a layer with the same thickness as before. After deposition, the PR and the undesired metallic parts are removed by lift-off using microstrip and then the sample is washed with DI water and IPA.

A layer of Au 50 nm thick is added. Again, because the Au layer is defined via lift-off, first one must do the patterning of the PR using DWL. Only after that, the layer of metal is deposited. To improve adhesion of Au onto a-Si:H, a thin layer (10 nm) of chromium (Cr) is deposited in between. Cr is deposited by DC-magnetron sputtering while for Au it is used RF power instead. After the lift-off, a washing step takes place and the sample is ready for release.

Finally, the wet etch of the sacrificial layer takes place. The Al located in the gap between the bottom and top electrodes is removed and the structure is now free. For the wet etch it is used the same Al etchant as before but now heated at 60°C to accelerate the process. This task takes roughly 45 min, including overetch. However, the sample should be immersed sequentially in DI water, IPA and n-hexane (Sigma-Aldrich). The transition between solutions must be fast to prevent the liquid from drying. The water will wash away the excess of etchant and n-hexane will improve the release of the structures since it creates low surface tension, reducing stiction effects. In the end, the sample dries in air since compressed air might break the released structures.

Immediately after each process, specially after lithography and etching/lift-off, it is important to inspect the sample under the microscope in order to spot any defect or incomplete process. The profilometer installed in the cleanroom (Dektak 3030 ST, Veeco) is also useful to measure the thickness of each layer of deposited material. This analysis should be done after patterning of each layer. If needed, it is also possible to assess the roughness of the deposited layer with this equipment since it uses a surface contact technique with a piezoresistive probe. Both equipments are presented in Figure 3.10, along with the dicing saw (DAD321, DISCO) installed in the grey area. When multiple dies are processed simultaneously in the same substrate, one must separate them in individual pieces using this dicing saw. Before starting, the sample should be spin coated with PR to protect the deposited materials from being damaged during dicing. Each die can then be mounted on a PCB and electrically interconnected by wire bonding.

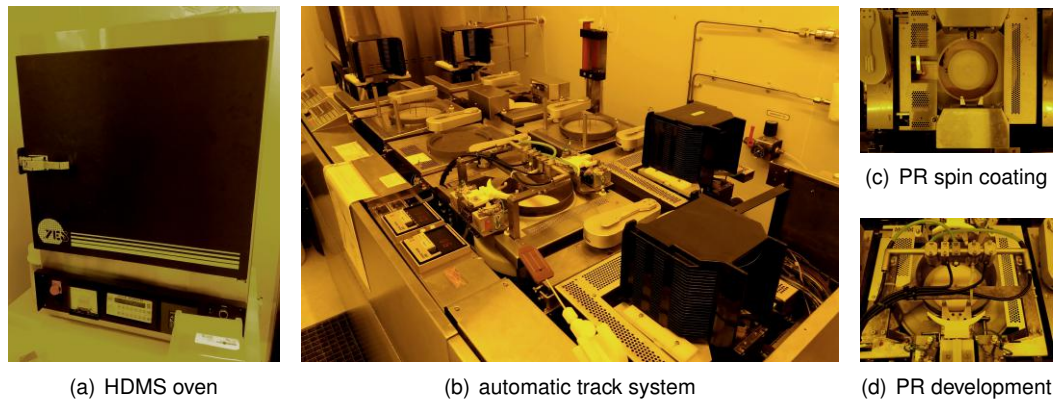


Figure 3.11: Equipment used for PR spin coating and development. (a) HDMS oven used for vapor priming; (b) automatic SVG track system for wafer processing; (c) PR spin coating and (d) PR development modules of the track system.

3.2.1 Photolithography

Microfabrication relies on lithography to perform the patterning of structures with specific shapes with high precision. In such a process, the desired shape is transferred into a polymer which is sensitive to light. This PR may exhibit two different behaviours when exposed to light depending on its type. If it is a positive PR, the light will change the properties of the polymer in the exposed regions and after being developed the PR vanishes from these same regions. This is the type of PR used in the photolithographies for MEMS fabrication (JSR Micro PFR 7790G-27cP). The negative PR shows the opposite behaviour: exposed regions remain intact after development. Because of this sensitivity to light, it is important to have special light conditions in the room. The lamps are covered with a filtering material so that the wavelengths that change the properties of the PR are absorbed by this filter.

Before coating the sample with the polymer and if improved adhesion of the PR is desired, a preliminary process in the vapor priming system is advisable. The equipment (HDMS Prime Oven, Yield Engineering Systems) is composed by an oven which is connected to a vacuum pump and gas inlets. It is possible to completely dry the sample by heating it at 130°C and to remove any particles that may be present on its surface. After this first dehydration step, a compound called hexamethyldisilazane (HDMS) is sprayed inside the chamber for promoting the adhesion of the PR to the surface of the sample. In the end, the remaining HDMS is exhausted and the chamber reaches pressure equalization.

For the PR coating it is used the automatic track system (Silicon Valley Group) showed in Figure 3.11. It starts by pouring the PR on top of the wafer where the sample is mounted while it is spinning. To reach the uniform thickness of $1.5\ \mu\text{m}$, the spinner accelerates until it reaches a specific velocity (2800 rpm) for a short duration (40 s) so that the excess PR is removed by the centrifugal forces. Finally, the polymer is hardened by baking it at 85°C for 60 s.

The exposure of the PR is performed by using a DWL system (DWL 2.0, Lasarray) equipped with a 442 nm Helium-Cadmium laser of 120 mW. In Figure 3.12 it is possible to distinguish the optics responsible for the laser focusing into the sample which is mounted on a mechanical stage. The focusing lens have an air pressure sensor to automatically focus the laser beam. Then it is necessary to align

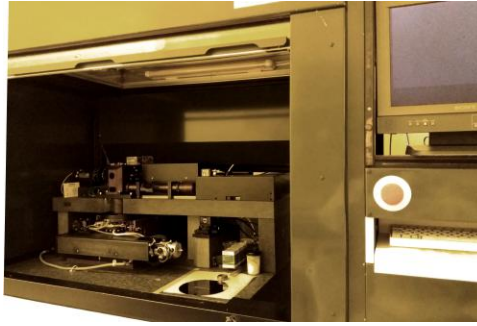


Figure 3.12: Direct Write Laser system for PR exposure. Inside the small chamber it is placed the laser and the corresponding focusing optics as well as the mechanical stage. There is also a CCD camera connected to a screen to assist in the alignment.

the sample appropriately, so that each mask is transferred into the right position. Afterwards, the mechanical stage moves along the horizontal plane and the laser can sweep the entire sample, exposing some regions of the PR as indicated by the files produced by the AutoCAD software. The laser starts exposing one stripe in the y -direction and then moves to the next stripe $200\ \mu\text{m}$ away in the x -direction until it reaches the borders of the die. The minimum feature size achievable by this equipment is $0.8\ \mu\text{m}$ with an alignment precision of $0.25\ \mu\text{m}$.

The last step comprises the development of the exposed PR. For that purpose it is used the second track of SVG, starting with a pre-baking step at 110°C for 60 s and a stand-by for temperature equalization. This pre-baking prevents any incomplete PR reactions from occurring due to the presence of standing light waves inside the PR. The sample is then rinsed with DI water and the developer is poured on top acting for 60 s without spinning. This developer (JSR Micro TMA238 WA) reacts with the PR, breaking its bonds in the exposed regions. Finally, the sample is rinsed with DI water while spinning in order to clean it and remove the undesired PR.

To confirm that the development is complete and to assess the contours of the patterned PR, it is useful to inspect the sample under the microscope with a proper filter to prevent overexposure.

3.2.2 Magnetron sputtering deposition

This is a physical method for deposition of thin films that is based on the principle of momentum transfer between ions of a plasma and a target material. As suggested in Figure 3.13(a) a plasma is created by injecting gas in a vacuum chamber and applying either a certain voltage (DC sputtering) or a RF power using an antenna (RF sputtering). The gas used to create the plasma needs to be an inert gas (Xenon or Argon typically) to prevent any undesired reaction from occurring. The confined plasma is subjected to a negative bias voltage that attracts its ions towards the target material. Under the target, there are also some permanent magnets that confine the trajectories of the ions from the plasma towards the target material, allowing a lower concentration of atoms for plasma ignition and higher deposition rates due to faster removal of the material. This effect is what distinguishes magnetron sputtering from regular sputtering. Since the collisions between the particles can cause overheating of the target and sample, it is also incorporated a water cooling system.

For the deposition of TiW and Al, it is used Nordiko 7000 while Au and Cr are deposited in Alcatel SCM 450 (Figure 3.13). Nordiko 7000 has four different deposition chambers connected to a transfer chamber. In each deposition chamber a different target is placed. Before the transfer chamber, the samples are placed in a loadlock chamber with smaller dimensions in order to accelerate the pumping process. Usually, the pressure at the loadlock is 5×10^{-6} Torr while the deposition chambers achieve 5×10^{-9} Torr. On the contrary, Alcatel has a unique chamber which delays the pumping step to roughly 12 hours so that it can reach the pressure of 10^{-7} Torr. Although the machine only has one chamber, it is equipped with four slots and three shutters to allow multiple processing. In this case, the deposition of Cr is also done by DC sputtering while Au is deposited using RF power. The typical conditions for each deposition are summarized in Table 3.2 and 3.3.

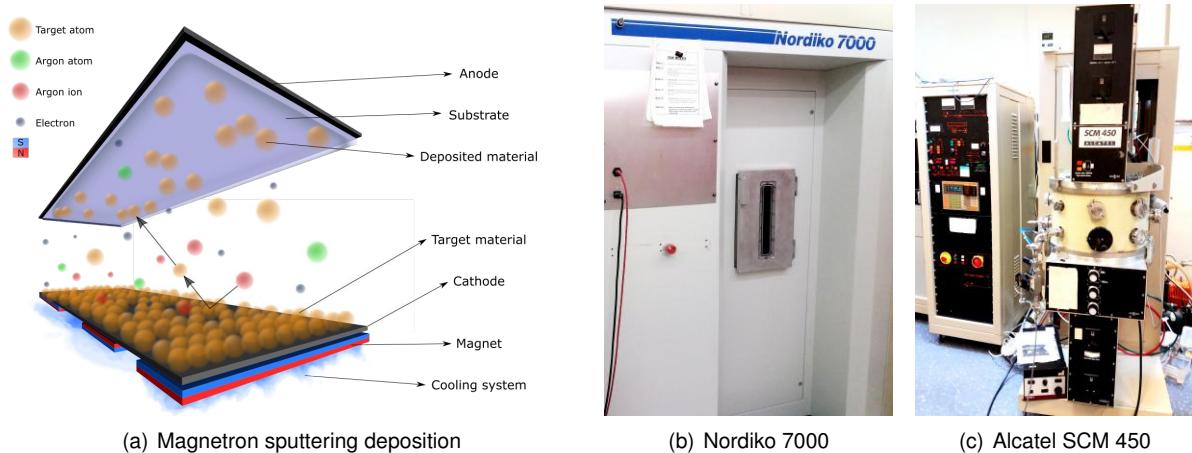


Figure 3.13: Magnetron sputtering is one of the techniques used for thin film deposition. In the figure, it is exemplified the process for DC sputtering. The two machines used for deposition of TiW, Al, Cr and Au are also shown. The control of Nordiko 7000 is performed via computer with the appropriate software while Alcatel is manually set.

Material	DC Power (kW)	Voltage (V)	Current (A)	Ar flow (sccm)	N ₂ flow (sccm)	Deposition pressure (mTorr)
150 nm TiW	0.3	320	0.96	50	1	3.0
1 μ m Al	2.0	400	5.00	50	0	3.0

Table 3.2: Typical conditions and parameters applied for the depositions in Nordiko 7000. For the deposition of TiW it is used the recipe “TiW1500A Low Stress” while for Al it is used the recipe “Al5000A 2kW” twice.

Material	Power (W)	Bias voltage (V)	Ar flow (sccm)	Base pressure ($\times 10^{-7}$ Torr)	Deposition pressure (mTorr)	Duration (min)
10 nm Cr	20 <i>DC</i>	-	20	6.5	2.9	2.5
50 nm Au	20 <i>RF</i>	150	20	6.5	2.9	9

Table 3.3: Typical conditions and parameters applied for the depositions in Alcatel SCM 450. Before each deposition it is performed a cleaning step of the target to be used by turning on the power while keeping the shutter over the sample for 3 to 5 min.

3.2.3 Plasma-enhanced chemical vapor deposition

At INESC-MN it is used a custom-made chamber (Figure 3.14) for this type of deposition. The plasma is created using RF excitation of gas between two electrodes and as in any CVD technique, a set of gases enters the deposition chamber where chemical reactions take place. The product of these reactions is deposited on top of the sample. The plasma serves here as an accelerator of chemical reactions since it will transfer energy to the mixture of reactive gases. Also, for this reason, the sample can be kept at lower temperatures since the formation of reactive and excited species occurs in the gas phase, before reaching the sample. The deposition rate of the process increases due to the plasma-enhancement and the mechanical and structural properties of the deposited layer are more uniform. The gases used for a-Si:H deposition are silane (SiH_4), hydrogen (H_2) and phosphine (PH_3) which need to be kept in a safe area due to their flammability and toxicity. The temperature of the sample is 175°C which is really low when comparing with the typical temperatures used in CVD ($600 - 500^\circ\text{C}$).

The conditions and parameters used for the deposition of a $1 \mu\text{m}$ thick layer of this material are detailed in Table 3.4. The electrical conductivity, mechanical residual stress, microstructure and hydrogen content on the film are intrinsically dependent on these same conditions and they can be adjusted according to the desired purpose.

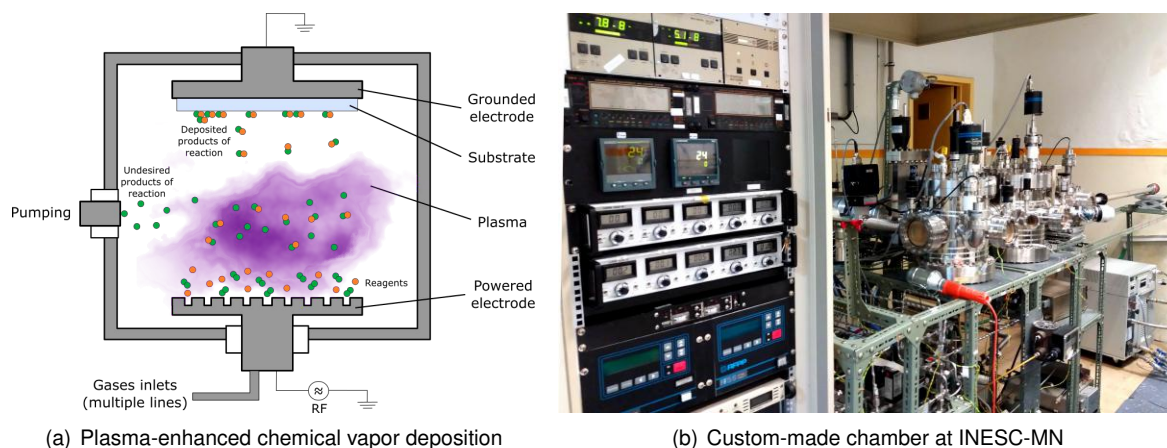


Figure 3.14: For the deposition of a-Si:H it is used the plasma-enhanced chemical vapor deposition depicted in the schematics. The equipment used at INESC-MN is composed by three different chambers, connected to various gas lines and pressure and temperature sensors. The excitation of the plasma is performed by RF power.

Material	RF Power (W)	SiH_4 flow (sccm)	H_2 flow (sccm)	PH_3 flow (sccm)	Deposition pressure (Torr)	Duration (min)
$1 \mu\text{m}$ a-Si:H	15	10	8	5	0.5	46

Table 3.4: Typical conditions and parameters applied for the PECVD. This recipe is optimized to achieve low residual film stress.

3.2.4 Reactive Ion Etching

Similarly to the previous process, a plasma is created using an RF antenna, but in this case, the gases that originate the plasma are turned into accelerated reactive species that hit the sample and react with the deposited material, resulting in its extraction from the surface of the sample. Only the material that is unprotected by the PR is extracted and pumped out of the chamber. However, the PR layer must be sufficiently thick because the PR is also extracted at a lower rate. Given the nature of the principles behind this technique, it is classified as an ion-enhanced chemical etching, adding some advantages of the physical etching to the chemical one. Although being highly selective and fast, any chemical etching tends to be isotropic, creating rounded profiles. In this case, some desired anisotropy is introduced by the acceleration of the ions in the plasma which is a characteristic of a physical process.

Inspection under the optical microscope is always needed since an incomplete etch can cause serious problems during the next steps of fabrication. To verify the thickness of the etched layer, it is possible to use the profilometer also.

This process is executed with LAM Research Rainbow Plasma Etcher (Figure 3.15) using methyl trifluoride (CHF_3) and sulfur hexafluoride (SF_6) for the composition of the plasma. This equipment is composed by two extra chambers with the purpose of accelerating the process of pumping and venting air from them. RIE is used twice in this process: first for the monolayer of TiW and then for the bilayer of TiW + a-Si:H being the etch rate of the first material 0.6 nm/s and the second one 2.5 nm/s. The conditions and parameters used for etching both the bottom electrodes and the structural layer + top electrodes are detailed in Table 3.5. The only difference between both etchings is the duration.

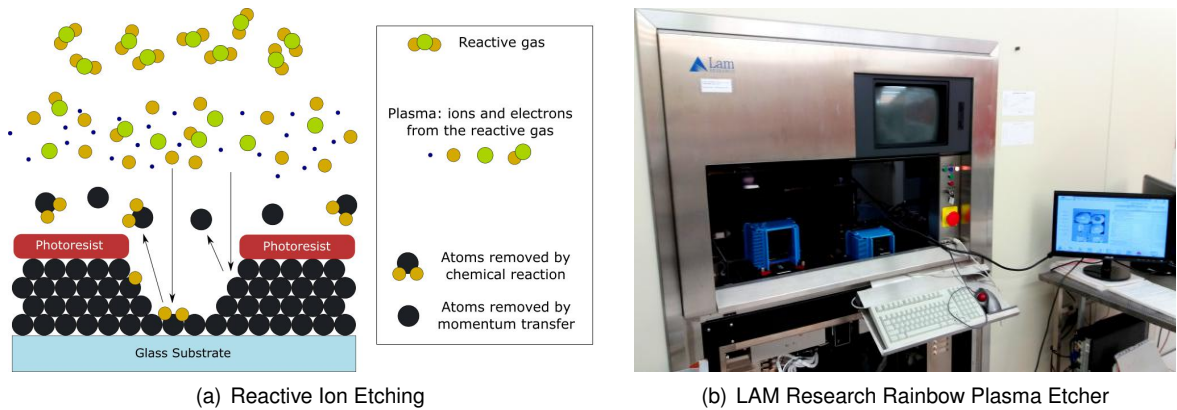


Figure 3.15: Given the physico-chemical nature of reactive ion etching, the etching profile becomes slightly rounded as depicted in the schematics. The equipment used for this process is automatized and optimized for multi-wafer processing.

Materials	RF Power (W)	CHF_3 flow (sccm)	SF_6 flow (sccm)	Temperature ($^{\circ}\text{C}$)	Deposition pressure (mTorr)
TiW & a-Si:H	200	50	50	40	100

Table 3.5: Typical conditions and parameters applied for the RIE of TiW and a-Si:H using LAM Plasma Etcher. Note that when etching solely 150 nm of TiW, the duration of the process is roughly 250 min, while for the bilayer it is necessary a process of 650 min.

3.2.5 Wet etching

This technique relies on chemical solutions to interact with a specific material and to remove it from the sample. Given that it is a pure chemical etching technique, it is usually fast (high etch rate) but completely isotropic which creates some difficulties when trying to define features at the nanoscale (Figure 3.16). The two major advantages when comparing with dry etching are the low costs involved, since there is no vacuum system in this case, and the high selectivity. For MEMS it is very important to have a perfectly selective process so that in the end, only the sacrificial layer is removed. The etch rate of the Al layer using the Technic etchant was determined as 80 nm/min at ambient temperature with manual agitation.

Again, if the material behind the etched layer is transparent, the etch final point can be visually accessed, although it is always a good practice to verify it in the microscope (Figure 3.17). The profilometer should also be used, previously, to determine the thickness of the material deposited in order to know how much material should be removed.

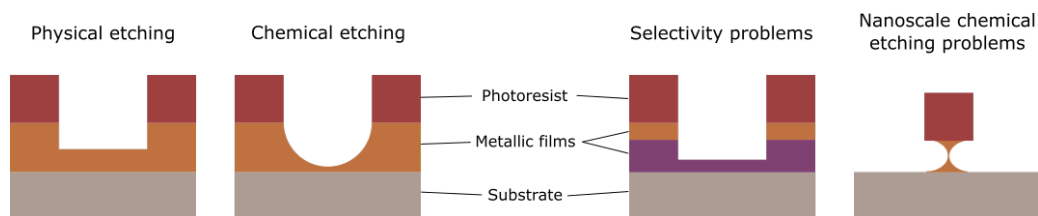


Figure 3.16: Schematics of the different profiles that are obtained when using physical or chemical etching techniques. When processing a multilayered film, physical etching may damage other material layers due to poor selectivity of the process when comparing with chemical etching. At nanoscale, the thickness of the film may create some additional difficulties to the process.

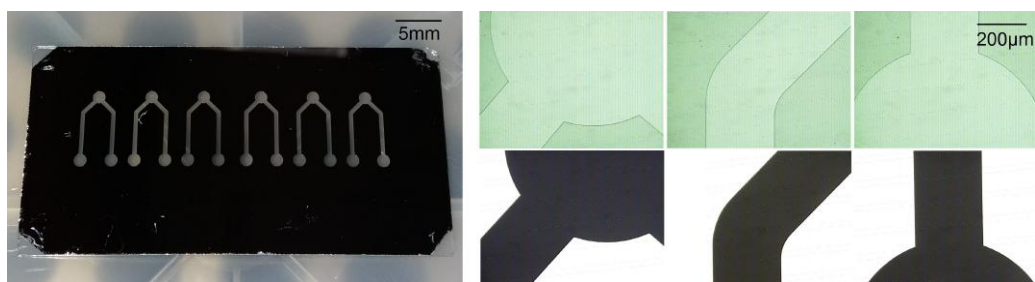


Figure 3.17: *Left*: By visual inspection it seems that the wet etch of the hard mask of the microchannels is completed. *Right*: Images from the optical microscope showing the structures defined in the hard mask by wet etch. The images in green tones are taken after lithographic exposure, while the ones in black and white are taken after etching.

3.2.6 Lift-off

Similarly to etching, lift-off is a patterning technique that takes place after the patterning of the PR. When immersed in microstrip, the patterned PR is dissolved and the layer of material that was deposited on top of the polymer is also removed since it does not have any support (Figure 3.18). On the contrary, in the regions where the PR was removed after development, the material is deposited directly on the

sample's surface, so it remains intact. This type of technique usually creates an irregular contour when comparing with etching techniques. For this reason, it is chosen when an etching process would affect deeper layers. Some other problems may occur specially when trying to lift-off thicker layers of material. For example, when the PR is not completely dissolved or when the material adheres and hardens so that it remains in its position, some undesired interconnections between different patterns may arise. "Rabbit ears" is a common defect that appears in the sidewalls of the PR after deposition of the material to be lifted-off. It is characterized by a pronounced elevation in the border of the patterned PR and it can cause unwanted connections with other layers. For that reason, it is commonly used only for the patterning of the top layers.

During the fabrication of the device under study, lift-off was only applied in the two last layers of materials since an etching process would possibly remove some of the materials in the structural layer. To accelerate the process, the structures firstly processed were placed in the ultrasonics bath at 65°C for a few minutes, but in the end some patterns of the structural layer were damaged possibly due to weak adhesion. Given the high thermal expansion coefficient of gold, it turned out that a simple heated bath with periodical manual agitation is enough to perform its lift-off. However, the lift-off of TiW was not completed when left in the heated bath overnight (Figure 3.19). For this reason, instead of placing it in a continuous heated ultrasonics bath, the sample was intermittently subjected to the ultrasonics for periods of 5 s at the same temperature.

In this process, it is also indispensable an optical inspection with the microscope since really small portions of material may remain intact after a certain period of time due to incomplete lift-off.



Figure 3.18: *Left*: In the beginning, only a uniform layer of metal over the sample is visible. *Middle*: After some moments, some of the PR starts dissolving and the metal that was deposit on top of it also starts peeling off. *Right*: Finally, all the PR is dissolved and the metal layer is patterned.

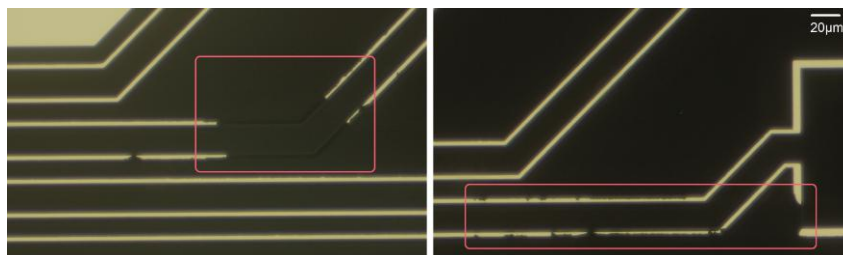


Figure 3.19: Images from the optical microscope, showing an incomplete lift-off (red marks). This result was obtained when it was not used ultrasonics bath during the process.

3.3 Microfluidics fabrication

In parallel, a set of microchannels needs to be produced in order to integrate with the MEMS. Microfluidics were fabricated using polydimethylsiloxane (PDMS) which is a very advantageous soft polymer when used for this purpose. This material is an electrical and thermal insulator that is permeable to gases but not to water. It is transparent for a wide range of wavelengths (300 to 2200 nm) which allows microscopical techniques to be used, like fluorescence and chemiluminescence. Its high elasticity allows a good water tightness of connections and the fabrication of valves and pumps for fluid handling. Furthermore, it is a non-toxic material which means that the resultant devices are easily disposable.

Generally, to build a microfluidic device it is used a slightly different technique for patterning which is called *soft lithography*. This is characterized by replicating a certain structure present in a mold onto an elastomeric material. Nevertheless, the molds used for this purpose are usually produced via photolithography. The complete procedure schematized in Figure 3.20 is composed by four different steps: hard mask fabrication, mold patterning, PDMS microstructures fabrication and sealing.

To produce the desired structures in the mold, it is used a *hard mask* for exposure during lithography. The substrate used for the mask is again the corning glass with the same dimensions and subjected to the same washing procedure previously detailed. First, it must be deposited an Al layer with 100 nm thickness on the substrate, using again Nordiko 7000 (DC-magnetron sputtering). After its deposition, the sample is spin coated with PR which is patterned by DWL photolithography. The unprotected regions are removed by wet etch (3 min duration) and then, the sample is immersed in microstrip to dissolve the PR. Finally, it is rinsed with DI water, IPA and DI water again and dried under compressed air. For further details on this procedure, please refer to Table 3.6 and to the previous subchapter.

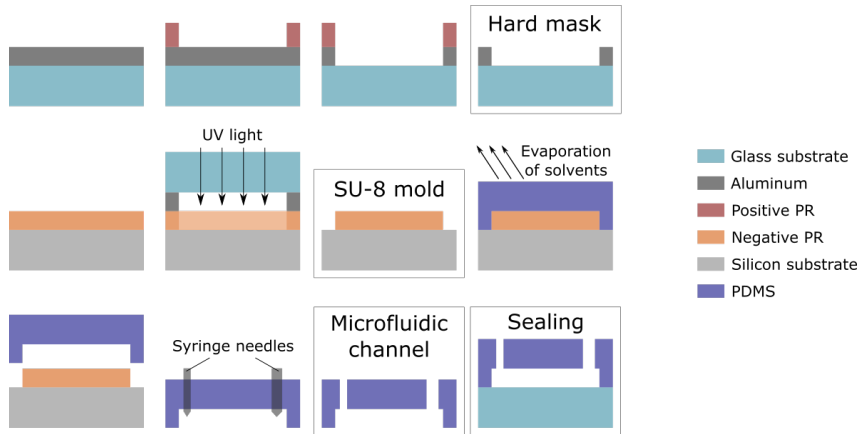


Figure 3.20: Schematics of the process for microfluidic channels fabrication.

Material	DC Power (kW)	Voltage (V)	Current (A)	Ar flow (sccm)	N ₂ flow (sccm)	Deposition pressure (mTorr)
100 nm Al	2	392	5.12	50	0	1.5

Table 3.6: Typical conditions and parameters applied for the deposition of Al in Nordiko 7000 in order to fabricate the hard mask.

Thickness (μm)	Function #	Velocity (rpm)	Duration (s)	Acceleration (rpm/s)
20	1	500	10	100
	2	1700	34	300
50	1	500	10	100
	2	2300	37	300

Table 3.7: Parameters for the spin coating of SU-8 on top of the silicon substrate.

Afterwards, the *mold of SU-8* is patterned by making use of the hard mask. This material is a negative PR that is not dissolved by the developer when exposed to UV light. For this reason, the hard mask should be transparent inside the contours of the channels, this way, they can remain intact after development. The procedure starts by sequentially washing a piece of a silicon wafer with acetone, DI water, Alconox, DI water, IPA and DI water again, similarly to the washing protocol of the glass substrates. Then, a portion of PR (SU-8 2015, MicroChem) is poured on top of the previously cleaned silicon substrate. The uniform layer of PR is obtained by spinning the sample in an automatic spinner (WS-650MZ-23NPP/LITE, Laurell) using again the centrifugal forces as agents and the parameters listed in Table 3.7. The height of the microchannels is defined by the thickness of this PR layer which should correspond to 20 μm . In fact, for the structures integrated with the MEMS, the thickness was increased up to 50 μm in order to prevent any damage since the cantilevers showed some strong residual stress. For this purpose, a different PR with an increased viscosity was used (SU-8 50, MicroChem) so that a higher thickness is achieved. Nevertheless, in order to harden the PR and remove any air particles from it, the substrate is heated in a hotplate (Digital Hotplate SD160, Stuart) and afterwards, it is placed below the hard mask in direct contact so that it can be exposed to an UV source. The exposure chamber is equipped with an holder for the sample and a shutter that must be removed when exposure starts. The light source has a wavelength of 254 nm and the sample is exposed to it for a few seconds. Similarly to what is performed in the SVG track, the sample is heated (post-exposure baking) and after cooling down, it is immersed in propylene glycol monomethyl ether acetate (PGMEA, Sigma-Aldrich) - the developer - for a few minutes under mild agitation, but in this case the tasks are performed manually inside the laminar flow hood. Finally, when the development is completed, the sample is rinsed carefully with IPA and it is heated again in the hotplate. The details for this procedure are listed in Table 3.8 and 3.9.

Finally, the *PDMS microstructures* are fabricated via soft lithography. PDMS is formed by a mixture of a viscous base component and a curing agent (Sylgard 184 silicone elastomer kit, Dow Corning) that creates the polymer when the solvents are evaporated. The proportions between both compounds determine the rigidity of the polymeric structure, meaning that more curing agent will decrease the rigidity of the resultant polymer. In this case, a proportion 1:10 (w/w) of curing agent is added to the PDMS base and it is mixed by hand. In order to remove the air bubbles that become trapped during the mixing step, this mixture is degassed in a low vacuum chamber for roughly 25 min. Then, the SU-8 mold is placed inside a Petri dish and the PDMS mixture is poured on top of it (Figure 3.21). After 2 hours inside the oven (Memmert) at 70°C, the PDMS is cured and ready to be cut and peeled off from the mould. One

advantage of this procedure is that the hard mask and mould can be used multiple times until one of them gets damaged.

All the equipment necessary for the processes described above is shown in Figure 3.22.

Procedure	Duration	Temperature	Equipment
Soft bake	4 min	95°C	Hotplate
Cool down	2 min	≈ 25°C	-
Exposure	27 s	-	UV chamber
Post-exposure bake	5 min	95°C	Hotplate
Cool down	2 min	≈ 25°C	-
Development	2 min	-	Container
Hard bake	15 min	150°C	Hotplate

Table 3.8: Conditions and materials used during the process of SU-8 2015 lithography (20 μm thickness), immediately after spin coating.

Procedure	Duration	Temperature	Equipment
Soft bake	10 min	95°C	Hotplate
Cool down	2 min	≈ 25°C	-
Exposure	25 s	-	UV chamber
Post-exposure bake	8 min	95°C	Hotplate
Cool down	2 min	≈ 25°C	-
Development	6 min	-	Container
Hard bake	15 min	150°C	Hotplate

Table 3.9: Conditions and materials used during the process of SU-8 50 lithography (50 μm thickness), immediately after spin coating.

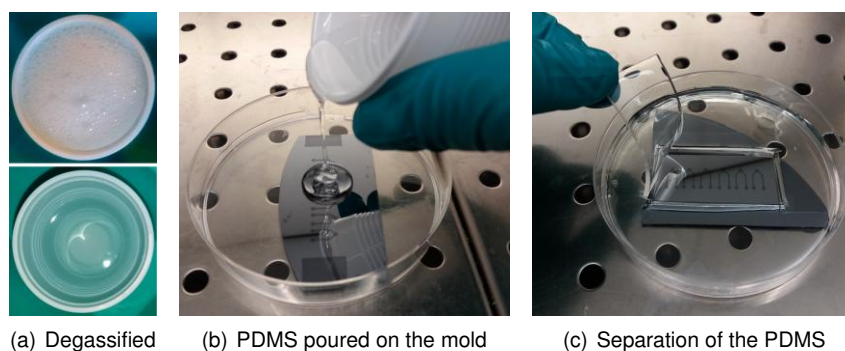


Figure 3.21: (a) PDMS after mixing with the curing agent with a lot of air bubbles inside it and after degassification in the vacuum chamber; (b) Degassed PDMS is poured into a petri dish with the SU-8 mold inside it; (c) The PDMS can easily be peeled off from the mold which can be reused if not damaged.



Figure 3.22: Equipment used for microfluidics fabrication.

3.3.1 Interface and control of microfluidics

Before sealing the PDMS microchannels against any substrate, it is necessary to perforate the inlets and outlets. For that purpose, syringe needles with appropriate diameters are used to define these points. The dimensions of the needles are chosen accordingly to the interface adapter that is going to be used. Commonly, when using *pulling* techniques, the liquid that is intended to flow inside the channel is captured by a micropipette and its tip is placed in the inlet. A metallic adapter connected to a syringe pump via a plastic tube is located in the outlet and the difference in pressure induced by the pump is the responsible for pulling the liquid across the channel. The opposite effect is expected when using *pushing* instead. The syringe pump allows a controlled flow inside the channel through the utilization of a step motor. A wide range of flow rates are possible to achieve starting from dozens of $\mu\text{L}/\text{min}$ down to $0.01 \mu\text{L}/\text{min}$.

In this work, it was used the pulling technique with a double syringe pump (Microsyringe Pump 4000, New Era Pump Systems) that is able to work in both modes (Figure 3.23). According to [56] this technique reduces the problems with air bubbles inside the microchannels that are difficult to remove and cause some problems in biological assays. The syringes (1 mL insulin luer U-100, Codan) are connected to a luer stub adapter (LS20, Instech) which is then attached to a plastic tubing (BTPE-50, Instech). The tubing is then connected to the microchannel outlet by a 90° metallic plug (SC20/15, Instech). The solutions that are intended to flow inside the channel are dispensed in the inlet by micropipette tips (Eppendorf). Both metallic plugs and micropipette tips must remain at a minimum distance from the substrate, otherwise they may clog the channel and no differential pressure is applied to it.

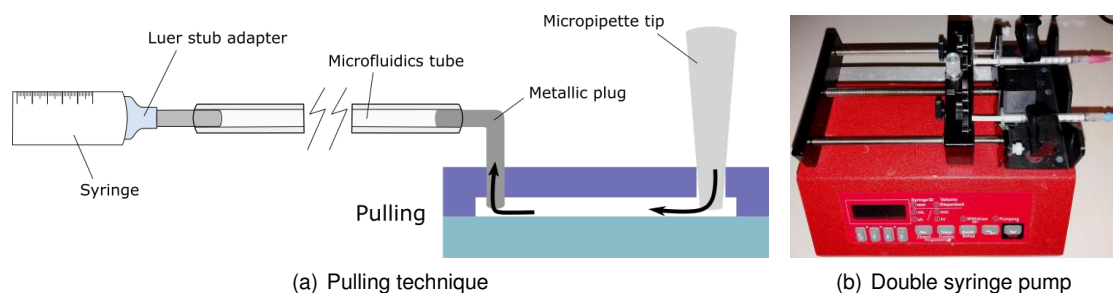


Figure 3.23: Schematics of the control setup for microfluidics control. The plastic tube where the metallic plug is inserted must be connected to the syringe needle placed in the pumping system.

3.3.2 Integration of microfluidics into MEMS

Different techniques were tested in order to find the best solution for sealing the PDMS structure against the glass substrate after processing (Figure 3.24). The first one involved placing both components inside a Plasma Cleaner Chamber (PDC-002-CE, Harrick Plasma) for a few minutes at maximum power. Although originally this method was intended for surface cleaning by remotion of organic contaminants, it is also very useful to induce the bonding between glass and PDMS. The process chamber is equipped with a three-way valve that establishes the connection with a mechanical pump, an oxygen bottle and the room (for venting). The process only starts after reaching approximately 0.3 mTorr with the valve open for the oxygen bottle. Then, an RF antenna turns the gaseous oxygen into plasma which is responsible for the oxidation of PDMS and glass surfaces. When both surfaces are brought into contact, Si-O-Si bonds are formed, creating a strong sealing. To ensure a lasting sealing, the final structure is placed in the oven at 70°C for 20 minutes.

In fact, when the surfaces to be sealed only involve glass and PDMS bonding, this technique works very well. However, for the structures with the ground plane (capacitive measurements) this method is not enough since the metal that is present in a lot of regions does not allow the Si-O-Si bonds to form. Following this reasoning, another method was used for these structures: stamping with “fresh” PDMS. In this case, an additional glass substrate is spin coated with a thin layer of PDMS, using the conditions detailed in Table 3.10. Afterwards, this layer is heated in a hotplate at 70°C for 6 min so that the PDMS is hardened by inducing its cure. The PDMS structure where the microchannels are patterned is brought into contact with the spin coated PDMS for a few seconds, just to transfer some of the semi-cured PDMS into the surface of the microchannels structure. Finally, this piece is placed on top of the chip with the MEMS and the set is moved to the oven for 2h to complete the curing process. Here, the microfluidic structure is stamped on the spin coated PDMS which acts like a glue. This sealing is a reversible one, meaning that it is more fragile, but still allowing the sealing when metal layers are present.

The alignment setup (Figure 3.25) is composed by a stereo microscope, a two-axis micromanipulator for the glass substrate and a vacuum gripper mounted in a three-axis micromanipulator to move the microfluidics structure above the glass chip. After preparing the sealing process, the samples should be immediately aligned and pressed one against the other, otherwise the sealing may be compromised.

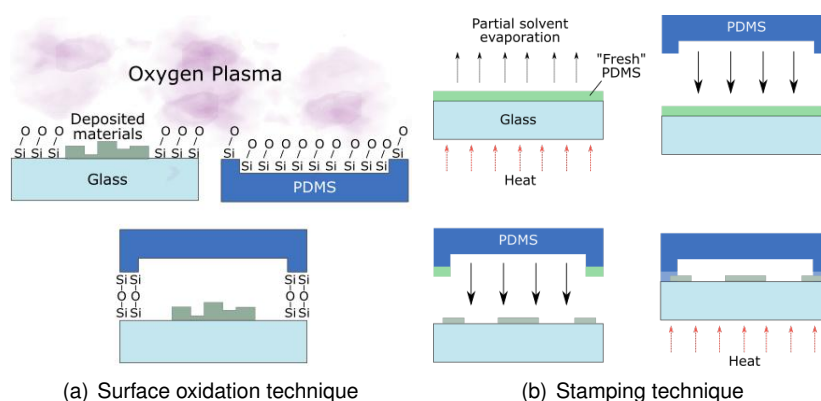


Figure 3.24: Two different techniques for PDMS microfluidics sealing against a substrate.

Function #	Velocity (rpm)	Duration (s)	Acceleration (rpm/s)
1	500	5	500
2	8000	20	1000

Table 3.10: Parameters for the spin coating of PDMS on top of a glass substrate.

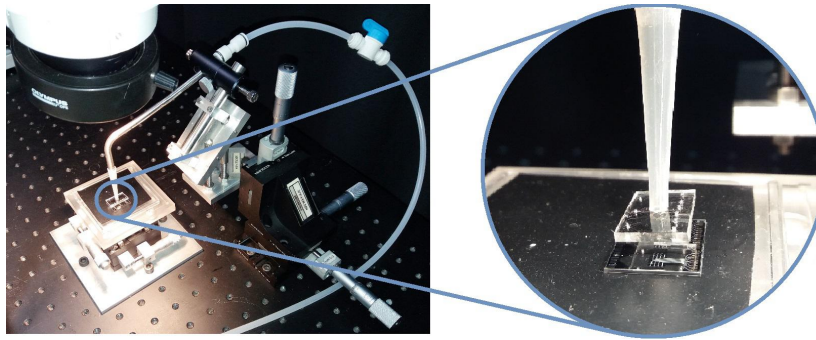


Figure 3.25: Equipment used for the alignment of the microfluidics structure and the MEMS chip during the sealing procedure.

3.4 Characterization and measurement setup

Analysis of the biological assays

Along the optimization of the assay, various protocols were investigated by varying solutions, flow rates, blocking agents, incubation duration among other parameters. For that reason, only the optimized protocol is described in this section (Protocol 3.1). This is the protocol used afterwards for the MEMS capacitive measurements. It starts with two washing steps at $20 \mu\text{L}/\text{min}$ in order to remove any contaminants or particles that may be populating the microchannel and the films inside it. Then, BSA-4% is flowed at $0.75 \mu\text{L}/\text{min}$ for 15 min for passivation of the microchannel walls and other surfaces, except for Au. Afterwards, the probe ssDNA enters the microfluidic structure at the same flow rate and for the same duration but it is incubated at room temperature for 24 hours when the flow stops. The complementary or non-complementary target is then allowed to bind to the probe by flowing it in the same conditions but without an incubation step. Subsequently, Strept-HRP is flowed at $1 \mu\text{L}/\text{min}$ for 10 min so that the targets can be labelled. Finally, the luminol is mixed with the peroxide buffer in a 1 : 1 ratio and flowed at $20 \mu\text{L}/\text{min}$ for no longer than 3 min. Each step is intercalated by a washing step with TE NaCl at $5 \mu\text{L}/\text{min}$ for 1 min to remove the excess molecules that did not bind. Both probe and target DNA are mixed with TE NaCl so that it reaches a concentration of $5 \mu\text{M}$.

The protocol for fluorescence measurements is not described because this method revealed to be problematic in the presence of Au films and it was no further used.

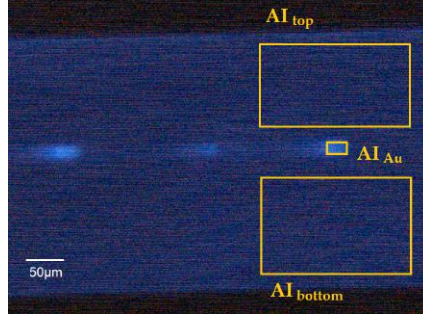


Figure 3.26: Example of a measurement of the signal on a gold surface. The average RGB intensity is measured for the area corresponding to each square.

{	Wash w/ IPA	20 $\mu\text{L}/\text{min}$ - 3min	
	Wash w/ TE NaCl	20 $\mu\text{L}/\text{min}$ - 3min	
	BSA-4%	0.75 $\mu\text{L}/\text{min}$ - 15min	
	Wash w/ TE NaCl	5 $\mu\text{L}/\text{min}$ - 1min	
	Thiolated Probe (5 μM)	0.75 $\mu\text{L}/\text{min}$ - 15min + 24 h incubation	
	Wash w/ TE NaCl	5 $\mu\text{L}/\text{min}$ - 1min	(3.1)
	Target-biotin (5 μM)	0.75 $\mu\text{L}/\text{min}$ - 15min	
	Wash w/ TE NaCl	5 $\mu\text{L}/\text{min}$ - 1min	
	Labelling Strept-HRP	1 $\mu\text{L}/\text{min}$ - 10min	
	Wash w/ PBS	5 $\mu\text{L}/\text{min}$ - 1min	
	Luminol	20 $\mu\text{L}/\text{min}$ - 3min	

The results corresponding to the images obtained by chemiluminescence and fluorescence were extracted using the software *ImageJ*. Without altering the properties and extension of the image, the signals were extracted using the rectangle tool of the software that allows one to select a rectangular region of the image and to measure its average RGB intensity, AI_X , in arbitrary units. For example, to measure the signal on top of Au surface, S_{Au} , it should be measured the region correspondent to this surface and two other regions in the vicinity inside the channel, $AI_{top/bottom}$, as showed in Figure 3.26. Then the total signal for the case of the Au surface is calculated as:

$$S_{Au} = AI_{Au} - \frac{AI_{top} + AI_{bottom}}{2} \quad (3.2)$$

This way, it is guaranteed that the calculated signal is not affected by the background. After having calculated the signal from one pattern, and since there are four repetitions of the same sequence of patterns in every microchannel for the biological tests, the signals of the other repeated patterns are calculated and averaged with this one. The experimental uncertainty in each assay corresponds to the standard deviation of the four values. When it is possible to repeat three times the same assay in different channels, the uncertainty is the standard deviation of averaged results from each channel.

Optical setup for resonance measurements

Before proceeding towards the measurement of cantilevers bending upon molecular recognition, it was measured the resonance frequency of each different structure. For that purpose, it was used the customized optical setup showed in Figure 3.27 present at INESC-MN. It is composed by a vacuum chamber, a laser and a photodetector. The chamber is pumped by a mechanical pump while a Pirani sensor (TPG300, Balzers) reads the pressure inside it. For these measurements, the vacuum created by the mechanical pump is enough to distinguish the resonance peak and various harmonics of the cantilevers, attaining roughly 20 mTorr. The laser is connected to a power source (E3641A, Agilent) which applies 2.2 V and a current limit of 0.1 A, producing a beam with approximately 30 μm of spot radius. This laser beam is focused on the cantilever to be measured and the reflected beam is captured by the photodetector (APD module C5331, Hamamatsu). The signal acquired by the photodetector is sent to a network/spectrum analyzer (4195A, Hewlett Packard) which plots the resonance spectrum of the cantilever. The chip where the structures are patterned is placed inside the chamber where it is established the interconnection with a DC power source and the AC power output of the spectrum analyzer for actuation. Since electrostatical actuation with an AC component produces an oscillatory motion, the reflected laser beam will be also oscillating around a certain position. This behaviour is felt by the photodetector as a variation in intensity since the laser beam is centered in the middle of the detector. By sweeping the frequencies of the AC component within an appropriate range, it is possible to detect the resonance frequency, characterized by a sudden increase in intensity.

After acquiring the data from the spectrum analyzer to a computer, it is possible to calculate the resonance frequency and the Q factor of the cantilever by fitting the data to a Lorentzian curve (Figure 3.28). The equation used for the fitting procedure is given by:

$$y = y_0 + \frac{2A}{\pi} \frac{FWHM}{4(x - x_c)^2 + FWHM^2} \quad (3.3)$$

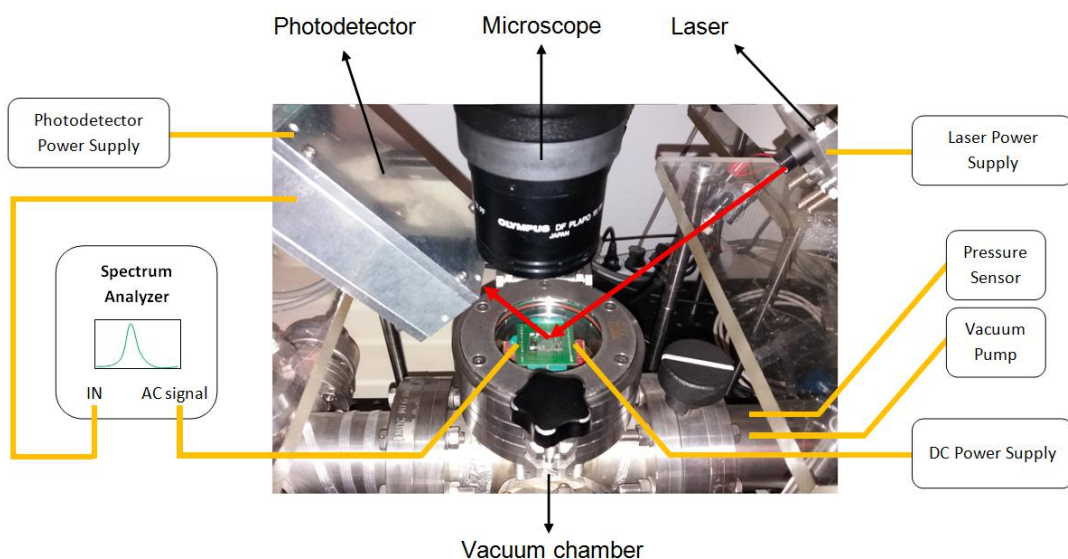


Figure 3.27: Schematics of the customized optical setup used for resonance measurements of the MEMS structures in vacuum.

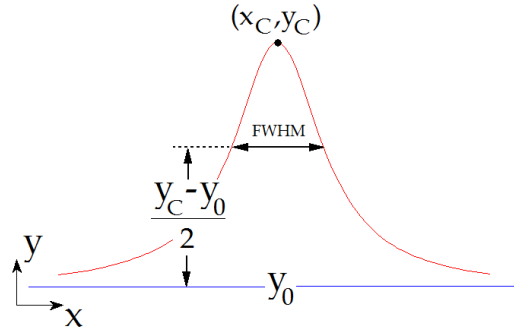


Figure 3.28: Lorentzian curve used for data fitting. Some general parameters are also represented.

where x_c is the frequency at maximum intensity, y_c , which corresponds to the resonance frequency and A is a normalization factor that is proportional to the electrostatic force. The Q factor is calculated from:

$$Q = \frac{x_c}{2\sqrt{0.107 FWHM^2}} \quad (3.4)$$

following the definition previously enunciated by equation 2.32. These results are important for the capacitive measurements in the static mode of operation because one needs to ensure that the applied low power AC component is not inducing resonance on the structure. Otherwise, it may start oscillating which compromises the results in this operation mode.

Capacitive setup for the static mode operation

The capacitive measurements are performed by a precision LCR meter (E4980A, Agilent) with a bandwidth ranging from 20 Hz to 2 MHz. It is used the parallel capacitance (C_P) and resistance (R_P) measurement mode because the capacitances under study are small, meaning that the series resistance (R_S) is less significant $R_S \ll R_P$. The DC level applied to the cantilever is fixed at 2 V. Also the AC component has 2 V_{PP} oscillating at 1.1 MHz. Both open- and short-circuit corrections are employed and the measurement time is set as long in order to guarantee maximum sensitivity. It is also possible to set the number of averages that the system must perform before sending the result. Since these particular measurements are very susceptible to noise, it is applied a shielded four-terminal pair configuration (Figure 3.29), characterized by the existence of two pairs of sensing probes: one for current sensing and the other for voltage readout. The shielding is accomplished by the incorporation of inner and outer conductors in the cables until they reach the device under test (DUT). This way, the current flows in both directions: towards the DUT by the inner conductor and towards the LCR meter by the outer one, resulting in the cancellation of the generated magnetic fields.

Because it is advantageous to implement differential measurements to the cantilevers, as discussed above, a double 8:1 multiplexer is interconnected with the LCR meter probes and the various outputs of the PCB where the chip is mounted. The multiplexer is responsible for successively switching between each cantilever terminal pair, in such a way that one is able to obtain intercalated measurements of the sensing cantilever and the reference one. The complete setup is showed in Figure 3.30.

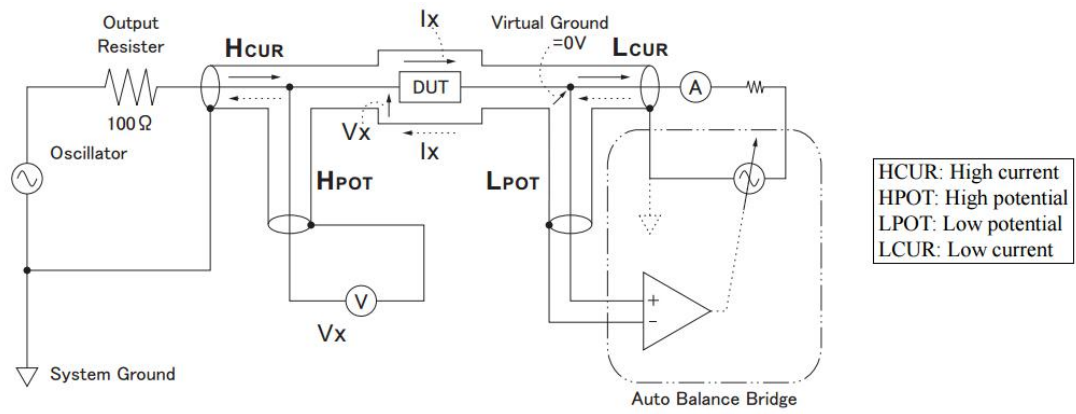


Figure 3.29: Schematics of the 4-terminal pair configuration with cable shielding. Two different pairs of terminals are used for sensing the voltage and the current simultaneously.

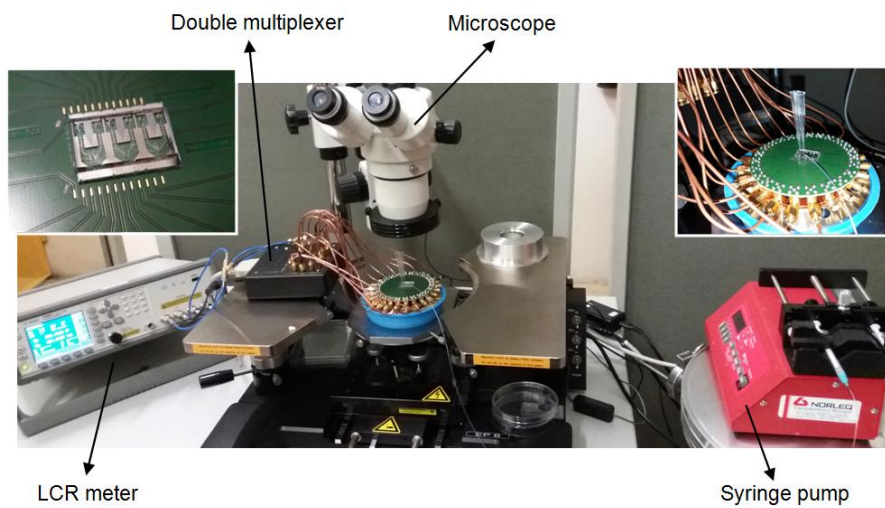


Figure 3.30: Setup used for the capacitive measurements in the static mode of operation of the cantilevers.

Chapter 4

Results

A first outlook over the various fabricated structures will be covered, including some considerations on any defects that may have arisen after any process. Then, a detailed discussion about the biological tests performed with the two designs of structures will be taken and the protocol that must be used in the capacitive measurements will be established according to this analysis. Finally, the capacitive measurements will be presented and some considerations about the performance of the structures and the sensing component will be made.

4.1 Fabrication outcome

4.1.1 Samples for biological tests

After the fabrication of the structures for the biological assays, they were imaged in an optical microscope to inspect and to infer on the quality of the process. Figure 4.1 presents some of the patterns created for the tests before integration with microfluidics. The thickness of each layer measured by the profilometer is listed in Table 4.1. In general, the shape of the a-Si:H is better defined due to the different technique used for its patterning. Etching produces more regular contours with sharper vertices, while lift-off tends to create irregularities in the contours and rounded vertices. In the first generation structures, the contrast between both techniques is more evident in the definition of the vertices of the rectangles. However, for the second generation ones, apart from the differences in sharpness of the vertices of each rectangle, it is clear the irregularity created by the lift-off at the borders of the TiW rectangles. Actually, Au contours are much smoother than TiW although they both have been patterned by lift-off. This happens due to the difference in rigidity of these two metals. The shear modulus, or modulus of rigidity, of TiW (> 50 GPa) is much higher than that of Au (≈ 28 GPa), making it more difficult to break the TiW film during the patterning process.

In Figure 4.2, it is shown the result of integration of microfluidics with the patterned structures. The alignment of both components was performed manually with the help of a stereo microscope, for that reason, it is not so perfect in some regions. It was also noticed that after peeling off the PDMS from the mold, it tends to shrink a few micrometers. Since the margins left between the rectangles and the walls

of the channels were very large, any consequence arising from the shrinkage of PDMS or misalignment was not so dramatic.

Some of the first structures to be produced suffered some problems when sealing the PDMS against the glass substrate. This occurred mainly due to inexperience, since the last groups of structures to be fabricated were strongly sealed. In fact, the more time it is spent positioning the PDMS in line with the patterns deposited on the substrate, the weaker is the bond between both surfaces. This happens because the oxidative reaction occurring in the plasma cleaner starts to be slowly reversed when the surfaces are brought into contact with the atmosphere. Due to this imperfection, some of the channels could not be used because PDMS started lifting from the glass in some regions.

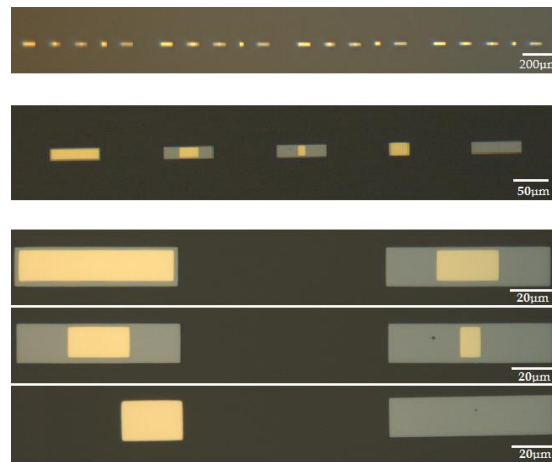


Figure 4.1: Images taken under the optical microscope with different magnification lenses. It is clear the difference in contours between the grey material (a-Si:H) and the golden one (Cr+Au) due to the different patterning techniques used.

Material	a-Si:H	Cr+Au	TiW
Expected Thickness (nm)	500	60	150
Measured Thickness (nm)	467 ± 29	57 ± 23	158 ± 38
Measured Roughness (nm)	150 ± 18	11 ± 5	8 ± 2

Table 4.1: Average thickness of each material used for the biological assays after deposition and patterning. The measured values correspond to the average of multiple measurements in the profilometer and its experimental error is obtained by the calculation of the standard deviation.

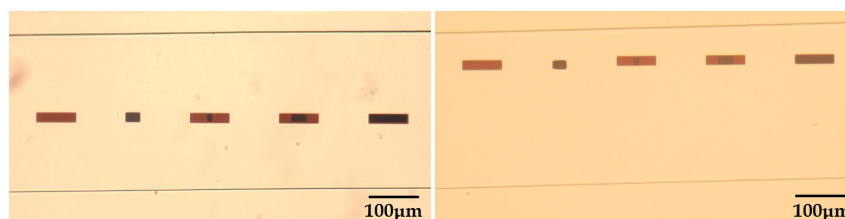


Figure 4.2: Structures after integration with microfluidics. *Left*: Reasonably well aligned channel and centered structures; *Right*: Although the channel is well aligned with the structures, they are not centered, possibly due to shrinkage of the PDMS.

4.1.2 Samples for stiction tests

In Figure 4.3, it is shown one die after release. In Table 4.2, it is listed the thickness of both materials measured in the profilometer. Globally, every cantilever was completely released, meaning that the wet etching reached the final point. It is also possible to observe some dark stripes on the longer cantilevers, which is expected since these are the cantilevers that suffered the effect of stiction, meaning that they got stuck to the substrate's surface. For that reason, some parts of the beams are bended which causes the light from the microscope to reflect towards another direction, resulting in darker regions.

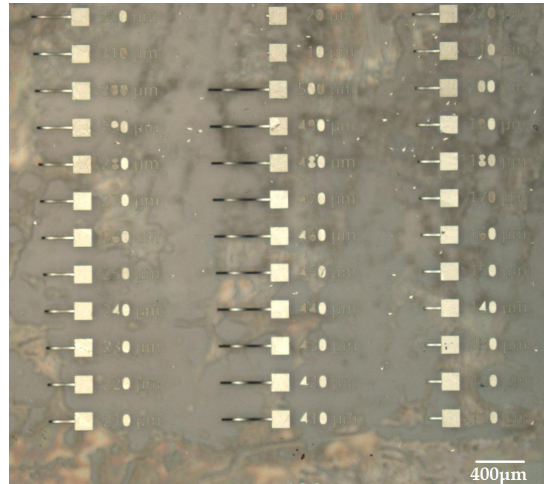


Figure 4.3: Image of one die after release by wet etching. The black stripes along the beams of the longer cantilevers are evidence of stiction.

Material	a-Si:H	Al sacrificial layer		
Expected Thickness (nm)	1000	400	600	800
Measured Thickness (nm)	9302 ± 524	421 ± 38	656 ± 41	841 ± 43
Measured Roughness (nm)	191 ± 20	62 ± 23	52 ± 24	57 ± 28

Table 4.2: Average thickness of each material used for the stiction tests. The measured values correspond to the average of multiple measurements in the profilometer. Since three different gaps were implemented, three different values are present for the sacrificial layer.

4.1.3 Samples for capacitive measurements

Different regions of one of the dies produced for the capacitive measurements in liquid is shown in Figure 4.4. All the layers seem to be very well defined and the thickness of each deposited layer is listed in Table 4.3. In the end, all structures survived to the release without collapsing and from the three substrates, only three cantilevers got compromised due to damaging or shortening of electrical lines. However, looking more closely, it is possible to notice, only in a few dies, a certain irregularity in the contours of the lifted-off ground plane and pads. Actually, due to some dust or metallic waste or even non-uniformities in the PR, the ground plane got damaged in a few locations. Nevertheless, it remains functional since only these few regions were affected.

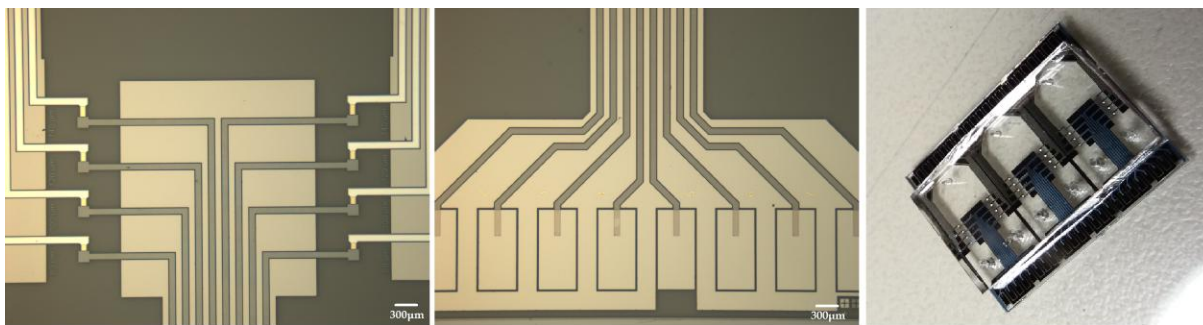


Figure 4.4: Set of images of the resultant structures for the capacitive measurements.

Material	a-Si:H	Al	TiW	Cr+Au
Expected Thickness (nm)	1000	1000	150	60
Measured Thickness (nm)	9711 ± 602	9693 ± 616	155 ± 47	56 ± 21
Measured Roughness (nm)	165 ± 24	96 ± 23	9 ± 3	10 ± 6

Table 4.3: Average thickness of each material used in the devices for the capacitive measurements. The measured values correspond to the average of multiple measurements in the profilometer and its experimental error is obtained by the calculation of the standard deviation.

By adjusting the focal plane of the microscope, it was possible to conclude that the cantilevers were curved upwards which means that they were suffering from a tensile stress. Such effect can be originated by two different causes (separately or conjugated): existence of tensile residual stress in the a-Si:H, Cr+Au and/or TiW film; and different linear thermal expansion coefficients (TiW: $5 - 8 \times 10^{-6} \text{K}^{-1}$; Au: $14 \times 10^{-6} \text{K}^{-1}$). Before starting the fabrication, the deposition conditions of TiW and a-Si:H have been recently optimized with the aim of reducing film residual stress. Furthermore, a tensile stress on the Cr+Au film would not affect so much the total stress given that its thickness is very small. For these reasons, the major contributors for this excessive stress may be in fact the different expansion coefficients. In terms of operation, the cantilever is still functional. A problem would arise if the stress was compressive because the gap between the beam and the substrate would decrease, resulting in smaller range of deflections that could be measured and higher probability of occurring stiction. Nevertheless, the height of the microchannels was increased up to $50 \mu\text{m}$ to prevent any damage on the cantilevers, as discussed in the previous section.

4.2 Biological tests

Testing chemiluminescence

Before testing immobilization and hybridization, it was necessary to understand which sensitivity could be achieved with this technique and how the conditions and parameters could be tuned in order to increase it. A simple protocol was employed in the first experiments (Protocol 4.1) only for probe immobilization.

{	Wash w/ IPA	20 $\mu\text{L}/\text{min}$ - 3min	(4.1)
	Wash w/ PBS	20 $\mu\text{L}/\text{min}$ - 3min	
	Probe-biotin (5 μM)	1.5 $\mu\text{L}/\text{min}$ - 10min	
	Wash w/ PBS	5 $\mu\text{L}/\text{min}$ - 1min	
	Labelling Strept-HRP	1 $\mu\text{L}/\text{min}$ - 10min	
	Wash w/ PBS	5 $\mu\text{L}/\text{min}$ - 1min	
	Luminol	10 – 20 $\mu\text{L}/\text{min}$	

The protocol is composed by two washing steps, insertion of biotinylated probe at a certain continuous flow, another washing step at a lower flow rate to remove the excess probe that did not bind to the Au (while maintaining the attached probes intact) and finally, the labelling of the probe with Strept-HRP. The parameters applied were based on some previous works with ssDNA at INESC-MN.

The results of this protocol are the ones shown in Figure 4.5, taken at different instants of time after starting flowing the luminol at two different velocities. It is also included a negative control which corresponds to the same protocol without the labelling step with Strept-HRP. First of all, it is clear that the signal degrades with time, meaning that the substrate of the reaction is getting consumed gradually. This result may also originate from some probes being washed away when flowing a liquid at such high speeds. It was observed that the system needs roughly 30 s to achieve a stable signal. Furthermore, higher flow rates return higher signals because more luminol is flowing in the same volume for a certain time interval. However, lower flow rates seem to have a more stable signal for longer periods of time which occurs because HRP reacts with luminol at a lower rate, so less substrate is consumed for the same period of time. By observing the pictures carefully, it is possible to detect a higher intensity on the patterned structures than on the PDMS/glass background. This does not necessarily mean that the signal comes from immobilized probes on Au surface. In fact, the stronger intensity may be due to reflection of the neighboring signal from probes attached to the glass or a-Si:H.

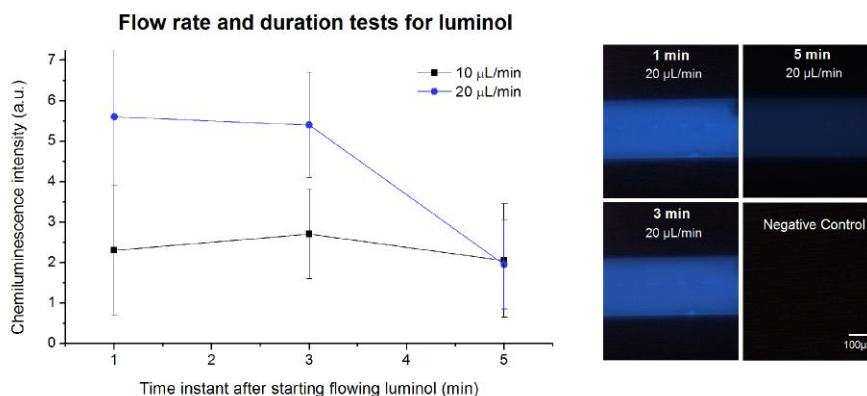


Figure 4.5: Results obtained by chemiluminescence by varying the flow rate of luminol and the instant of the measurement. *Left*: Plot of the signal on Au surfaces measured in three different instants at 10 and 20 $\mu\text{L}/\text{min}$; *Right*: Pictures taken from the microscope during the measurement at 20 $\mu\text{L}/\text{min}$.

From this first experiment, it was established a compromise between the duration and flow rate of the last step. The flow rate of luminol was fixed at $20 \mu\text{L}/\text{min}$ and the measurements were all taken between the first half-minute and the third minute after starting flowing it. Consequently, a strong signal is obtained and the results are taken after stabilization of the signal and before a dramatic decrease in probe density. It was also noticed the need to find which was the origin of the strong intensity on Au.

According to the literature [58], a buffer containing 1M TE NaCl would be more appropriate for this assay because the high concentration of salt allows a stronger shielding between ssDNA molecules, reducing the intensity of the repulsions between them. In a different assay, using the same protocol, PBS was substituted by 1M TE NaCl and in fact the signal on Au increased almost 25% (Figure 4.6). From this point forward, only TE NaCl was used in the protocols.

A pair of similar experiments focused on the effect of probe flow rate (Figure 4.7). In this case, the flow rate at which the probe was passing through the channel was changed to 0.25 and $0.75 \mu\text{L}/\text{min}$. Since the duration of probe insertion was not changed (10 min) it would be expected that at a higher flow rate, the signal would be more intense since the total quantity of available probes in solution is higher, which was validated by the results. Also important to evaluate is the variability of results along the channel. It is concluded that these variations of signal in the channel are negligible.

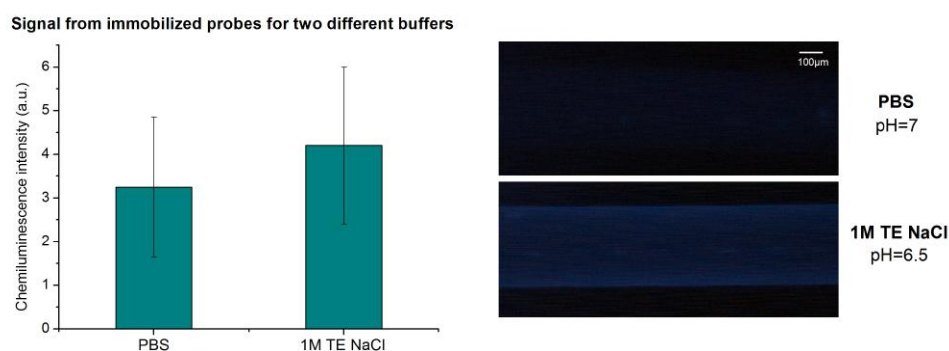


Figure 4.6: Results obtained by chemiluminescence when using PBS and 1M TE NaCl as buffers. *Left*: Plot of the signal on Au surfaces measured for both solutions; *Right*: Pictures taken from the microscope during both measurements.

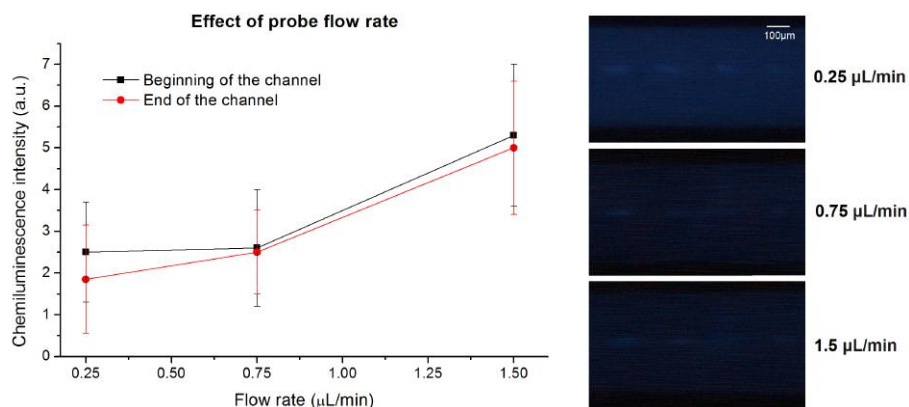


Figure 4.7: Results obtained by chemiluminescence by varying the flow rate of the probe inside the channel. *Left*: Plot of the signal on Au surfaces measured for three different probe flow rates; *Right*: Pictures taken from the microscope during the measurement.

Blocking agent and incubation of probe

By promoting a general increase of signal while blocking the access of the probes to the PDMS/glass surfaces, it could be possible to understand where is the signal on Au coming from. With this intention, a new protocol was created with more steps (Protocol 4.2), including a blocking step with a certain molecule that could get attached everywhere but on the Au surface and an additional incubation procedure after probe insertion. Three different blocking agents were compared and different durations of incubation were tested. Regarding the incubation, the results are presented in Figure 4.8, where the signal on the Au surface is plotted as function of duration of incubation.

{	Wash w/ IPA	20 $\mu\text{L}/\text{min}$ - 3min	(4.2)
	Wash w/ TE NaCl	20 $\mu\text{L}/\text{min}$ - 3min	
	Blocking agent	0.75 $\mu\text{L}/\text{min}$ - 15min	
	Wash w/ TE NaCl	5 $\mu\text{L}/\text{min}$ - 1min	
	Probe-biotin (5 μM)	0.75 $\mu\text{L}/\text{min}$ - 10min + incubation	
	Wash w/ TE NaCl	5 $\mu\text{L}/\text{min}$ - 1min	
	Labelling Strept-HRP	1 $\mu\text{L}/\text{min}$ - 10min	
	Wash w/ TE NaCl	5 $\mu\text{L}/\text{min}$ - 1min	
	Luminol	20 $\mu\text{L}/\text{min}$	

From the plot, it is inferred that with increasing time interval of incubation, higher is the measurable signal and higher the background level also. This means that although more probes are getting attached to the channel walls, the immobilization on gold increases with a higher pace. Since during incubation there is no insertion of new probe, it is suggested that these probes need some time for reorganization in solution so that they can create the bonds between thiol and gold. It is also interesting that, even with 48h of incubation, the probe density does not reach the saturation level which is beneficial for hybridization. For the sake of compromise, it was established an incubation of 24h for the following assays.

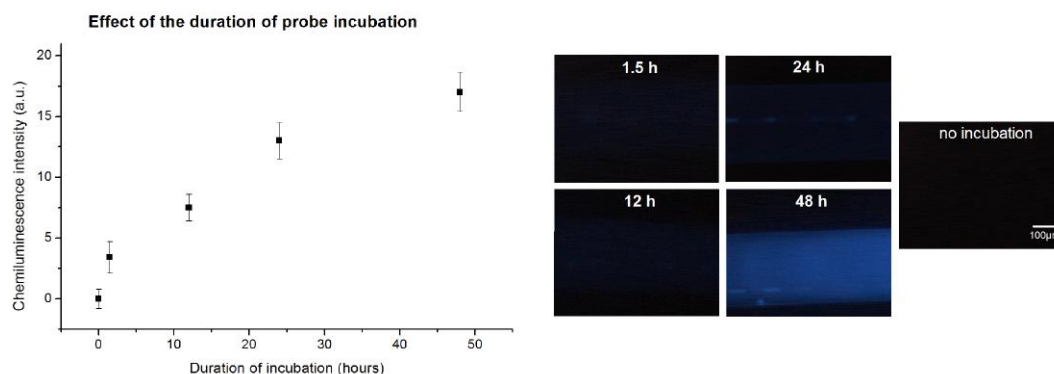


Figure 4.8: Results obtained by chemiluminescence when a different incubation duration is implemented. *Left*: Plot of the signal on Au surfaces measured for various durations of incubation; *Right*: Pictures taken from the microscope during each measurement.

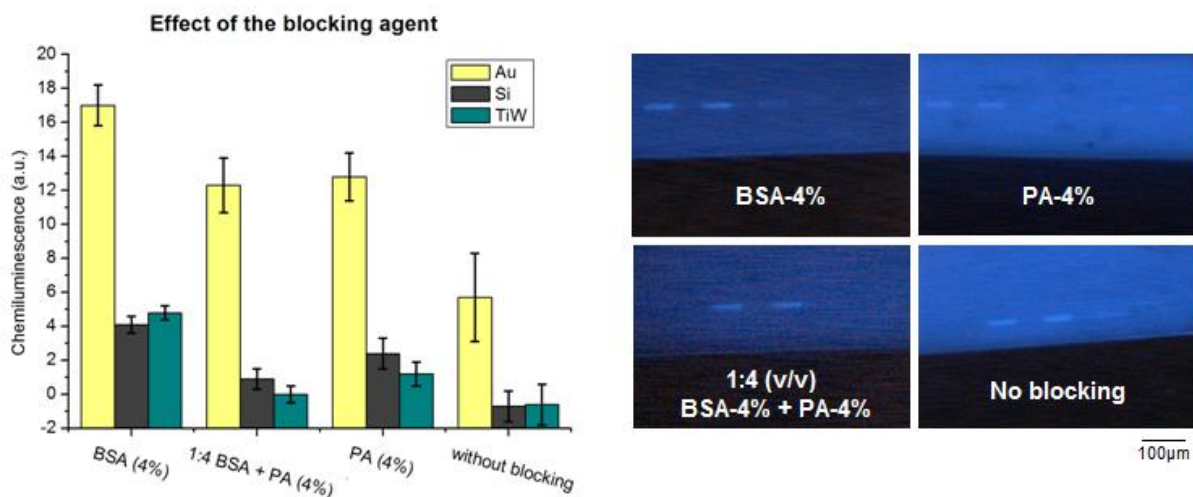


Figure 4.9: Results obtained by chemiluminescence when different blocking agents are used. *Left*: Plot of the signal on Au, TiW and PDMS/glass surfaces measured for various blocking materials; *Right*: Pictures taken from the microscope during each assay.

Blocking agent	None	BSA-4%	PAA-4%	1:4 BSA+PAA 4%
PDMS/glass signal (a.u.)	35 ± 5	14.0 ± 0.5	32 ± 2	22 ± 5

Table 4.4: Chemiluminescence intensity on PDMS/glass in arbitrary units for the different assays with blocking agents.

In parallel, it was obtained the plot in Figure 4.9 for the comparison between blocking agents. The plot is followed by Table 4.4 which comprises various signals obtained on top of PDMS/glass. For this experiment it was used BSA-4%, PAA-4% and a mixture of 1:4 (v/v) PAA-4% with BSA-4% with the probe incubation step. As a positive control, it was used the same protocol without any blocking step.

By analysing the raw intensity signal on PDMS/glass background, one infers that this is lower when using solely BSA-4% or the mixture, reporting background intensity reductions of 31% and 37%, respectively. This means that the PAA is blocking some regions of the PDMS/glass that BSA is not able to block. PAA has smaller dimensions than BSA and the second has a rounded shape, so possibly PAA is occupying the free spaces between BSA molecules, obtaining a more uniform coverage of the channel with the mixture of molecules. However, the plot shows that the calculated signal on Au is higher when BSA is the blocking agent. If the raw intensity signal on Au was the same in every case, then the calculated signal on Au should be higher for the mixture of blocking molecules. Since this is not the trend, it is clear that some of the PAA is also blocking the Au surface, decreasing the density of immobilized probes. In the end, the blocking agent that seems more appropriate is BSA-4%. It is also interesting to see that the raw intensities on gold in the various assays does not change so significantly, suggesting that the signal is really coming from immobilized probes on the surface of Au. For the first time, it was used the structure of the second generation which includes TiW patterns. As one may observe, the immobilization on this material is almost negligible, indicating that, in principle, it is possible to achieve the differential surface stress on the cantilever for capacitive measurements in the static mode.

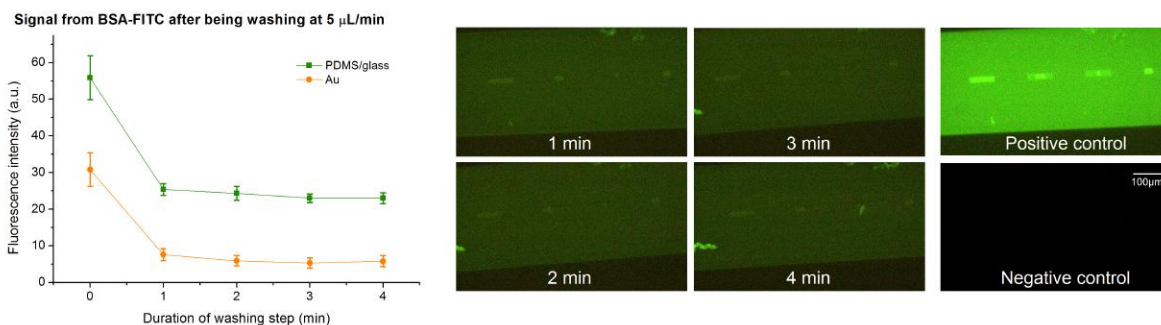


Figure 4.10: Results obtained by fluorescence from BSA marked with FITC after being washed multiple times with a constant flow rate of 5 $\mu\text{L}/\text{min}$. *Left*: Plot of the signal of BSA on Au and PDMS/glass surfaces measured after each minute of washing (the results for PDMS/glass correspond to the raw measurement); *Right*: Pictures taken from the microscope for each minute.

To better exclude the possibility of the signal on Au being originated by reflection of signal coming from probes in the vicinity, a darker background would be desirable. In order to evaluate if the blocking agent was getting washed away during the execution of the protocol, BSA marked with FITC was used in order to track its density along various washing steps at 5 $\mu\text{L}/\text{min}$. The results can be found in Figure 4.10. In this case, the negative control corresponded to flowing just TE NaCl at the same velocity but without the marked BSA, while the measurements taken before washing the BSA serve as positive controls.

From the results obtained on PDMS/glass surface, it is possible to conclude that the blocking agent is not being significantly removed during the washing steps. The signal before washing (positive control) has a great intensity not because there is a huge amount of BSA attached to the surface but because there is a considerable density of these molecules in solution. Although there is a distinct signal on gold, the major contribution should be in fact due to signal reflection from BSA molecules present in the neighboring surfaces since the evolution of the signal on this surface follows the trend of PDMS/glass signal.

Non-specific adsorption

The fact that the negative control in the first assay where the luminol flow rate was being tested revealed no signal (Figure 4.5), supports the idea that the signal on PDMS/glass is originated by the probes and not by non-specific adsorption of Strept-HRP on the channel walls.

In order to ensure that the signal on Au is relative to specific adsorption of the thiol groups linked to the ssDNA and not a result of non-specific adsorption of the ssDNA oligomers on Au, a simple test was performed. In this pair of assays, it was used a probe with thiol group and another one without this termination. The results when implementing the optimized Protocol 4.3 are summarized in Figure 4.11.

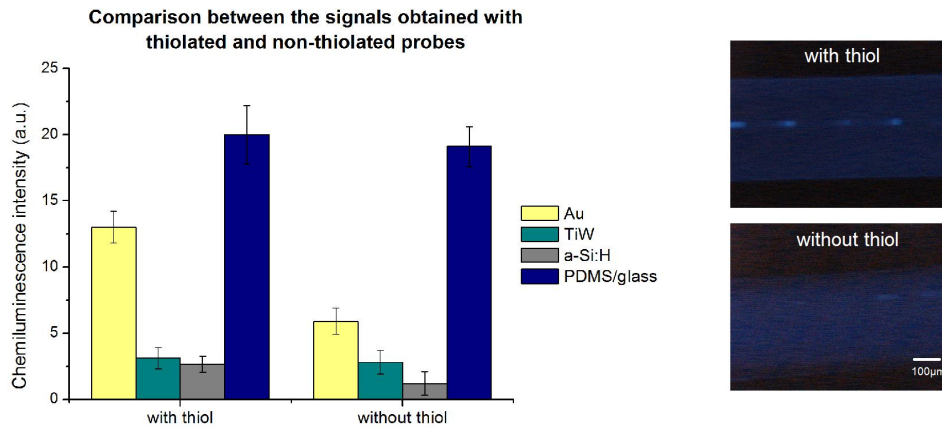


Figure 4.11: Results obtained by chemiluminescence when using thiolated and non-thiolated probes. *Left*: Plot of the signal on Au, TiW, a-Si:H and PDMS/glass surfaces measured for both types of probes (the results for PDMS/glass correspond to the raw measurement); *Right*: Pictures taken from the microscope for each assay.

}	Wash w/ IPA	20 µL/min - 3min	(4.3)
	Wash w/ TE NaCl	20 µL/min - 3min	
	BSA-4%	0.75 µL/min - 15min	
	Wash w/ TE NaCl	5 µL/min - 1min	
	Probe-biotin (5 µM)	0.75 µL/min - 10min + 24h incubation	
	Wash w/ TE NaCl	5 µL/min - 1min	
	Labelling Strept-HRP	1 µL/min - 10min	
	Wash w/ TE NaCl	5 µL/min - 1min	
	Luminol	20 µL/min	

Although it is possible to distinguish two Au patterns in the picture relative to the assay without thiol, the signal on the other assay is much more intense while the background remains the same. The result confirms that the major contribution to the signal on Au is due to specific adsorption of the thiol group, however, some non-specific adsorption and/or reflection from the vicinities have some weak influence. Because in this experiment the background does not change between assays, it is inferred that the background signal is emitted from probes that are adsorbed on the PDMS/glass, creating bonds with the oligomers and not with the thiol group. Another important aspect is that the good selectivity of thiol groups to Au is again confirmed when comparing with TiW and a-Si:H.

Further insight into incubation and background signal

In order to improve the ratio between the signal on Au surfaces and the background signal (PDMS/glass), it was implemented the same protocol but with a decreased probe flow rate and duration of incubation. The different combinations of flow rates and incubation procedures are listed along with the results for the signal on Au surfaces for each assay (Figure 4.12).

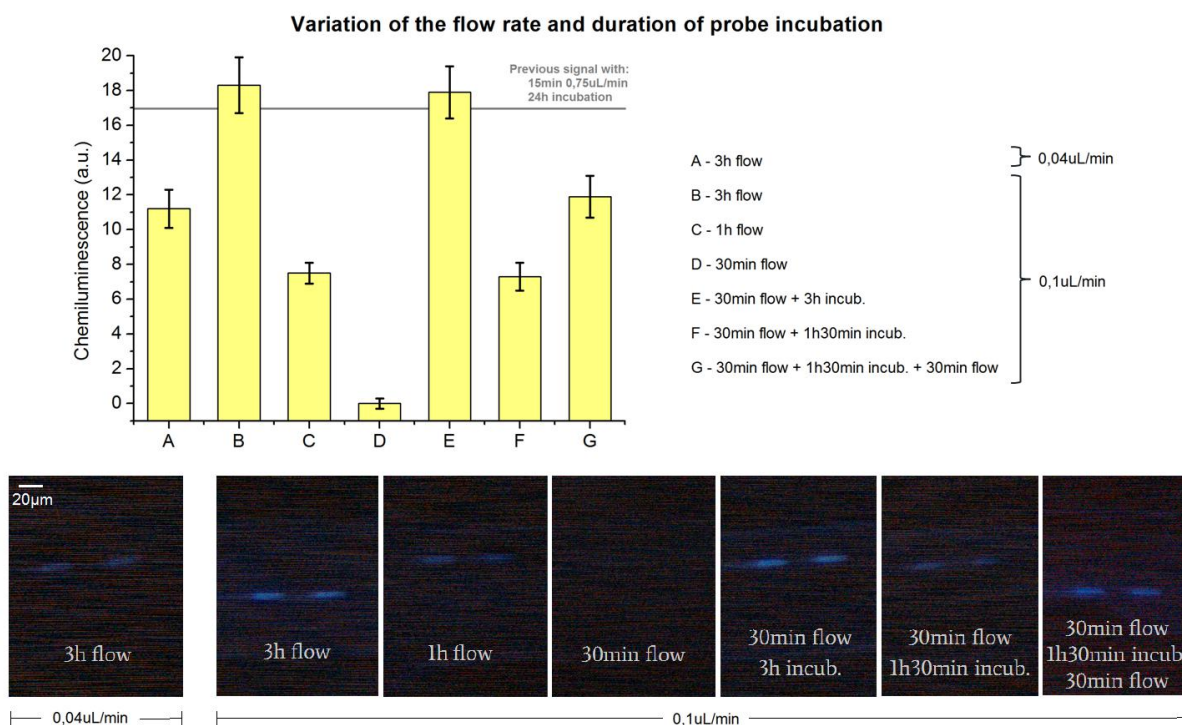


Figure 4.12: Results obtained by chemiluminescence when implementing different procedures for probe flow and incubation. *Left*: Plot of the signal on Au surfaces measured with two different flow rates and different duration of flow and incubation; *Right*: Pictures taken from the microscope for each assay.

First of all, it is important to note that these results were extracted from images obtained with lower amplification because the signal was so low that the regular lens used in the previous experiments could not capture a distinguishable signal. Having this in mind, one should not forget that even if the intensity in this plot is high, the real density of probes is much lower than in previous assays. Nevertheless, some interesting behaviours and trends can be inferred. The same trend of increased signal with increasing flow rate (A and B) and duration of incubation (F and E) is clear. However, it is possible to compare the relative effect of the parameters under test. One may observe that when changing the duration of flow rate and the duration of incubation in a similar amount, the variation in signal is not so different, meaning that both parameters promote the similar trends. Nevertheless, it is always preferable to use a protocol with incubation than with continuous flow when the duration of both procedures is the same because less biological material is consumed. Another very important aspect that can be analyzed with these results is the background signal. It is visible the decrease in the background signal when any of these protocols are used. The cause of such result is simply related with the less quantity of probe that is being used and the less time for probe reorganization and possibly adsorption on the PDMS.

Testing hybridization

After having a full insight on probe immobilization and an optimized assay for that purpose, it was necessary to proceed towards DNA hybridization. Given the promising results obtained in the last experiments of probe immobilization in terms of reduction of background signal, it was implemented the Protocol 4.4 for hybridization with the assay that returned a higher signal for immobilization.

{	Wash w/ IPA	20 $\mu\text{L}/\text{min}$ - 3min	(4.4)
	Wash w/ TE NaCl	20 $\mu\text{L}/\text{min}$ - 3min	
	BSA-4%	0.75 $\mu\text{L}/\text{min}$ - 15min	
	Wash w/ TE NaCl	5 $\mu\text{L}/\text{min}$ - 1min	
	Probe (5 μM)	0.1 $\mu\text{L}/\text{min}$ - 30min + 3h incubation	
	Wash w/ TE NaCl	5 $\mu\text{L}/\text{min}$ - 1min	
	Target-biotin (5 μM)	0.75 $\mu\text{L}/\text{min}$ - 15min	
	Wash w/ TE NaCl	5 $\mu\text{L}/\text{min}$ - 1min	
	Labelling Strept-HRP	1 $\mu\text{L}/\text{min}$ - 10min	
	Wash w/ TE NaCl	5 $\mu\text{L}/\text{min}$ - 1min	
	Luminol	20 $\mu\text{L}/\text{min}$	

The result of such assay is presented in Figure 4.13 along with the result for a similar assay with incubation of the target DNA for 3h after flowing it in the same conditions. It is visible some weak signal near the margins of the channel, but no structure is distinguishable. The background signal is higher in the assay with target incubation which is only a result of reorganization of target molecules originating non-specific adsorption on PDMS and glass. Given this scenario, two explanations can be assumed. Either the target DNA is not hybridizing due to large probe density on Au surfaces, or the yield of such process is so small that the signal from the few hybridized molecules is very low. The same experiment was performed with a lower duration of probe incubation (lower probe density on Au surface) but a similar image was obtained without any visible structure.

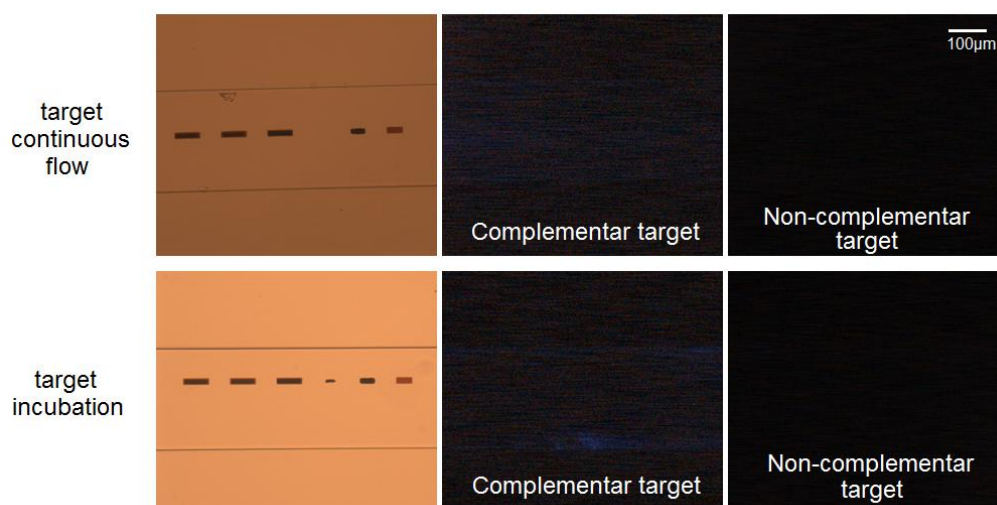


Figure 4.13: Results obtained by chemiluminescence for hybridization after incubation of probe for 3h. *Left:* Pictures taken from the microscope for the assay with continuous flow of target at 0.75 $\mu\text{L}/\text{min}$; *Right:* Pictures taken from the microscope for the assay with target incubation for 3h after flowing for 5 min.

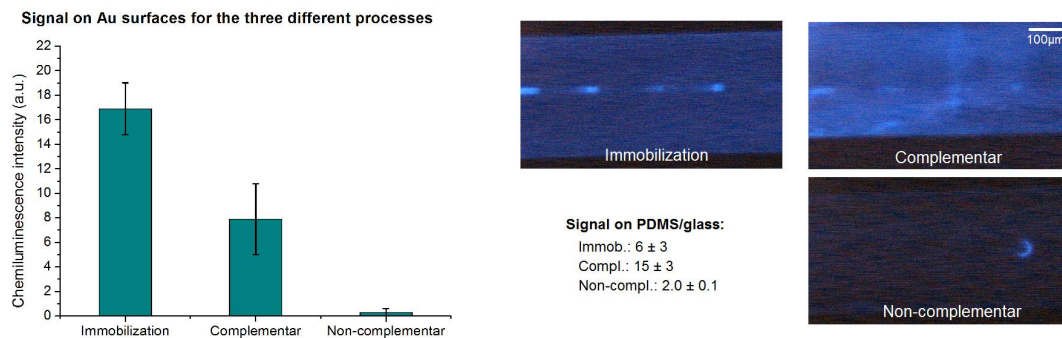


Figure 4.14: Results obtained by chemiluminescence for hybridization after incubation of probe for 24h and continuous flow of target. The measured signal on PDMS/glass surfaces is also indicated for each type of assay. *Left*: Plot for the three different events tested with the assays; *Right*: Pictures taken from the microscope for each assay and the measured signal on PDMS/glass.

With the aim of verifying if the problem was related with low yield of hybridization, an additional assay with the previous protocol for probe immobilization with an incubation of 24h was implemented followed by target molecule flow (Protocol 3.1). The results of such assay are presented in Figure 4.14. It is relevant to refer that separate assays need to be performed in order to track both immobilization and hybridization processes because it is not possible to distinguish the signal from the targets and the probes when both molecules are labelled simultaneously.

With this protocol, it is reached hybridization of ssDNA probes with the targets. The signal of the hybridization with the complementar target is almost one half of that of immobilization. If the problem was an excessive probe density, then it would not be possible to detect signal in this case in which there are much more immobilized probes on the surface. With this statement, it is confirmed that the low yield of such process was the cause for not detecting any distinguishable signal on the previous hybridization experiments. However, the selectivity of the process is extremely high given the disparity between the signals obtained with complementar and non-complementar targets. Such result is in fact expected because the non-complementar target sequence of nucleobases was chosen in order to maximize the mismatch between them.

Regarding the background signal on PDMS/glass, the hybridization with a complementar target originates a higher non-specific signal when comparing with immobilization (more than the double). The reason for such increase may be related not only with hybridization of immobilized probes on PDMS/glass surface but also with adsorption of target molecules on the same surface along with a partial washing of some BSA molecules. This last reason seems to have a strong influence because it is noticed a non-uniformity on the intensity of the background signal along the entire channel. On the contrary, non-complementar assays return a very low background signal because it is not expected that the target binds with the probe, having only the contribution of direct target adsorption on the surface.

An additional experiment was performed in order to track the quantity of BSA that is present along the entire assay of immobilization and hybridization. For such purpose, the protocol was ran in the same conditions but using BSA-FITC and non-labelled target instead of the regular non-labelled BSA and the biotinylated target. The results are shown in Figure 4.15.

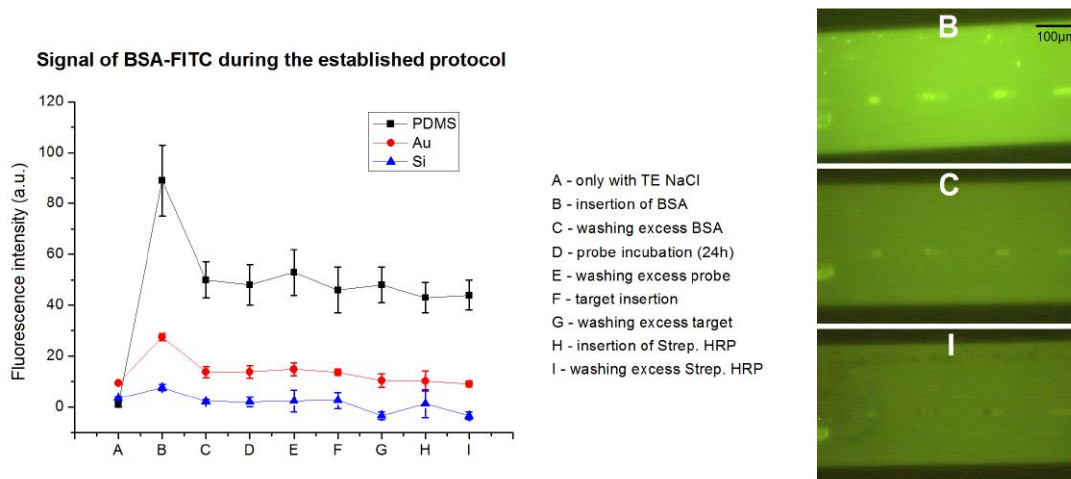


Figure 4.15: Results obtained by fluorescence in order to track the density of BSA molecules along the entire protocol for hybridization. The measured signal on PDMS/glass surfaces corresponds to the raw signal obtained by the software. *Left*: Plot of the signal intensity measured for each step of the protocol; *Right*: Pictures taken from the microscope for some particular steps of the entire protocol.

Apparently, BSA molecules do not suffer an excessive decrease in density upon the multiple washing steps included in the protocol. However, the same type of non-uniformity in the intensity signal on PDMS/glass surface is noticed near the end of the protocol, suggesting that some kind of reorganization or partial remotion of BSA molecules is in fact occurring. Furthermore, it is important to bare in mind that the sensitivity of fluorescence techniques is lower than that of chemiluminescence, meaning that a variation in signal obtained with this technique corresponds to a higher variation when using the last mentioned one. So, although the variation of the signal seems to be negligible, it may in fact be affecting the blocking of the channel being only possible to detect such variation with chemiluminescence.

In the end, it is created a protocol that is able to produce not only probe immobilization but also target hybridization with a great selectivity to the Au surface. This is important in order to ensure that when this assay is implemented with a cantilever as sensor, a different density of probes and targets is attached to each surface of the beam, producing the desired differential surface stress. In addition, also a high selectivity is attained in the hybridization process, validating the implementation of the non-complementar target assay as a reference assay for the differential capacitive measurements in the static mode of operation of cantilevers.

Testing fluorescence

Along with chemiluminescence, also detection by fluorescence was tried, specially because the protocol is composed by fewer steps (Protocol 4.5). A simpler protocol means less washing steps which results in less immobilized probes and hybridized targets getting washed away. Nevertheless, this is a difficult technique to use when imaging on metal surfaces because some more exotic phenomena may occur (quenching, for example). After using the protocol for probe immobilization with 24h of incubation, the results are the ones shown in Figure 4.16. As a negative control, it is used an empty channel and as positive one, a channel full of probes ($5 \mu M$) is measured.

}	Wash w/ IPA	20 $\mu\text{L}/\text{min}$ - 3min	(4.5)
	Wash w/ TE NaCl	20 $\mu\text{L}/\text{min}$ - 3min	
	BSA-4%	0.75 $\mu\text{L}/\text{min}$ - 15min	
	Wash w/ TE NaCl	5 $\mu\text{L}/\text{min}$ - 1min	
	Probe-biotin (5 μM)	0.75 $\mu\text{L}/\text{min}$ - 15min + 24h incubation	
	Wash w/ TE NaCl	5 $\mu\text{L}/\text{min}$ - 2min	

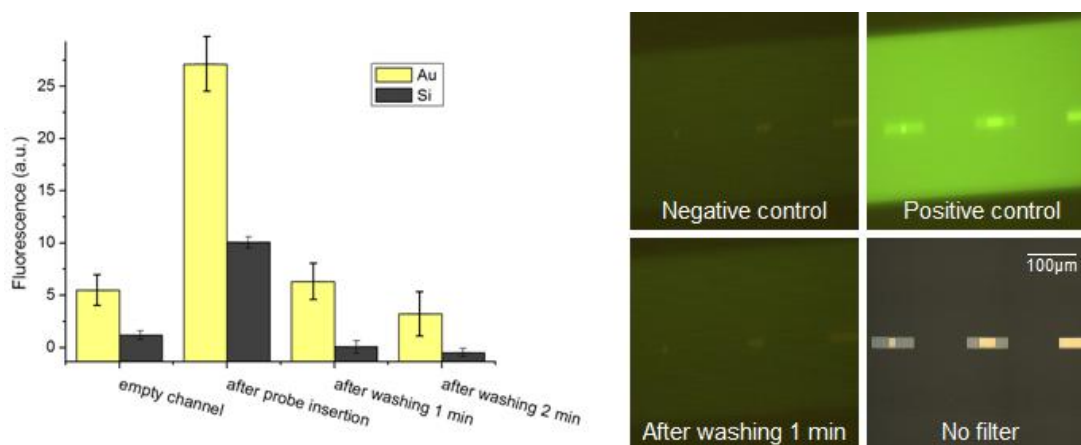


Figure 4.16: Results obtained by fluorescence. *Left*: Plot of the signal on Au and a-Si:H surfaces measured in four different instants; *Right*: Pictures taken from the microscope during the measurement.

Both plot and set of pictures indicate that the signal after washing the excess probe from the channel returns to similar values obtained from an empty channel. It is proven by chemiluminescence that the protocol works, so if fluorescence was working according to the expected, it should be noticeable some signal above the negative control, even after washing the probe for 1 min. Such behaviour is typical of quenching. It is known that when the fluorophore is very close to the metal surface, it suffers quenching and no light emission is observed. In fact, this distance is relatively small (accounting only for the six CH_2 links, the five-adenine spacer and the oligomer with 23 nucleobases), so it was tried a different molecule with a larger spacer between the thiol group and the ssDNA (instead of six CH_2 links, it was composed by forty-five). The results proved to be very similar: the signal after washing for 1 min is close to the negative control (Figure 4.17). From here, only two situations may be occurring. Or the molecules are still being quenched by the Au surface, or the signal is so low that this fluorescent technique is not sensitive enough. Actually, when comparing with other work that uses the same equipment and acquisition parameters [56], a signal of chemiluminescence around 15 a.u. should be detectable with fluorescence, so the reason must be quenching indeed.

After properly analysing these results, fluorescence was abandoned and only chemiluminescence was used for the remaining tests.

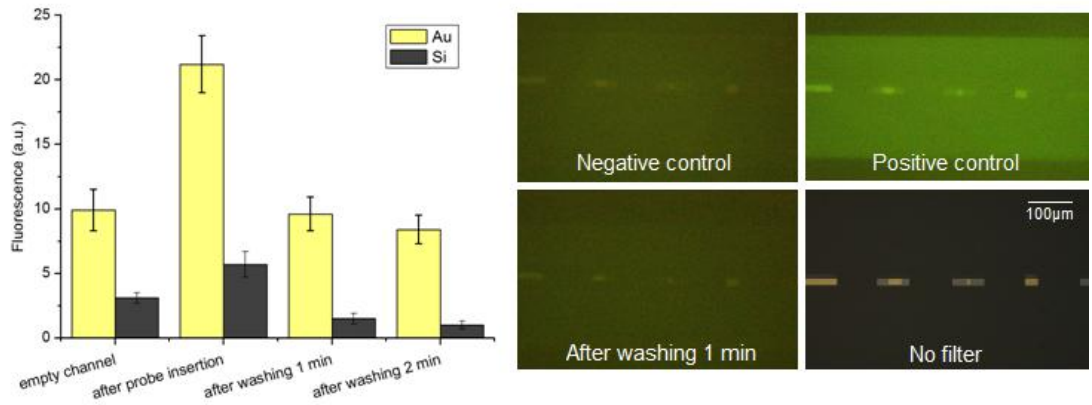


Figure 4.17: Results obtained by fluorescence for longer molecules. *Left*: Plot of the signal on Au and a-Si:H surfaces measured in four different instants; *Right*: Pictures taken from the microscope during the measurement.

4.3 Stiction tests

As explained previously, two different release protocols were applied to the two sets of dies. One of the protocols is the standard release protocol used at INESC-MN comprising a sequential immersion of the die in Al etchant, DI water, IPA and n-hexane. The other one is a simpler procedure using only Al etchant and DI water. The purpose of this comparison was to understand if the additional solutions produce in fact any change in the release and to quantify it.

From the optical inspection of the released dies under the microscope, one should obtain the value of the detachment length for each cantilever. With this result and by knowing the dimensions of the structures and the properties of the materials being used, it is possible to determine the work of adhesion given in equation 2.47. The two quantities that are allowed to vary are the detachment length and the gap, so if one plots the first as function of the second, a simple fitting procedure to the previously mentioned equation will return the value of work of adhesion for each of the release protocols.

The plots in Figure 4.18 show the fraction of cantilevers that adhered to the substrate as function of the length of the beam for the two protocols under study.

In Figure 4.19, it is represented the resultant fit to the equation of the work of adhesion with the values obtained by this analysis and the measurements used for the procedure.

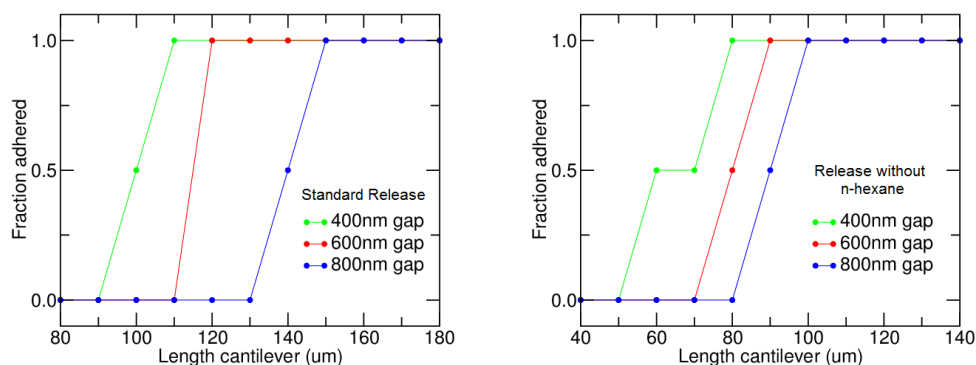
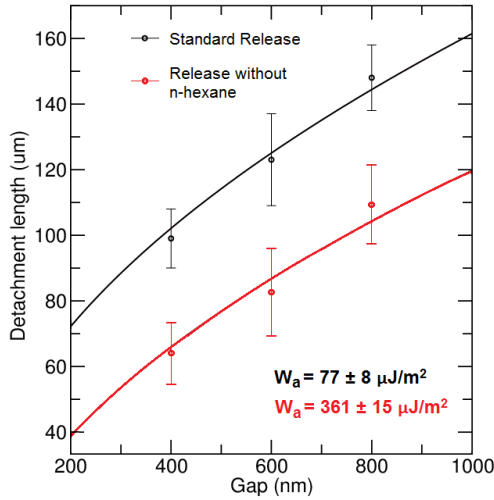


Figure 4.18: Plots of the fraction of adhered cantilevers as function of the length of the beam. *Left*: Standard release; *Right*: Release without using n-hexane.



Release protocol	Gap (nm)	l_d (μm)
Standard	400	99 ± 9
	600	123 ± 14
	800	148 ± 10
No n-hexane	400	64 ± 7
	600	78 ± 10
	800	107 ± 9

Figure 4.19: Fit of the function of the work of adhesion when using the standard protocol and the release without n-hexane. The measurements of detachment length are also listed in the table.

Because n-hexane is a liquid with really low surface tension, the corresponding protocol has a higher detachment length and a lower work of adhesion ($W_a = 77 \pm 8 \mu\text{J}\cdot\text{m}^{-2}$). This means that the forces attracting the beam towards the substrate during release are substantially reduced when the standard protocol is used. Since in the static mode the sensitivity is strongly dependent on the aspect ratio of the beam, this standard release is the one used for the MEMS of the capacitive measurements, so that longer beams can be used without compromising its integrity. Other research groups report work of adhesion results ranging from tens to hundreds of $\mu\text{J}\cdot\text{m}^{-2}$, validating the values obtained. In the end, this result is a valuable tool when trying to design a cantilever or even other structure with a known equation for its work of adhesion, since the dimensions can be tuned in order to prevent stiction effects.

4.4 Resonance measurements

Before proceeding to the capacitive measurements, it would be necessary to measure the resonance frequency of the MEMS devices integrated with microfluidics. As described previously, the cantilevers were excited with an AC signal biased with a DC voltage and the resultant resonance frequency was acquired by the analysis of a reflected laser beam. The measurements were performed under vacuum conditions, at a pressure of 23 mTorr. The results obtained after fitting a Lorentz curve to each resonant mode are summarized in Table 4.5 for three different lengths of cantilevers. The experimental error of the resonance frequency is calculated from the $FWHM$ value that is extracted as a parameter of the fit, $\sigma_{f_r} = FWHM/2\sqrt{2\ln 2}$. Unfortunately, it was not possible to measure the resonance frequency and the various harmonics of the longest cantilever (140 μm) because the few structures that did not suffer from stiction, ended up being damaged during some failed sealing procedures.

The spectrum containing the resonance peaks and harmonics is shown in Figure 4.20 along with a single peak as an inset for exemplification of the fitting procedure. Since the voltages used for actuation were higher for higher vibrational modes, the relative intensity of the peaks cannot be directly compared.

Length	Mode	f_r (kHz)	Q	V_{DC} (V)	V_{AC} (V_{pp})
80 μm	1	114.8 ± 0.1	665	2	0.2
	2	689.9 ± 0.8	555	2	0.2
	3	1856 ± 2	698	4	0.3
	4	2490 ± 2	873	6	0.5
100 μm	1	74.3 ± 0.1	458	2	0.2
	2	441.6 ± 0.7	407	2	0.2
	3	1298 ± 2	508	3	0.2
	4	2131 ± 2	822	7	0.5
120 μm	1	51.66 ± 0.05	666	2	0.2
	2	304.1 ± 0.3	581	2	0.2
	3	903.3 ± 0.9	682	4	0.3
	4	1778 ± 2	716	8	0.5
	5	2280 ± 2	975	12	0.5

Table 4.5: Resonance frequency and Q factor for each mode of vibration obtained by fitting a Lorentz curve. The voltages used for actuation of the cantilevers are also presented.

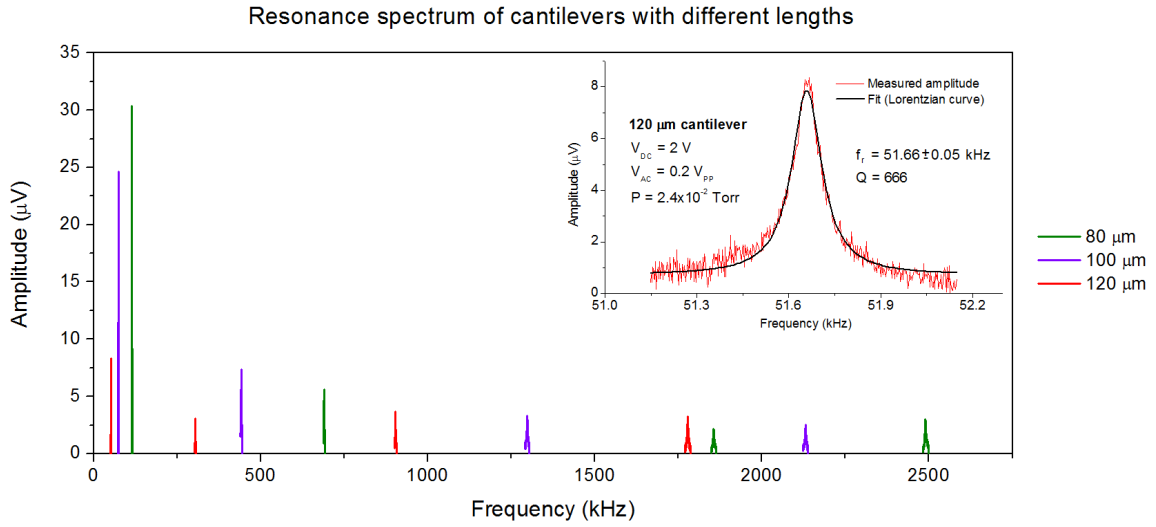


Figure 4.20: Resonance spectrum of each cantilever. The intensity of the various harmonics cannot be directly compared because higher voltages were used for actuation for higher harmonics. *Inset*: Plot of a resonance peak with a Lorentz curve fit and the extracted parameters.

The resonance frequencies experimentally obtained are lower than the ones predicted by equation 2.30, when assuming a Young's modulus of the a-Si:H of 120 GPa and a density of the same material of $2330 \text{ kg}\cdot\text{m}^{-3}$. The fact that the cantilever is composed by a multilayer of materials, will affect the mechanical behaviour of the structure since the elasticity of the various deposited films is different. Furthermore, because the cantilevers had a visible compressive residual stress, the oscillatory motion can suffer some variations to the expected since this is not the base geometry of the model. Finally, for increasingly higher gaps between the cantilever beam and the substrate, some non-linearities start shifting the trend of evolution of these frequencies.

From these preliminary results, it is important to evaluate which is the best frequency value for actuation of the cantilevers in the static mode. It needs to be a frequency that does not correspond to the natural frequency of the structure neither its harmonics in order to prevent an oscillatory motion. Having this in mind, it was defined 1.1 MHz as working frequency for the AC signal supplied in the capacitive measurements.

Regarding the Q factor, not many trends can be accessed because different actuation voltages were used. Nevertheless, for increasing voltages it is registered an increase in the quality factor which is a result of the larger amount of energy that is used for the actuation, while maintaining the same dissipation mechanisms.

4.5 Capacitive measurements

Until the first attempt of integration of microfluidics with MEMS, it was not known that a glass substrate with such quantity of metal deposited on top was not easily sealed against PDMS when using the regular technique in the plasma cleaner chamber. For that reason, the first two dies revealed a poor adhesion of PDMS to the substrate where the MEMS were patterned, even after detaching the PDMS structure and repeating the sealing. In fact, during the detachment, some cantilevers got damaged, making it impossible to measure anything with them. From these chips, only one pair of microchannels could be used but only for some minutes because the “repeated” sealing was fragile and the liquid that was flowing started leaking. Nevertheless, it was possible to determine the noise level of the measurement in air and water and it was compared the signal in the presence of a stationary liquid and that when flowing it.

Then, it became clear that it was necessary to try the stamping technique to improve the efficiency of the sealing. After various tests on glass substrates, this technique was implemented in the structures to be measured. The first attempt failed because some PDMS entered inside the channel right after placing the PDMS structure on top of the chip which resulted in permanent damage of the cantilevers. After optimizing the technique in order to reduce the thickness of spin coated PDMS for stamping, it was implemented again the same sealing technique. Although the sealing was completed successfully, this die must have suffered an electrical discharge due to statics which made the beams collapse and get stuck to the substrate.

The following die to be processed did not reach the integration phase. While the die was immersed in Al etchant, the pads for wire bonding got destroyed. Possibly the etching process for patterning of the sacrificial layer did not reach completely the end point and the TiW of the pads that was deposited afterwards suffered lift-off during this last procedure.

Finally, the last die resisted until the end of the integration process and a biological assay was started. However, during the step of 24h incubation, a leak was detected but the liquid inside the channel escaped causing stiction. Moreover, during handling of micropipette tips and metallic plug for microfluidics interface, a lot of connections made through wire bonding got damaged, so the assay was stopped in this phase.

Length of the cantilever		Average C_P (fF)	C_P noise level (fF)	Average R_P (M Ω)	R_P noise level (M Ω)
80 μm	A	-9.26	0.03	9.2	0.3
	B	25.26	0.05	-6.6	0.3
100 μm	A	-8.72	0.04	9.1	0.5
	B	24.72	0.04	-9.2	0.5
120 μm	A	-3.62	0.04	11.2	0.8
	B	28.30	0.05	-10.9	0.8
<i>Average</i>		-	0.04	-	0.5

Table 4.6: Average measurements in air and corresponding noise levels when the cantilevers are at equilibrium. The noise is calculated as the standard deviation.

In the end, from the six dies that were fabricated, only two ended up being useful after integration with microfluidics. Although it was not possible to run a complete biological experiment, it was possible to validate the concept of integration of both technologies under study.

By simply acquiring the measurements of capacitance and resistance with the cantilevers in equilibrium, it is possible to determine the noise level in the specific medium involving the structures. In Table 4.6 it is listed the noise level and average measure for each cantilever. In this design there is a pair of channels with an equal sequence of cantilevers, this is why there are two rows of results per length of cantilever. For this acquisition, it was defined a long measurement time and no sample averaging. The frequency of the AC component with amplitude of 1 V_{PP} was set as 1.1 MHz and no DC bias voltage was applied.

For the capacitance it is registered a noise level in the dozens of attoFarad while for resistance measurements the noise reaches hundreds of k Ω . This is considered as high sensitivity since a change of capacity of 0.04 fF corresponds to a deflection of 0.8 nm if calculated by:

$$\Delta z = g \left(\frac{1}{1 + \frac{g \Delta C}{\epsilon_0 w L}} - 1 \right) \quad (4.6)$$

Such deflection is lower than the reported values of cantilever deflection induced by DNA molecules (1 – 10 nm). A curious feature of this device is related with the negative values that appear intercalated with positive ones. Systematically, the cantilevers in the first channel return negative capacitances, while the ones from the second channel return positive ones due to the symmetrical design that was implemented between each pair of channels. According to the equation for the capacitance between two parallel electrodes (equation 2.39), it would be expected that with increasing length, the capacitance would increase linearly. However, the opposite is observed. A possible explanation for such trend may be based on the residual compressive stress of these cantilevers. Because of the resultant upwards natural bending of the cantilevers, the electrodes are not parallel and in fact, the angle defined between their planes increases with the length and the position in the beam, so a non-linear regime with the opposite trend takes place over the linear model for the parallel plates. The only trend that is respected

by these devices is the relation between capacitance and resistance: if the capacitance increases, it means that the electrodes are closer and the resistance decreases and vice-versa.

During such procedure, the light of the microscope was turned on twice, near the end of the measurement. The period of time for which the light was on, is detectable by the cantilever because a-Si:H is sensitive to light given its semiconductor properties. The plot in Figure 4.21 shows these two events both in capacitance and resistance signals. The phenomenon that occurs in this case is characterized by an excitation of an electron from the valence band of the material, promoting its shift towards the conduction band. The presence of electrons in the conduction band is responsible for the registered decrease in resistance and increase in capacitance.

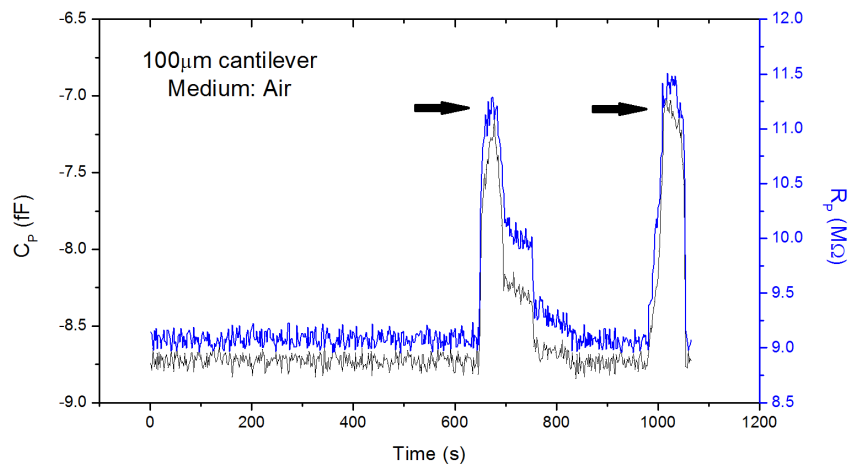


Figure 4.21: Plot of capacitance and resistance for each instant of time. The results were obtained in air by measuring a cantilever with 100 μm length. The black arrows are pointing the instants when the light of the microscope was turned on.

When the medium is changed to Milli-Q water, the capacitance must increase because the relative permittivity of the water, ϵ_r , corresponds to roughly 80, at room temperature. For this experiment, it was performed a new open and short calibration due to some complications with microfluidics interface, meaning that the absolute values in air cannot be compared with the ones in water. Nevertheless, it was examined the standard deviation of the measurements, just like it was done for the measurements in air. The noise level of capacitance in water is in average 0.04 fF just like in air. Nonetheless, the noise level of resistance decreased to an average of 0.2 MΩ which is probably related with the increase in conductivity between electrodes.

An additional experiment was done in which the response of the sensor in the presence of a flowing liquid was evaluated. The plot on Figure 4.22 shows the transition from a stationary state to flow and to the stationary state again for a cantilever of 120 μm length. The channel was previously filled with water and 97 s after starting the measurement, the flow of water was restarted at 5 $\mu\text{L}/\text{min}$ again. Then, 255 s after the initial instant, the flow was stopped. In the plot, it is clearly visible the transition between both states, not only because it is detected a sudden increase/decrease in the signals, but also because when the water is flowing, an oscillatory behaviour is obtained. The first evidence results from the sudden

pressure that the flow applies on the stressed cantilever, bending it downwards. The second one is originated by the stepper motor incorporated in the syringe pump. In fact, only the longer cantilevers ($120\ \mu\text{m}$) are able to sense such oscillation in the flow, given that longer beams are more sensitive. It is also interesting to refer the presence of a drift in the measurements from channel A while the other remains constant, except in the end when the flow is stopped. This drift is no more than a mechanical transient. The difference between both channels suggest that they were in different states of equilibrium: B was in equilibrium in the beginning of the experiment while A was still moving towards that state. Such difference is not beneficial when trying to implement differential measurements. However, the principle of operation of the device in water is validated with these few experiments.

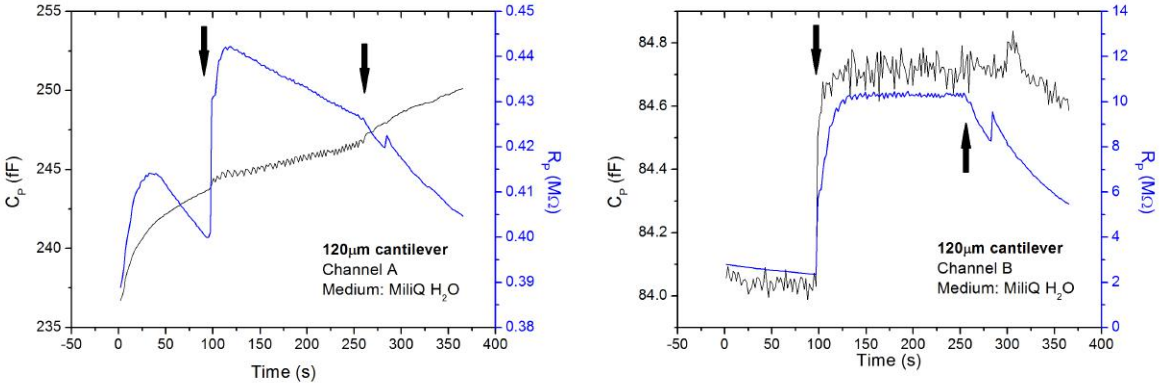


Figure 4.22: Plots of capacitance and resistance for each instant of time. The results were obtained in water by measuring two cantilevers with $120\ \mu\text{m}$ length in two different channels. The black arrows are pointing the instants when the flow was turned on and off.

Chapter 5

Conclusions

As first achievement, the present work succeeded in quantifying the effects of stiction using the standard protocol at INESC-MN and a simpler one. The standard protocol using n-hexane for reduction in surface tension has an associated work of adhesion of $77 \pm 8 \mu\text{J}\cdot\text{m}^{-2}$, much lower than that of the simple process that finishes using solely DI water ($361 \pm 15 \mu\text{J}\cdot\text{m}^{-2}$). This is the evidence that in fact the release protocol currently used is beneficial for the structure being released. Also, with this tool, it became possible to predict if a cantilever with certain dimensions and material properties is presumed to suffer stiction.

From the biological experiences involving the formation of ssDNA SAM's, an extended study of the effects of the variation of certain conditions on the density of immobilized probes was achieved by implementation of chemiluminescence techniques. It was desired a high selectivity of probes with the Au surface in order to ensure that a differential stress would be originated in the cantilever, and also an appropriate density of probes that needs to establish the compromise between the intermolecular electrostatic repulsion and simultaneously the coverage of a maximum surface. For that reason, conditions and parameters such as flow rates, duration of flow, incubation, blocking agent and liquid medium were optimized in order to achieve a robust protocol. In the end, it was attained a good understanding on the processes involved in SAM's formation and the objectives of such experiences were achieved. It was verified the critical effect of incubation as way of increasing the density of probes and it was established a duration of incubation of 24h as a compromise. It was also observed that a solution of 1M TE NaCl can in fact help the immobilization process since the high concentration of salt shields neighboring molecules from electrostatic repulsions at a certain extent. By comparing three blocking agents, it was concluded that BSA-4% shows the best performance because it is more selective than PA and has more affinity to the desired surfaces. In the end, a strong signal is obtained on top of Au surfaces with a low background arriving from the PDMS/glass surfaces predominantly. However, the selectivity and the ratio between the specific signal and the background one seem to be high enough.

Also a protocol for hybridization was established, this one without long hours of incubation, but the processes could not be fully-tuned and tested and for that reason, only a specific set of conditions and parameters were found to work. Nevertheless, the selectivity of the probes towards complementar

targets showed to be very high, attaining results with no specific signal when flowing non-complemetar targets.

The biological assays also allowed to find out that with these particular molecules, fluorescence cannot be used for imaging because the proximity of the fluorophores to the Au thin films induces quenching. If one tries to reproduce the optimized assay of chemiluminescence but with a fluorophore as label, after washing the excess probe that did not immobilize, the signal decreases to the same values of an empty microchannel.

In terms of integration of MEMS with the microfluidics, some non expected issues occurred, resulting sometimes in damaging of the cantilevers. It was noticed that it was necessary to use a stamping technique for sealing instead of the regular oxidative treatment in the plasma cleaner because the quantity of metal deposited on glass did not allow the formation of strong bonds with the PDMS. Even the stamping technique with "fresh" PDMS needed to be tested carefully because if the spin coated layer of this material was too thick, then the PDMS would enter the microchannels and damage the cantilevers. Although the efficiency and uniformity of this technique proved to be higher, the strength of the seal is lower. The wire bonding used to connect the pads in the glass substrate to the pads in the PCB although being functional, it is not very practical and robust since a lot of devices got their wires broken while the tubes and micropipette tips were being attached to the inlets/outlets.

Finally, it was possible to define a working frequency for the capacitive measurements by measuring the resonance spectrum of the various cantilevers. It needed to be such a frequency that do not cause resonance of the cantilever, so it was chosen 1.1 MHz. Given the quantity of problems that arised during integration of devices, few structures could in fact be used for measuring the capacitance and resistance of the cantilevers. Nonetheless, it was possible to define the noise level of capacitance and resistance in air and in water. The capacitance noise was found to be 0.04 fF for both mediums which corresponds to a deflection of approximately 0.8 nm for the designated cantilevers. The resistance noise in air was determined as 0.5 M Ω and, when the cantilever is immersed in water, the same parameter decreases to 0.2 M Ω . For this reason and because the sensors appeared to be responsive to changes in light intensity and flow, this system was considered very sensitive and appropriate for biosensing in liquid mediums.

For future work, it is suggested a complementary study on immobilization and hybridization of DNA on gold. Some experiments using different buffers and solutions can be advantageous in order to improve not only the immobilization yield but also the hybridization one. A study of the behaviour of such molecules in the presence of the same solution with varied pH values may be also interesting. The comprehension of the mechanisms that lead Au thin films to induce quenching of the fluorescence signal could be very relevant since that way it would be possible to tune the various conditions and parameters of the film and molecules in order to prevent/reduce such undesired process. If fluorescence could be used, a simpler protocol for biological assays is used which is also beneficial for the immobilized probes. A final set of experiments regarding regeneration of probes would allow to reuse the same microchannel multiple times. This is also important for the detection with MEMS since less structures would need to be fabricated and the reproducibility of each sensor would increase. In the literature, some solutions containing urea are known to regenerate the probes at some extent, so this could be a starting point.

The reduction of film residual stress would decrease the upwards bending of the cantilevers that is observed when they are in equilibrium after release. Such improvement would allow a better and more efficient comparison with the theoretical models and a better control of the structures.

If instead of wire bonding, it was used a customized connector between the MEMS chip and the PCB, a more robust connection can be established and the probability of being able to run an entire biological assay until the end, would increase. If an alternative technique for improvement of sealing could be implemented, a stronger bond between the MEMS chip and the PDMS would be achieved and no leak issues would happen.

To sum up, the device developed throughout this project proved that integration of MEMS with microfluidics is possible even for biosensing. Although it was not possible to perform a complete biological assay due to logistic problems, some preliminary measurements allowed the validation of the concept.

Bibliography

- [1] S. B. Patil et al. Decoupling competing surface binding kinetics and reconfiguration of receptor footprint for ultrasensitive stress assays. *Nature Nanotechnology*, 10:899–907, Aug. 2015.
- [2] M. Alvarez and L. M. Lechuga. Microcantilever-based platforms as biosensing tools. *The Analyst*, 135:827–836, Jan. 2010.
- [3] M. Calleja, P. M. Kosaka, A. S. Paulo, and J. Tamayo. Challenges for nanomechanical sensors in biological detection. *Nanoscale*, 4:4925–4938, June 2012.
- [4] J. L. Arlett, E. B. Myers, and M. L. Roukes. Comparative advantages of mechanical biosensors. *Nature Nanotechnology*, 6:203–215, Mar. 2011.
- [5] J. Zhang et al. Rapid and label-free nanomechanical detection of biomarker transcripts in human RNA. *Nature Nanotechnology*, 1:214–220, Nov. 2006.
- [6] P. Alpuim, V. Chu, and J. P. Conde. Amorphous and microcrystalline silicon films grown at low temperatures by radio-frequency and hot-wire chemical vapor deposition. *Journal of Applied Physics*, 86(7):3812–3821, Oct. 1999.
- [7] M. Boucinha, P. Brogueira, V. Chu, and J. P. Conde. Amorphous silicon air-gap resonators on large-area substrates. *Applied Physics Letters*, 77(6):907–909, 2000.
- [8] J. Mouro, A. Gualdino, V. Chu, and J. P. Conde. Tunable properties of hydrogenated amorphous / nanocrystalline silicon thin-films for enhanced MEMS resonators performance. *Journal of Microelectromechanical Systems*, 23(3):600–609, June 2014.
- [9] A. Gualdino, V. Chu, and J. P. Conde. Pressure effects on the dynamic properties of hydrogenated amorphous silicon disk resonators. *Journal of Micromechanics and Microengineering*, 22(8):85026, Aug. 2012.
- [10] J. P. Conde, J. Gaspar, and V. Chu. Low-temperature thin-film silicon MEMS. *Thin Solid Films*, 427(1-2):181–186, Mar. 2003.
- [11] J. Gaspar, V. Chu, and J. P. Conde. Electrostatic actuation of thin-film microelectromechanical structures. *Journal of Applied Physics*, 93(12):10018–10029, Mar. 2003.

- [12] A. Gualdino, V. Chu, and J. P. Conde. Study of the out-of-plane vibrational modes in thin-film amorphous silicon micromechanical disk resonators. *Journal of Applied Physics*, 113(17):174904, Apr. 2013.
- [13] Y.-P. Zhao, L. S. Wang, and T. X. Yu. Mechanics of adhesion in MEMS - a review. *Journal of Adhesion Science and Technology*, 17(4):519–546, 2003.
- [14] E. E. Parker, W. R. Ashurst, C. Carraro, and R. Maboudian. Adhesion characteristics of MEMS in microfluidic environments. *Journal of microelectromechanical systems*, 14(5):947–953, Oct. 2005.
- [15] R. Maboudian and C. Carraro. Surface chemistry and tribology of MEMS. *Annual Review of Physical Chemistry*, 55:35–54, Feb. 2004.
- [16] B. Bhushan. Adhesion and stiction: mechanisms, measurement techniques, and methods for reduction. *Journal of Vacuum Science and Technology B*, 21(6):2262–2296, Nov. 2003.
- [17] L. Huang et al. A system based on capacitive interfacing of CMOS with post-processed thin-film MEMS resonators employing synchronous readout for parasitic nulling. *Journal of Solid-State Circuits*, 50(4):1002–1015, Apr. 2015.
- [18] J. Gaspar, V. Chu, and J. P. Conde. Electrostatically actuated thin-film amorphous silicon micro-bridge resonators. *Applied Physics Letters*, 97(9):94501, Apr. 2005.
- [19] S. B. Patil, A. Guedes, P. P. Freitas, S. Cardoso, V. Chu, and J. P. Conde. On-chip magnetoresistive detection of resonance in microcantilevers. *Applied Physics Letters*, 95(023502):1–3, July 2009.
- [20] M. Li, H. X. Tang, and M. L. Roukes. Ultra-sensitive NEMS-based cantilevers for sensing, scanned probe and very high-frequency applications. *Nature Nanotechnology*, 2(2):114–120, Feb. 2007.
- [21] A. Gupta, D. Akin, and R. Bashir. Single virus particle mass detection using microresonators with nanoscale thickness. *Applied Physics Letters*, 84(11):1976–1978, Mar. 2004.
- [22] J. P. Conde, N. Madaboosi, R. Soares, J. Fernandes, P. Novo, G. Moulas, and V. Chu. Lab-on-chip systems for integrated bioanalyses. *Essays in Biochemistry*, 60:121–131, June 2016.
- [23] D. C. Martins, V. Chu, D. Prazeres, and J. P. Conde. Electrical detection of DNA immobilization and hybridization by streaming current measurements in microchannels. *Applied Physics Letters*, 99(18):183702, Nov. 2011.
- [24] M. Boyd-Moss, S. Baratchi, M. D. Venere, and K. Khoshmanesh. Self-contained microfluidic systems: a review. *Lab on a Chip*, 16:3177–3192, July 2016.
- [25] N. Noeth, S. Keller, and A. Boisen. Integrated cantilever-based flow sensors with tunable sensitivity for in-line monitoring of flow fluctuations in microfluidic systems. *Sensors*, 14:229–244, Jan. 2014.
- [26] M. Yue, J. C. Stachowiak, H. Lin, R. Datar, R. Cote, and A. Majumdar. Label-free protein recognition two-dimensional array using nanomechanical sensors. *Nano Letters*, 8(2):520–524, Jan. 2008.

- [27] M. G. von Muhlen, N. D. Brault, S. M. Knudsen, S. Jiang, and S. R. Manalis. Label-free biomarker sensing in undiluted serum with suspended microchannel resonators. *Analytical Chemistry*, 82(5): 1905–1910, Mar. 2010.
- [28] H. Lang, M. Hegner, and C. Gerber. Nanomechanical cantilever array sensors. In *Handbook of nanotechnology*, chapter 15, pages 427–452. Springer, New York, 3rd edition, 2010.
- [29] M. F. Hagan, A. Majumdar, and A. K. Chakraborty. Nanomechanical forces generated by surface grafted DNA. *Journal of Physical Chemistry B*, 106(39):10163–10173, Sept. 2002.
- [30] A. Sassolas, B. D. Leca-Bouvier, and L. J. Blum. DNA biosensors and microarrays. *Chemical Reviews*, 108(1):109–139, 2008.
- [31] P. M. Kosaka, J. Tamayo, J. J. Ruz, S. Puertas, E. Polo, V. Grazu, J. de la Fuente, and M. Calleja. Tackling reproducibility in microcantilever biosensors: a statistical approach for sensitive and specific end-point detection of immunoreactions. *Analyst*, 138(3):863–872, Feb. 2013.
- [32] J. Fritz. Cantilever biosensors. *The Analyst*, 133:855–863, Apr. 2008.
- [33] R. Shuttleworth. The surface tension of solids. *Proceedings of the Physical Society*, A63(5):444–457, May 1950.
- [34] G. G. Stoney. The tension of metallic films deposited by electrolysis. *Proceedings of the Royal Society of London*, A82(553):172–175, May 1909.
- [35] A. Boisen, S. Dohn, S. S. Keller, S. Schmid, and M. Tenje. Cantilever-like micromechanical sensors. *Reports on Progress in Physics*, 74:36101–36131, Feb. 2011.
- [36] W. C. Young and R. G. Budynas. *Roark's formulas for stress and strain*, chapter 8, pages 125–266. McGraw-Hill, New York, 7th edition, 2002.
- [37] M. Liangruksa. Effect of surface stress on micromechanical cantilevers for sensing applications. Master thesis, Virginia Polytechnic Institute and State University, Blacksburg, Virginia, July 2008.
- [38] K. L. Ekinici. Electromechanical transducers at the nanoscale: actuation and sensing of motion in nanoelectromechanical systems (NEMS). *Small*, 1(8-9):786–797, Aug. 2005.
- [39] S. M. Heinrich and I. Dufour. Fundamental theory of resonant MEMS devices. In *Resonant MEMS: fundamentals, implementation, and application*, chapter 1, pages 3–28. Wiley, 1st edition, Apr. 2015.
- [40] M. Bao. *Analysis and design principles of MEMS devices*. Elsevier B. V., Amsterdam, 1st edition, 2005.
- [41] S. Schmid, L. G. Villanueva, and M. L. Roukes. *Fundamentals of nanomechanical resonators*, chapter 1-4, pages 1–148. Springer, Switzerland, 2016.

- [42] M. Lalanne, P. Berthier, and J. D. Hagopian. *Mechanical vibrations for engineers*, chapter 1, pages 1–36. John Wiley and Sons, New York, 1984.
- [43] K. M. Goeders, J. S. Colton, and L. A. Bottomley. Microcantilevers: sensing chemical interactions via mechanical motion. *Chemical Reviews*, 108:522–542, Mar. 2008.
- [44] M. I. Younis. *MEMS linear and nonlinear statics and dynamics*, chapter 1-4, pages 1–154. Springer, New York, 2011.
- [45] B. Bahreyni. *Fabrication and design of resonant microdevices*. Series 3. William Andrew, New York, 2008.
- [46] R. Marathe. *Active sensing in silicon-based MEMS resonators*. PhD thesis, Massachusetts Institute of Technology, June 2015.
- [47] G. J. O'Brien, D. J. Monk, and L. Lin. MEMS cantilever beam electrostatic pull-in model. In *Design, characterization, and packaging for MEMS and microelectronics II*, volume 4593, pages 1–4, Nov. 2001.
- [48] C. H. Mastrangelo and C. H. Hsu. Mechanical stability and adhesion of microstructures under capillary forces - part I: basic theory. *Journal of Microelectromechanical systems*, 2(1):33–43, Mar. 1993.
- [49] C. H. Mastrangelo and C. H. Hsu. Mechanical stability and adhesion of microstructures under capillary forces - part II: experiments. *Journal of Microelectromechanical systems*, 2(1):44–55, Mar. 1993.
- [50] M. R. Houston, R. T. Howe, and R. Maboudian. Effect of hydrogen termination on the work of adhesion between rough polycrystalline silicon surfaces. *Journal of Applied Physics*, 81(8):3474–3483, Apr. 1997.
- [51] P. Tabeling. *Introduction to microfluidics*. Oxford University Press, Oxford, Nov. 2005.
- [52] B. E. Rapp. *Microfluidics: modeling, mechanics, and mathematics*, chapter 9-24, pages 241–494. Micro and nano technologies. William Andrew - Elsevier, Oxford, 2017.
- [53] R. Pedersen, A. N. Marchi, J. Majikes, J. A. Nash, N. A. Estrich, D. S. Courson, C. K. Hall, S. L. Craig, and T. H. LaBean. *Handbook of nanomaterials properties*, chapter 34, pages 1125–1157. Springer, Berlin, 1st edition, 2014.
- [54] J. Watson, T. Baker, S. Bell, A. Gann, M. Levine, and R. Losick. *Molecular biology of the gene*, chapter 6, pages 1–33. Cold Spring Harbor Laboratory Press, New York, 5th edition, 2004.
- [55] T. F. Scientific. Fluorescence fundamentals, accessed on 29th Jun 2017. <https://www.thermofisher.com/pt/en/home/references/molecular-probes-the-handbook/introduction-to-fluorescence-techniques.html>.

- [56] C. Caneira. Bead-based microfluidic system for DNA/RNA detection. Master thesis, Instituto Superior Técnico, Lisboa, Nov. 2015.
- [57] T. F. Scientific. Chemiluminescent western blotting, accessed on 29th Jun 2017. <https://www.thermofisher.com/pt/en/home/life-science/protein-biology/protein-biology-learning-center/protein-biology-resource-library/pierce-protein-methods/chemiluminescent-western-blotting.html>.
- [58] A. W. Peterson, R. J. Heaton, and R. M. Georgiadis. The effect of surface probe density on DNA hybridization. *Nucleic Acids Research*, 29(24):5163–5168, Oct. 2001.

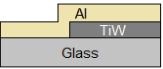
Appendix A

Fabrication runsheets

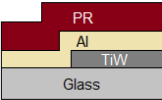
The various runsheets for each step of the generic process that was implemented can be found in the next pages. The runsheets are divided in:

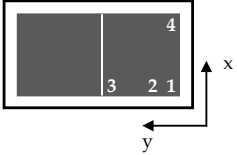
- Film deposition and patterning
- Hard mask for microfluidics
- SU-8 mold
- PDMS microchannels fabrication

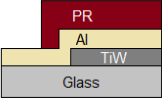
8.	Resist Strip	Date: 06/03/2017
<p>Equipment: Wet Bench Solution: Acetone + Fujifilm Microstrip 3001 Temperature: 65 °C Agitation: Manual</p> 		
<p>Procedure: Wash the sample to remove the photoresist, using plenty of acetone. Then, place it in microstrip for 30 min. Finally, wash with DI water, IPA, DI water again and blow dry.</p>		

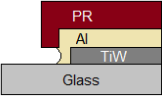
9.	Al sacrificial layer deposition	Date: 06/03/2017																
<p>Equipment: Nordiko 7000 (Magnetron Sputtering) Recipe: Al 5000A 2kW (run 2x)</p> 																		
<p>Layer thickness: 1000 nm Deposition rate: 3,85 nm/s Duration: 4 min 18 sec</p>																		
<p>Procedure:</p> <table border="0"> <tr> <td>1 – Mod4 Func3 – deposition of 500 nm Al at 2kW;</td> <td>Parameters:</td> <td>Power: 2 kW</td> <td>Ar flow: 50 sccm</td> </tr> <tr> <td>2 – Run again the same sequence (Al 5000A 2kW);</td> <td>Voltage: 400 V</td> <td>N₂ flow: 0 sccm</td> <td></td> </tr> <tr> <td>3 – Mod4 Func3 – deposition of 500 nm Al at 2kW;</td> <td>Current: 5 A</td> <td>Pressure: 3 mTorr</td> <td></td> </tr> </table>			1 – Mod4 Func3 – deposition of 500 nm Al at 2kW;	Parameters:	Power: 2 kW	Ar flow: 50 sccm	2 – Run again the same sequence (Al 5000A 2kW);	Voltage: 400 V	N ₂ flow: 0 sccm		3 – Mod4 Func3 – deposition of 500 nm Al at 2kW;	Current: 5 A	Pressure: 3 mTorr					
1 – Mod4 Func3 – deposition of 500 nm Al at 2kW;	Parameters:	Power: 2 kW	Ar flow: 50 sccm															
2 – Run again the same sequence (Al 5000A 2kW);	Voltage: 400 V	N ₂ flow: 0 sccm																
3 – Mod4 Func3 – deposition of 500 nm Al at 2kW;	Current: 5 A	Pressure: 3 mTorr																
<p>Profilometer (Al thickness)</p> <table border="0"> <tr> <td>1st sample:</td> <td>_____ Å,</td> <td>_____ Å,</td> <td>_____ Å</td> </tr> <tr> <td>2nd sample:</td> <td>_____ Å,</td> <td>_____ Å,</td> <td>_____ Å</td> </tr> <tr> <td>3rd sample:</td> <td>_____ Å,</td> <td>_____ Å,</td> <td>_____ Å</td> </tr> <tr> <td>average:</td> <td>_____ ± _____ Å</td> <td></td> <td></td> </tr> </table>			1 st sample:	_____ Å,	_____ Å,	_____ Å	2 nd sample:	_____ Å,	_____ Å,	_____ Å	3 rd sample:	_____ Å,	_____ Å,	_____ Å	average:	_____ ± _____ Å		
1 st sample:	_____ Å,	_____ Å,	_____ Å															
2 nd sample:	_____ Å,	_____ Å,	_____ Å															
3 rd sample:	_____ Å,	_____ Å,	_____ Å															
average:	_____ ± _____ Å																	

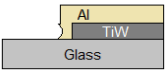
10.	Vapor Prime	Date: 06/03/2017
<p>Equipment: HDMS Oven</p> <p>Procedure:</p> <ol style="list-style-type: none"> 1 – Wafer dehydration: vacuum (10 Torr, 2 min); N₂ inlet (760 Torr, 3 min); heating (130°C) 2 – HDMS priming: vacuum (1 Torr, 3 min); HDMS (6 Torr, 5 min) 3 – HDMS exhaustion: vacuum (4 Torr, 1 min); N₂ inlet (500 Torr, 2 min); vacuum (4 Torr, 2 min) 4 – Pressure equalization: N₂ inlet (3 min) 		

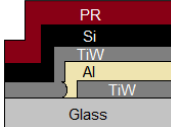
11.	Photoresist Spin Coating	Date: 06/03/2017
<p>Equipment: SVG Track Photoresist: JSR Micro PFR 7790G-27cP (Positive Photoresist) Layer thickness: 1.5 µm Coater Track Programs: Spinner Program: 6; Oven Program: 2</p> 		
<p>Procedure:</p> <ol style="list-style-type: none"> 1 – PR disposal: spinning (800 rpm); acceleration (10 krpm/s); duration (5 s) 2 – Spin (slow): spinning (800 rpm); acceleration (10 krpm/s); duration (5 s) 3 – Spin (fast): spinning (2800 rpm); acceleration (50 krpm/s); duration (40 s) 4 – Spin: spinning (1500 rpm); acceleration (50 krpm/s); duration (10 s) 5 – Hard bake: temperature (85 °C); duration (60 s) 		

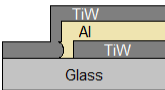
12.	Laser Exposure: Al sacrificial layer patterning	Date: 06/03/2017
<p>Equipment: DWL AUTOCAD Mask: final_structure_version1.dwg DWL File: CANTcapL2 Layer: Level 2 – Al sacrificial layer Map: CANTCAP (2 dies) Die dimensions: 15x19 mm</p> 		
<p>Focus: 35 Energy: 60 Exposure time: 22 min/substrate (66 min total)</p>		
<p>Note: Mask converted to do etching!</p> <p style="text-align: center;">MASK IS NOT SYMMETRIC!!!!</p>		
<p>1. Bottom-left alignment marks coordinates: (90;270) (225; 270) um 2. Distance to the next alignment marks (y): 6110 um 3. Distance to the last alignment marks (y): 18330 um 4. Distance to the other set of alignment marks (x): 14685 um</p>		

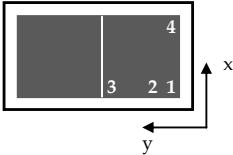
13.	Photoresist Development	Date: 06/03/2017
<p>Equipment: SVG Track Developer: JSR Micro TMA238 WA Developer Track Programs: Oven Program: 6; Spinner Program: 2</p> 		
<p>Procedure:</p> <ol style="list-style-type: none"> 1 – Post-exposure bake: temperature (110 °C); duration (60 s) 2 – Cool down: duration (30 s) 3 – Rinse: spinning (500 rpm); acceleration (10 krpm/s); duration (5 s) 4 – Spray developer: spinning (500 rpm); acceleration (10 krpm/s); duration (5 s) 5 – Development: spinning (0 rpm); acceleration (0 krpm/s); duration (60 s) 6 – Rinse: spinning (500 rpm); acceleration (5 krpm/s); duration (15 s) 7 – Spin dry: spinning (2000 rpm); acceleration (10 krpm/s); duration (30 s) 		

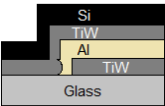
14.	Wet etch of Al sacrificial layer	Date: 07/03/2017
<p>Equipment: Wet Bench Solution: Gravure Aluminium Etchant Micropur MOS, Technic, France (LOT 017217)</p> 		
<p>Temperature: Ambient temperature Sonication: Manual agitation Etch Depth: 1µm Duration: 12 min 30 sec (+ 2 min overetch) Etch Rate: 80 nm/min</p>		
<p>Note: Exchange the microstrip near the end of the liftoff for a cleaner result. You may reuse this fresher microstrip if few particles are suspended on it. Do <u>not</u> use ultrasounds since Si may start peeling off.</p>		

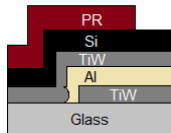
15. Resist Strip	Date: 07/03/2017
<p>Equipment: Wet Bench Solution: Acetone + Fujifilm Microstrip 3001 Temperature: 65 °C Agitation: Manual</p>	
	
<p>Procedure: Wash the sample to remove the photoresist, using plenty of acetone. Then, place it in microstrip for 30 min. Finally, wash with DI water, IPA, DI water again and blow dry.</p>	

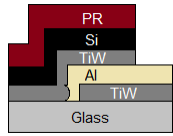
19. Photoresist Spin Coating	Date: 08/03/2017
<p>Equipment: SVG Track Photoresist: JSR Micro PFR 7790G-27cP (Positive Photoresist) Layer thickness: 1.5 µm Coater Track Programs: Spinner Program: 6; Oven Program: 2</p>	
	
<p>Procedure:</p> <ol style="list-style-type: none"> 1 – PR disposal: spinning (800 rpm); acceleration (10 krpm/s); duration (5 s) 2 – Spin (slow): spinning (800 rpm); acceleration (10 krpm/s); duration (5 s) 3 – Spin (fast): spinning (2800 rpm); acceleration (50 krpm/s); duration (40 s) 4 – Spin: spinning (1500 rpm); acceleration (50 krpm/s); duration (10 s) 5 – Hard bake: temperature (85 °C); duration (60 s) 	

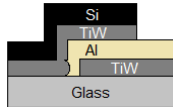
16. TiW layer deposition (top electrodes)	Date: 07/03/2017																
<p>Equipment: Nordiko 7000 (Magnetron Sputtering) Recipe: TiW1500A low stress</p>																	
																	
<p>Layer thickness: 150 nm Deposition rate: 0,5 nm/sec Duration: 5 min</p>																	
<p>Procedure:</p> <ol style="list-style-type: none"> 1 – Mod3 Func22 – deposition of 75 nm TiW at 0.3kW; 2 – Mod3 Func6 – cool down for 3 minutes; 3 – Mod3 Func22 – deposition of 75 nm TiW at 0.3kW; 																	
<table style="width: 100%; border: none;"> <tr> <td style="width: 25%;">Parameters:</td> <td style="width: 25%;">Power: 0.3 kW</td> <td style="width: 25%;">Ar flow: 50 sccm</td> <td style="width: 25%;"></td> </tr> <tr> <td></td> <td>Voltage: 330 V</td> <td>N₂ flow: 1 sccm</td> <td></td> </tr> <tr> <td></td> <td>Current: 0.94 A</td> <td>Pressure: 3 mTorr</td> <td></td> </tr> </table>		Parameters:	Power: 0.3 kW	Ar flow: 50 sccm			Voltage: 330 V	N ₂ flow: 1 sccm			Current: 0.94 A	Pressure: 3 mTorr					
Parameters:	Power: 0.3 kW	Ar flow: 50 sccm															
	Voltage: 330 V	N ₂ flow: 1 sccm															
	Current: 0.94 A	Pressure: 3 mTorr															
<p>Profilometer (TiW thickness)</p> <table style="width: 100%; border: none;"> <tr> <td style="width: 15%;">1st sample:</td> <td style="width: 15%;">_____ Å,</td> <td style="width: 15%;">_____ Å,</td> <td style="width: 15%;">_____ Å</td> </tr> <tr> <td>2nd sample:</td> <td>_____ Å,</td> <td>_____ Å,</td> <td>_____ Å</td> </tr> <tr> <td>3rd sample:</td> <td>_____ Å,</td> <td>_____ Å,</td> <td>_____ Å</td> </tr> <tr> <td>average:</td> <td colspan="3">_____ ± _____ Å</td> </tr> </table>		1 st sample:	_____ Å,	_____ Å,	_____ Å	2 nd sample:	_____ Å,	_____ Å,	_____ Å	3 rd sample:	_____ Å,	_____ Å,	_____ Å	average:	_____ ± _____ Å		
1 st sample:	_____ Å,	_____ Å,	_____ Å														
2 nd sample:	_____ Å,	_____ Å,	_____ Å														
3 rd sample:	_____ Å,	_____ Å,	_____ Å														
average:	_____ ± _____ Å																

20. Laser Exposure: Silicon layer patterning	Date: 08/03/2017
<p>Equipment: DWL AUTOCAD Mask: final_structure_version1.dwg DWL File: CANTcapL3 Layer: Level 3 – Si+TiW layer Map: CANTCAP (2 dies) Die dimensions: 15x19 mm</p>	
	
<p>Focus: 35 Energy: 60 Exposure time: 20 min/substrate (60 min total)</p>	
<p>1. Bottom-left alignment marks coordinates: (90;270) (225; 270) um 2. Distance to the next alignment marks (y): 6110 um 3. Distance to the last alignment marks (y): 18330 um 4. Distance to the other set of alignment marks (x): 14685 um</p>	
<p>Note: Mask converted to do etching!</p> <p>MASK IS NOT SYMMETRIC!!!!</p>	

17. n⁺ a-Si:H - Silicon layer deposition	Date: 07/03/2017																
<p>Equipment: Plasma-enhanced chemical vapor deposition (PECVD) Layer thickness: 1 µm Deposition rate: 21.7 nm/min</p>																	
																	
<p>Deposition conditions:</p> <table style="width: 100%; border: none;"> <tr> <td style="width: 15%;">RF Power: 15 W</td> <td style="width: 15%;">SiH₄ flow: 10 sccm</td> </tr> <tr> <td>Pressure: 0.5 Torr</td> <td>H₂ flow: 8 sccm</td> </tr> <tr> <td>Duration: 46 min</td> <td>PH₃ flow: 5 sccm</td> </tr> <tr> <td>Temperature: 175 °C</td> <td></td> </tr> </table>		RF Power: 15 W	SiH ₄ flow: 10 sccm	Pressure: 0.5 Torr	H ₂ flow: 8 sccm	Duration: 46 min	PH ₃ flow: 5 sccm	Temperature: 175 °C									
RF Power: 15 W	SiH ₄ flow: 10 sccm																
Pressure: 0.5 Torr	H ₂ flow: 8 sccm																
Duration: 46 min	PH ₃ flow: 5 sccm																
Temperature: 175 °C																	
<p>Profilometer (a-Si:H thickness)</p> <table style="width: 100%; border: none;"> <tr> <td style="width: 15%;">1st sample:</td> <td style="width: 15%;">_____ Å,</td> <td style="width: 15%;">_____ Å,</td> <td style="width: 15%;">_____ Å</td> </tr> <tr> <td>2nd sample:</td> <td>_____ Å,</td> <td>_____ Å,</td> <td>_____ Å</td> </tr> <tr> <td>3rd sample:</td> <td>_____ Å,</td> <td>_____ Å,</td> <td>_____ Å</td> </tr> <tr> <td>average:</td> <td colspan="3">_____ ± _____ Å</td> </tr> </table>		1 st sample:	_____ Å,	_____ Å,	_____ Å	2 nd sample:	_____ Å,	_____ Å,	_____ Å	3 rd sample:	_____ Å,	_____ Å,	_____ Å	average:	_____ ± _____ Å		
1 st sample:	_____ Å,	_____ Å,	_____ Å														
2 nd sample:	_____ Å,	_____ Å,	_____ Å														
3 rd sample:	_____ Å,	_____ Å,	_____ Å														
average:	_____ ± _____ Å																

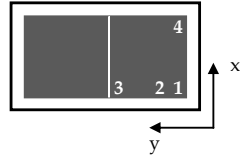
21. Photoresist Development	Date: 08/03/2017
<p>Equipment: SVG Track Developer: JSR Micro TMA238 WA Developer Track Programs: Oven Program: 6; Spinner Program: 2</p>	
	
<p>Procedure:</p> <ol style="list-style-type: none"> 1 – Post-exposure bake: temperature (110 °C); duration (60 s) 2 – Cool down: duration (30 s) 3 – Rinse: spinning (500 rpm); acceleration (10 krpm/s); duration (5 s) 4 – Spray developer: spinning (500 rpm); acceleration (10 krpm/s); duration (5 s) 5 – Development: spinning (0 rpm); acceleration (0 krpm/s); duration (60 s) 6 – Rinse: spinning (500 rpm); acceleration (5 krpm/s); duration (15 s) 7 – Spin dry: spinning (2000 rpm); acceleration (10 krpm/s); duration (30 s) 	

22.	RIE Patterning of the Si+TiW layer	Date: 08/03/2017												
<p>Equipment: LAM Research Rainbow Plasma Etcher Recipe: SF₆ + CHF₃ Etch Depth: 0.5 μm Duration: 350 s</p> <p>Parameters:</p> <table> <tr> <td>RF Power:</td> <td>200 W</td> <td>CHF₃ flow:</td> <td>50 sccm</td> </tr> <tr> <td>Pressure:</td> <td>100 mTorr</td> <td>SF₆ flow:</td> <td>50 sccm</td> </tr> <tr> <td>Electrode temp.:</td> <td>40 °C</td> <td></td> <td></td> </tr> </table>			RF Power:	200 W	CHF ₃ flow:	50 sccm	Pressure:	100 mTorr	SF ₆ flow:	50 sccm	Electrode temp.:	40 °C		
RF Power:	200 W	CHF ₃ flow:	50 sccm											
Pressure:	100 mTorr	SF ₆ flow:	50 sccm											
Electrode temp.:	40 °C													
														

23.	Resist Strip	Date: 08/03/2017
<p>Equipment: Wet Bench Solution: Acetone + Fujifilm Microstrip 3001 Temperature: 65 °C Agitation: Manual</p> <p>Procedure: Wash the sample to remove the photoresist, using plenty of acetone. Then, place it in microstrip for 30 min. Finally, wash with DI water, IPA, DI water again and blow dry.</p>		
		

24.	Vapor Prime	Date: 08/03/2017
<p>Equipment: HDMS Oven</p> <p>Procedure:</p> <ol style="list-style-type: none"> 1 – Wafer dehydration: vacuum (10 Torr, 2 min); N₂ inlet (760 Torr, 3 min); heating (130°C) 2 – HDMS priming: vacuum (1 Torr, 3 min); HDMS (6 Torr, 5 min) 3 – HDMS exhaustion: vacuum (4 Torr, 1 min); N₂ inlet (500 Torr, 2 min); vacuum (4 Torr, 2 min) 4 – Pressure equalization: N₂ inlet (3 min) 		

25.	Photoresist Spin Coating	Date: 08/03/2017
<p>Equipment: SVG Track Photoresist: JSR Micro PFR 7790G-27cP (Positive Photoresist) Layer thickness: 1.5 μm Coater Track Programs: Spinner Program: 6; Oven Program: 2</p> <p>Procedure:</p> <ol style="list-style-type: none"> 1 – PR disposal: spinning (800 rpm); acceleration (10 krpm/s); duration (5 s) 2 – Spin (slow): spinning (800 rpm); acceleration (10 krpm/s); duration (5 s) 3 – Spin (fast): spinning (2800 rpm); acceleration (50 krpm/s); duration (40 s) 4 – Spin: spinning (1500 rpm); acceleration (50 krpm/s); duration (10 s) 5 – Hard bake: temperature (85 °C); duration (60 s) 		

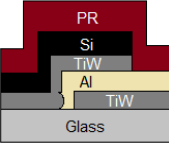
26.	Laser Exposure: TiW layer patterning (contact pads and ground plane)	Date: 08/03/2017
<p>Equipment: DWL AUTOCAD Mask: final_structure_version1.dwg DWL File: CANTcapL4 Layer: Level 4 – pads + groundplane Map: CANTCAP (2 dies) Die dimensions: 15x19 mm</p> <div style="display: flex; align-items: center;">  </div> <p>Focus: 35 Energy: 65 Exposure time: 20 min/substrate (60 min total)</p> <div style="border: 1px solid black; padding: 5px;"> <ol style="list-style-type: none"> 1. Bottom-left alignment marks coordinates: (90;420) (225; 420) μm 2. Distance to the next alignment marks (y): 6110 μm 3. Distance to the last alignment marks (y): 18330 μm 4. Distance to the other set of alignment marks (x): 14685 μm </div> <p>Note: Mask converted to do etching! MASK IS NOT SYMMETRIC!!!!</p> <p>Obs.: During the RIE of the bilayer Si+TiW, the alignment mark of the level 1 was erased, so this alignment is performed with the marks of the level 2 (Al – sacrificial layer).</p>		

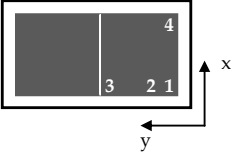
27.	Photoresist Development	Date: 08/03/2017
<p>Equipment: SVG Track Developer: JSR Micro TMA238 WA Developer Track Programs: Oven Program: 6; Spinner Program: 2</p> <p>Procedure:</p> <ol style="list-style-type: none"> 1 – Post-exposure bake: temperature (110 °C); duration (60 s) 2 – Cool down: duration (30 s) 3 – Rinse: spinning (500 rpm); acceleration (10 krpm/s); duration (5 s) 4 – Spray developer: spinning (500 rpm); acceleration (10 krpm/s); duration (5 s) 5 – Development: spinning (0 rpm); acceleration (0 krpm/s); duration (60 s) 6 – Rinse: spinning (500 rpm); acceleration (5 krpm/s); duration (15 s) 7 – Spin dry: spinning (2000 rpm); acceleration (10 krpm/s); duration (30 s) 		

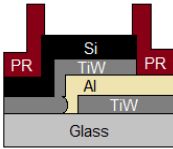
28.	TiW layer deposition (contact pads and ground plane)	Date: 09/03/2017																												
<p>Equipment: Nordiko 7000 (Magnetron Sputtering) Recipe: TiW1500A low stress</p> <p>Layer thickness: 150 nm Deposition rate: 0,5 nm/sec Duration: 5 min</p> <table> <tr> <td>Procedure:</td> <td></td> <td>Parameters:</td> <td></td> </tr> <tr> <td>1 – Mod3 Func22 – deposition of 75 nm TiW at 0.3kW;</td> <td></td> <td>Power:</td> <td>0.3 kW</td> </tr> <tr> <td>2 – Mod3 Func6 – cool down for 3 minutes;</td> <td></td> <td>Voltage:</td> <td>320 V</td> </tr> <tr> <td>3 – Mod3 Func22 – deposition of 75 nm TiW at 0.3kW;</td> <td></td> <td>Current:</td> <td>0.96 A</td> </tr> <tr> <td></td> <td></td> <td>Ar flow:</td> <td>50 sccm</td> </tr> <tr> <td></td> <td></td> <td>N₂ flow:</td> <td>1 sccm</td> </tr> <tr> <td></td> <td></td> <td>Pressure:</td> <td>3 mTorr</td> </tr> </table> <p>Profilometer (TiW thickness)</p> <p>1st sample: _____ Å, _____ Å, _____ Å 2nd sample: _____ Å, _____ Å, _____ Å 3rd sample: _____ Å, _____ Å, _____ Å average: _____ ± _____ Å</p>			Procedure:		Parameters:		1 – Mod3 Func22 – deposition of 75 nm TiW at 0.3kW;		Power:	0.3 kW	2 – Mod3 Func6 – cool down for 3 minutes;		Voltage:	320 V	3 – Mod3 Func22 – deposition of 75 nm TiW at 0.3kW;		Current:	0.96 A			Ar flow:	50 sccm			N ₂ flow:	1 sccm			Pressure:	3 mTorr
Procedure:		Parameters:																												
1 – Mod3 Func22 – deposition of 75 nm TiW at 0.3kW;		Power:	0.3 kW																											
2 – Mod3 Func6 – cool down for 3 minutes;		Voltage:	320 V																											
3 – Mod3 Func22 – deposition of 75 nm TiW at 0.3kW;		Current:	0.96 A																											
		Ar flow:	50 sccm																											
		N ₂ flow:	1 sccm																											
		Pressure:	3 mTorr																											

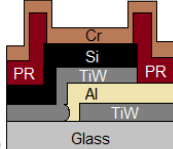
29.	Resist Strip / TiW Lift-off	Date: 09/03/2017
<p>Equipment: Wet Bench Solution: Fujifilm Microstrip 3001, LOT N4D13NAS</p> <p>Temperature: 65 °C Sonication: Intermittent Duration: Overnight</p> <p>Note: Exchange the microstrip near the end of the liftoff for a cleaner result. You may reuse this fresher microstrip if few particles are suspended on it. Do <u>not</u> use ultrasounds since Si may start peeling off.</p>		

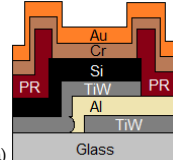
30.	Vapor Prime	Date: 10/03/2017
<p>Equipment: HDMS Oven</p> <p>Procedure:</p> <ol style="list-style-type: none"> 1 – Wafer dehydration: vacuum (10 Torr, 2 min); N₂ inlet (760 Torr, 3 min); heating (130°C) 2 – HDMS priming: vacuum (1 Torr, 3 min); HDMS (6 Torr, 5 min) 3 – HDMS exhaustion: vacuum (4 Torr, 1 min); N₂ inlet (500 Torr, 2 min); vacuum (4 Torr, 2 min) 4 – Pressure equalization: N₂ inlet (3 min) 		

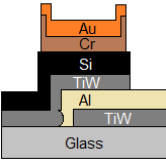
31.	Photoresist Spin Coating	Date: 10/03/2017
<p>Equipment: SVG Track Photoresist: JSR Micro PFR 7790G-27cP (Positive Photoresist) Layer thickness: 1.5 µm Coater Track Programs: Spinner Program: 6; Oven Program: 2</p>  <p>Procedure:</p> <ol style="list-style-type: none"> 1 – PR disposal: spinning (800 rpm); acceleration (10 krpm/s); duration (5 s) 2 – Spin (slow): spinning (800 rpm); acceleration (10 krpm/s); duration (5 s) 3 – Spin (fast): spinning (2800 rpm); acceleration (50 krpm/s); duration (40 s) 4 – Spin: spinning (1500 rpm); acceleration (50 krpm/s); duration (10 s) 5 – Hard bake: temperature (85 °C); duration (60 s) 		

32.	Laser Exposure: Chromium+Gold layer patterning	Date: 10/03/2017
<p>Equipment: DWL AUTOCAD Mask: final_structure_version1.dwg DWL File: CANTcapL5 Layer: Level 5 – Cr+Au layer Map: CANTCAP (2 dies) Die dimensions: 15x19 mm</p>  <p>Focus: 35 Energy: 65 Exposure time: 2 min/substrate (6 min total)</p> <p>Note: <u>Mask converted to do etching!</u></p> <p style="text-align: center;">MASK IS NOT SYMMETRIC!!!!</p>		
<ol style="list-style-type: none"> 1. Bottom-left alignment marks coordinates: (90;420) (225; 420) um 2. Distance to the next alignment marks (y): 6110 um 3. Distance to the last alignment marks (y): 18330 um 4. Distance to the other set of alignment marks (x): 14685 um 		

33.	Photoresist Development	Date: 10/03/2017
<p>Equipment: SVG Track Developer: JSR Micro TMA238 WA Developer Track Programs: Oven Program: 6; Spinner Program: 2</p>  <p>Procedure:</p> <ol style="list-style-type: none"> 1 – Post-exposure bake: temperature (110 °C); duration (60 s) 2 – Cool down: duration (30 s) 3 – Rinse: spinning (500 rpm); acceleration (10 krpm/s); duration (5 s) 4 – Spray developer: spinning (500 rpm); acceleration (10 krpm/s); duration (5 s) 5 – Development: spinning (0 rpm); acceleration (0 krpm/s); duration (60 s) 6 – Rinse: spinning (500 rpm); acceleration (5 krpm/s); duration (15 s) 7 – Spin dry: spinning (2000 rpm); acceleration (10 krpm/s); duration (30 s) 		

34.	Chromium layer deposition	Date: 20/03/2017					
<p>Equipment: SCM 450 Alcatel (Magnetron Sputtering) Layer thickness: 10 nm Deposition rate: 4 nm/min</p>  <p>Procedure:</p> <ol style="list-style-type: none"> 1 – Cleaning Cr target: With the shutter under the sample holder and the power ON (duration 5 min) 2 – Cr deposition: The shutter is removed so that the material can deposit on the sample (duration 2 min 30 sec) <p>Deposition conditions:</p> <table> <tr> <td>Base Pressure: 6,55 × 10⁻⁷ Torr</td> <td>Ar flow: 20 sccm</td> <td rowspan="2" style="border: 1px solid black; padding: 5px;">Station 4 + Target 1</td> </tr> <tr> <td>Dep. Pressure: 2,90 × 10⁻³ Torr</td> <td>DC power: 20 W</td> </tr> </table>			Base Pressure: 6,55 × 10 ⁻⁷ Torr	Ar flow: 20 sccm	Station 4 + Target 1	Dep. Pressure: 2,90 × 10 ⁻³ Torr	DC power: 20 W
Base Pressure: 6,55 × 10 ⁻⁷ Torr	Ar flow: 20 sccm	Station 4 + Target 1					
Dep. Pressure: 2,90 × 10 ⁻³ Torr	DC power: 20 W						

35.	Gold layer deposition	Date: 20/03/2017							
<p>Equipment: SCM 450 Alcatel (Magnetron Sputtering) Layer thickness: 50 nm Deposition rate: 5,6 nm/min</p>  <p>Procedure:</p> <ol style="list-style-type: none"> 1 – Cleaning Au target: With the shutter under the sample holder and the power ON (duration 3 min) 2 – Au deposition: The shutter is removed so that the material can deposit on the sample (duration 9 min) <p>Deposition conditions:</p> <table> <tr> <td>Base Pressure: 6,55 × 10⁻⁷ Torr</td> <td>DC power: 20 W</td> <td rowspan="3" style="border: 1px solid black; padding: 5px;">Station 4 + Target 3</td> </tr> <tr> <td>Dep. Pressure: 2,92 × 10⁻³ Torr</td> <td>Ar flow: 20 sccm</td> </tr> <tr> <td></td> <td>V(bias): 150 V</td> </tr> </table> <p>Profilometer (gold+chromium thickness): ____ Å, ____ Å, ____ Å. average: ____ ± ____ Å</p> <p>Note: The thermal expansion coefficient of gold (14 × 10⁻⁶ K⁻¹) is approximately the double of TiW's (6,5 × 10⁻⁶ K⁻¹) so the thickness of deposited gold must be near half the thickness of the top electrodes. This way it is prevented any additional stress due to thermal expansion.</p>			Base Pressure: 6,55 × 10 ⁻⁷ Torr	DC power: 20 W	Station 4 + Target 3	Dep. Pressure: 2,92 × 10 ⁻³ Torr	Ar flow: 20 sccm		V(bias): 150 V
Base Pressure: 6,55 × 10 ⁻⁷ Torr	DC power: 20 W	Station 4 + Target 3							
Dep. Pressure: 2,92 × 10 ⁻³ Torr	Ar flow: 20 sccm								
	V(bias): 150 V								

36.	Resist Strip / Cr+Au Lift-off	Date: 20/03/2017
<p>Equipment: Wet Bench Solution: Fujifilm Microstrip 3001, LOT N4D13NAS</p> <p>Temperature: 65 °C Sonication: Manual agitation Duration: 1h</p> <div style="text-align: center;">  </div> <p>Note: Exchange the microstrip near the end of the liftoff for a cleaner result. You may reuse this fresher microstrip if few particles are suspended on it. Do <u>not</u> use ultrasounds since Si may start peeling off.</p>		

37.	Photoresist Spin Coating	Date: 23/03/2017
<p>Equipment: SVG Track Photoresist: JSR Micro PFR 7790G-27cP (Positive Photoresist) Layer thickness: 1.5 µm Coater Track Programs: Spinner Program: 6; Oven Program: 2</p> <p>Procedure:</p> <ol style="list-style-type: none"> 1 – PR disposal: spinning (800 rpm); acceleration (10 krpm/s); duration (5 s) 2 – Spin (slow): spinning (800 rpm); acceleration (10 krpm/s); duration (5 s) 3 – Spin (fast): spinning (2800 rpm); acceleration (50 krpm/s); duration (40 s) 4 – Spin: spinning (1500 rpm); acceleration (50 krpm/s); duration (10 s) 5 – Hard bake: temperature (85 °C); duration (60 s) 		

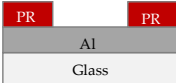
38.	Dicing – cut sample in individual dies	Date: 23/03/2017
<p>Equipment: Disco DAD 321 Dicing Saw Blade thickness: ~200 µm Blade speed: 30.000 rpm Cutting speed: 1 mm/s Cutting dimensions: Channel 1 = _____ mm; Channel 2 = _____ mm</p>		

Observations:

After TiW (Level 1) deposition, some marks were visible in one of the substrates. These marks were due to residues of water that were not properly dried. After RIE etching, these marks disappeared, not compromising the structures.

The lift-off of TiW (Level 4) from the groundplane didn't go as expected in some regions of the substrates. Possibly due to the ultrasounds or non-uniformities in the photoresist, the metal started to peel-off in undesired regions and weird patterns appeared. Only three cantilevers seem to be compromised due to these defects and incomplete lift-off.

Note: During gold deposition, if a strict control of thickness is desired, deposition must occur on stations 2 and 4 and never on the three of them at the same time. Otherwise, there will be contamination and the thickness and content cannot be properly controlled.

7.	Aluminium patterning using wet etch	Date: 09/09/2016
Equipment: Wet Bench Etchant: TechniEtch Al80 (UN 3265) Etch Depth: 100 nm Etch Rate: 50-100 nm/min Duration: 3 min (w/ overetch included)		
Note: Verify if the etching is complete. If it is not the case, do a little bit more overetch.		

8.	Resist Strip	Date: 09/09/2016
Equipment: Wet Bench Solution: Fujifilm Microstrip 3001, LOT N4D13NAS Temperature: 65 °C Sonication: Continuous Duration: 10 min		
Procedure: <ol style="list-style-type: none"> 1 – Fill a recipient with microstrip and place the sample inside it 2 – After 10 min, rinse with DI water 3 – Clean with IPA followed by DI water again 4 – Blow dry with compressed air 		
Note: Exchange the microstrip near the end for a cleaner result. You may reuse this fresher microstrip if few particles are suspended on it.		

Observations:

In the end of the process, the area corresponding to the microchannel's interior must be completely removed in the Al layer. This is needed for the next step, in which the exposure of the negative photoresist (SU-8) will result in the removal of the non-exposed regions (regions with Al). The SU-8 resist will prevail in the microchannel's interior, so that the PDMS can enclose this region when poured on top of it, leaving a lacunar region where the resin was placed.

Runsheets – Immobilization Tests on Au and Si

SU-8 Mould

Started: 09/09/2016

Finished: 09/09/2016

Responsible: Pedro Brito

1.	Substrate Cleaning	Date: 09/09/2016
<p>Equipment: Wet Bench Substrate: Silicon wafer</p> <p>Cleaning Procedure:</p> <ol style="list-style-type: none"> 1 – Rinse and rub with acetone, DI water, IPA and DI water again 2 – Sonication with Alconox (15 min, 65°C) 3 – Sonication with DI water (30 min, 65°C) 4 – Rinse with IPA and DI water and blow dry with compressed air 		

2.	SU-8 spin coating	Date: 09/09/2016
<p>Equipment: SVG Track Photoresist: SU-8 (Negative Photoresist) Layer thickness: 20 µm</p> <p>Coater Track Programs:</p> <p style="padding-left: 20px;">Spinner Program: 19 or 20 (Edit Mode)</p> <ul style="list-style-type: none"> - Spin at 500 rpm for 10 sec with an acceleration of 100 rpm/sec - Spin at 1700 rpm for 34 sec with an acceleration of 300 rpm/sec <p>Procedure:</p> <ol style="list-style-type: none"> 1 – Before inserting the sample, make sure to protect the spinner’s walls with aluminum foil. 1 – The substrate is placed on the spinner (be sure to press the vacuum button to fix the substrate) 2 – Pour the SU-8 over the Si substrate 3 – Press Run Mode followed by Run 4 – After spin coating, heat the sample on the hot plate at 95 °C for 4 min (soft bake) 5 – Cool down to room temperature (>2 min) 		

3.	UV exposure for SU-8 patterning	Date: 09/09/2016
<p>Equipment: UV Light Box Duration: 27 sec</p> <p>Procedure:</p> <ol style="list-style-type: none"> 1 – Place the substrate on the light box support along with the hard mask on top 2 – Insert the UV filter and the substrate holder on the respective slots 3 – Remove the filter and start counting the time 4 – Insert the filter and remove the substrate holder 5 – Remove the substrate and hard mask from the holder 6 – Heat the substrate on a hot plate (5 min at 95 °C) 7 – Cool down to room temperature (>2 min) <p>Note: Turn on the UV lamp 30 minutes before use (wear UV goggles)!</p>		

4.	SU-8 development	Date: 09/09/2016
<p>Equipment: Wet Bench Developer: PGMEA</p> <p>Procedure:</p> <ol style="list-style-type: none"> 1 – Immerse the SU-8 sample in the developer and agitate for 2 min 2 – When development is complete, clean with IPA (do not point the IPA squirt directly at SU-8 structure) 3 – Hard bake at 150 °C for 15 min. <p>Profilometer (SU-8 thickness): Å, Å, Å, Å, Å.</p> <p style="text-align: center;">± Å</p>		

Observations:

Runsheets – Immobilization Tests on Au and Si

PDMS Micro-channel Fabrication

Started: 09/09/2016

Finished: 10/10/2016

Responsible: Pedro Brito

1.	PDMS preparation	Date: 09/09/2016 (1 st) 30/09/2016 (2 nd)
Equipment: Wet Bench		
Procedure: 1 – Prepare Sylgard 184: mix base and curing agent 10:1 w/w for 5 min (59,4:5,94 g) 2 – Clean the mixing tool with IPA 3 – Place the solution in vacuum for air bubbles extraction (~40 min) 4 – Dispense PDMS on the mould 5 – Cure in the oven at 70 °C for 2 hours 6 – Manually punch the inlets and outlets of the channels after curing		

2.	Irreversible surface bonding	Date: 10/10/2016
Equipment: Wet Bench and UVO chamber		
Procedure: 1 – Clean the glass containing the Au and Si structures and also the PDMS using IPA and then blow dry 2 – Place the samples in the Plasma Cleaner chamber (2 min in active plasma) 3 – Press the PDMS towards the glass substrate after aligning them. 4 – Dry for 30 min at 70 °C		

Observations:

The outcome of the first alignment was satisfactory since the structures were all placed inside the channel. Nevertheless, the alignment process took a lot of time (~10 min) so it is necessary to confirm that the sealing was successful.

The second alignment was much better than the first one both in terms of localization of the structures and duration. Anyway, this second PDMS block was less sticky than the first one which may possibly return an incorrect sealing.

